Summer 2024

Process Modeling of Composites for Automated Fiber Placement

Von Clyde Jamora
Old Dominion University, vonjamora@gmail.com

PROCESS MODELING OF COMPOSITES FOR AUTOMATED FIBER PLACEMENT

By

Von Clyde Jamora
B.S. May 2018, Old Dominion University
M.S. May 2020, Old Dominion University

A Dissertation submitted to the faculty of
Old Dominion University in Patial Fulfillment of the
Requirement for the Degree of

DOCTOR OF PHILOSOPHY

MECHANICAL ENGINEERING

OLD DOMINION UNIVERSITY
AUGUST 2024

Approved By:

Oleksandr Kravchenko (Director)

Krishnanand N. Kaipa (Member)

Sergii Kravchenko (Member)

Gene Hou (Member)

ABSTRACT

PROCESS MODELING OF COMPOSITES FOR AUTOMATED FIBER PLACEMENT

Von Clyde Jamora
Old Dominion University, 2023
Director: Dr. Oleksandr Kravchenko

Fiber-reinforced composites are available in various material systems, each requiring specific manufacturing techniques to exploit their unique properties fully. Systems such as woven fabrics and preimpregnated fibers employ distinctive methods to harness these properties effectively. For instance, non-crimp fabrics (NCF) use high-pressure resin transfer molding and prepregs, like IM7-8552, use manufacturing method called automated fiber placement (AFP). However, these manufacturing processes often introduce deposition features that can evolve into defects. Their occurrence and impact on morphology must be predicted using experimentally informed finite element models. The research began with compaction experiments on NCF fabric, leading to the development of a constitutive equation for an FEA model that simulated the evolution of fiber volume fraction and wrinkling between the woven fabric layers. The model highlighted the strain-rate dependence on fiber volume fraction distribution across NCF layers. The study then focused on the deposition of a prepreg tow on a composite substrate, modeled using a visco-hyperelastic constitutive equation with an anisotropic tensorial viscosity. This was coupled with a thermo-rheological model to predict heat transfer and resin development within the composite layers. Experiments with increasing substrate layers were conducted, with the spreading of the tow recorded in both experimental trials and numerical models. The substrate layers influenced the compaction and temperature gradient, affecting the substrate's viscous properties.

After deposition, the visco-hyperelastic model was validated during early curing phases by creating and measuring unidirectional composite coupons, comparing this data to similar models. A laminate with a single fiber tow gap was also studied, revealing discrepancies in predicting resin-rich region volumes. Incorporating resin bleed-out into the model improved accuracy by accounting for fiber volume fraction evolution and internal pressure in the fiber tow gap, providing structural support to the sinking plies. The addition of the resin bleed out results in a more accurate model prediction. The research culminates in attempting to predict the morphology of a laminate with multiple fiber tow gaps. Although the previous concepts were applied, they did not accurately predict the laminate's morphology, indicating potential for further research and the development of new concepts to simulate the composite manufacturing process accurately.

ACKNOWLEDGEMENTS

To my teachers who began my path in engineering,
Especially the one who called me a doctor, a prophecy endearing.
To my professors who showed me the art of learning,
And my colleagues, whose support kept my spirit burning.

To the students I taught, together we grew,
In every lesson shared, I learned with you.
To Oleksandr Kravchenko, my guide and friend,
The best advisor on whom I could depend.

To my committee who believed in my quest,
Your faith in me inspired my best.
To my parents who provided all I needed,
Your love and support were always heeded.

To my sisters, the best siblings in the world,
In your encouragement, my dreams unfurled.
And to my beautiful wife, my heart's delight,
For you, my love, I reached this height.

TABLE OF CONTENTS

Chapter Page

List of Figures

Figure Page

Figure Page

Figure Page

Figure Page

Figure Page

1 Introduction

Composites are a combination of two or more constituents that produce a superior material by retaining the distinct properties of each component. Specifically, fiber reinforcement materials, such as carbon fiber, glass, or natural fibers, are combined with a polymer matrix, which can be thermoset or thermoplastic. This amalgamation enhances the properties of the homogenized components, resulting in a superior product. Among these materials, fiber-reinforced composites have gained significant popularity, particularly in lightweight structures used in aerospace, automotive, and medical fields. The structural fibers in these composites can be made from various materials, including carbon fibers, nylon, and natural fibers. Composites are available in numerous forms such as continuous fibers, short fibers, stitched fabric, chopped fibers, and woven fabric. These composites are supplied as pellets or strips pre-impregnated with resin.

The resin itself can be a thermoset, which undergoes an irreversible curing process, or a thermoplastic, which cures through a reversible process. The diversity of composite material systems highlights their versatility and broad range of manufacturability. For example, short fibers trade the strength of continuous fibers for the ability to form complex geometries. Over the years, composites have become more commercially viable due to advancements in polymer chemistry and novel manufacturing methods[1], [2], [3]. This progress has led to cost reductions in structures that can compete with metal counterparts. Despite the significant potential of these materials, the processing techniques used in their fabrication can profoundly affect their final structure and performance. Therefore, it is crucial to examine the manufacturing processes of composites in detail. This study aims to investigate various aspects of composite manufacturing processes and to establish a digital thread for predicting the quality of the manufactured composites, especially those utilizing thermoset resin.

The processing of thermoset composites encompasses various methods, each tailored to specific applications and performance requirements. Traditional techniques such as manual stacking of thermoset tape are used to fabricate composite plates. Additionally, compression molding and injection molding are common methods for rapid manufacturing but lower strength applications. Compression molding involves squeezing a deformable charge within a heated mold, while injection molding entails grinding pellets and fibers, then extruding them into a mold [4]. However, for applications demanding higher tolerances and greater load-bearing capabilities, more precise manufacturing methods are essential. Liquid composite molding is one such method, where a plunger delivers resin into a closed mold, ensuring more uniform pressure distribution within the mold cavity [5]. State-of-the-art manufacturing processes include additive manufacturing, where the direction of fibers becomes a design variable, offering customization and optimization of composite structures by varying the fiber direction [6], [7]. The diverse families of composite manufacturing techniques involve numerous composite types, each designed to accommodate specific material systems and structural complexities. This versatility ensures that the appropriate method can be selected to meet the unique demands of various applications, enhancing the performance and reliability of thermoset composites.

The manufacturing methods for composites exhibit significant diversity, reflecting the wide array of composite materials themselves. For dry fabrics, the process involves a mold that applies both heat and pressure to shape the structure [8]. During this procedure, resin is infused into the mold, permeating the interwoven fibers. The subsequent application of heat and pressure solidifies the resin and sets the composite's geometry. In contrast, the fabrication of structures using composite tows involves curing within an autoclave, which subjects the material to both heat and pressure. To ensure uniform pressure distribution across the composite, the laminate is placed in a

vacuum bag, which compresses the structure prior to the autoclave's pressurization. Both manufacturing techniques rely on the thorough dispersion of resin throughout the fibers, aiming to produce a homogeneous solid structure once the resin cures and cools. Despite the precision of these methods, the occurrence of defects during the manufacturing process remains inevitable. Understanding and mitigating these defects are crucial for optimizing the performance and reliability of the final composite structures.

Defects in composite materials originate from the early stages of the manufacturing process, specifically from deposition characteristics. During the compaction of dry fabrics within a mold, the fiber volume fraction can exhibit variability across the quasi-isotropic layers [9], [10]. Additionally, the interaction between layers can introduce waviness within the laminate, leading to an uneven distribution of resin throughout the structure. This uneven distribution results in resin-rich regions and fiber misalignment[11]. When composite prepreg tows are deposited on structures with complex curvatures, deposition irregularities such as fiber tow gaps and overlaps can occur. These irregularities propagate into defects during the manufacturing process. The flow of resin exacerbates the formation of resin-rich regions, fiber waviness, voids, and inconsistencies in fiber volume fraction. These features, developing during manufacturing, ultimately reduce the strength of the composites. Mitigating these defects is crucial for optimizing the performance and reliability of composite materials. Each manufacturing process must be meticulously analyzed to identify and understand the sources of these defects. By doing so, strategies can be developed to minimize the occurrence of gaps and overlaps, thereby enhancing the overall quality of the composite structures.

Dry fabrics are manufactured through a process involving the compression and infusion of textiles with resin, subsequently forming composite structures via preforms [12]. Often these

fabrics are woven together to form different patterns, such as plain weave, twill, and basket weave to name a few. One of these configurations consists of multiple layers of unidirectional fibers held together by stitching materials, such as nylon, in a quasi-isotropic arrangement also known as non-crimp fabric (NCF). This method preserves the material's mechanical properties better than conventional stitching techniques [13]. Since the resin is infused later in the manufacturing process, the material has an extended shelf life and can be easily shaped into complex forms before the gelation process begins (Figure 1). Additionally, due to its fabric-like nature, it demonstrates superior drapability, allowing the composites to conform to complex curvilinear structures prior to resin infusion. This capability is particularly advantageous for creating intricate geometries in advanced composite applications.

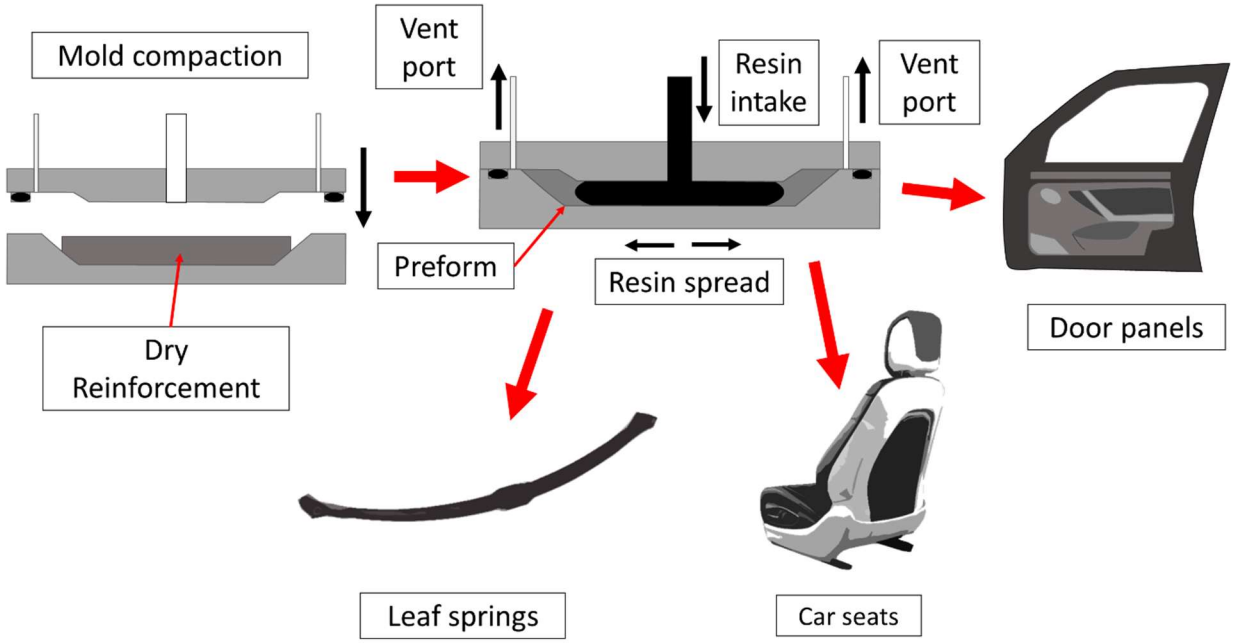

Figure 1. High pressure resin transfer molding, where liquid resin is infused into a dry textile using a vacuum inside a preform.

The flexibility of dry fabrics introduces potential sources of defects during composite manufacturing. Techniques such as resin transfer molding (RTM) and liquid composite molding

are employed to infuse dry fabrics with resin in a preform, assisted by higher pressures or vacuum. However, during the compression of these dry woven fabrics, defects such as wrinkles and shifts in fiber orientation commonly occur prior to resin infusion (Figure 2). Additionally, the compression process alters the fiber volume fraction in the preform. These variations significantly impact the permeability of the dry fabric, thereby influencing the resin infusion process. Consequently, a comprehensive understanding of the evolution of both the geometry and the fiber volume fraction is essential to fully harness the potential of this material. This understanding will facilitate the development of strategies to minimize defects and optimize the performance and reliability of the final composite structures.

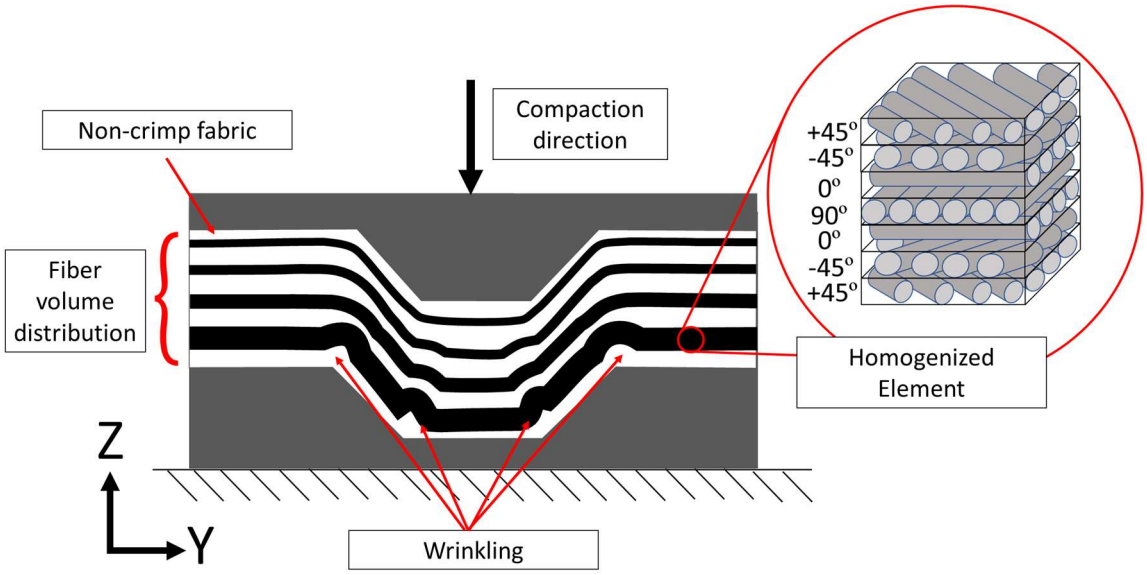

Figure 2. Schematics of the compaction roller model with homogenized elements of the non-crimp fabric. Wrinkling can be seen at the corners due to the shearing between layers.

State-of-the-art manufacturing methods increasingly focus on automating the deposition of composite tows, specifically through the ability to lay individual strips of composite material, enabling the adaptation of composites into complex structures [14]. These methods include

automated tape laying (ATL) and automated fiber placement (AFP) [14], [15]. The early development of AFP technology can be traced back to a research initiative at the Royal Establishment in 1966, which utilized carbon fiber materials [14]. This technology became commercially available in the early 1980s through the efforts of Hercules Inc., which developed it for aircraft and other high-performance structural application [14]. Significant advancements in computer numerical control machine tools, computer-aided design, and computer-aided manufacturing has facilitated high-throughput manufacturing processes for fiber-reinforced composites, allowing for intricate layups with reduced processing cycle times [14], [16]. These manufacturing methods enables the production of complex and precise structures.

AFP utilizes reinforced composites to construct complex layups with reduced processing cycle times [14], [16]. This composite deposition technique places strips of prepreg tows to create layers of thermoset or thermoplastic composites at specified locations. By enabling tailored orientations, AFP produces variable stiffness structures that cater to specific loading conditions while reducing weight compared to traditional layups [17], [18], [19], [20], [21]. However, layup defects during the AFP manufacturing process can result in an irregular, non-uniform morphology after the curing and compaction of the AFP preform. Deposition-induced AFP tow features, particularly fiber tow gaps, inevitably lead to local irregularities upon cure and compaction [22]. Previous studies indicate that manufacturing defects arising during the early stages of cure, before resin gelation, can significantly impact the mechanical properties of the composites [23], [24], [25]. Understanding these defects and their origins is crucial for optimizing AFP processes and improving the structural integrity and performance of composite materials.

A common consensus among numerous researchers identifies fiber tow gaps and overlaps, initiated during the deposition stage, as primary contributors to failure initiation [22], [26], [27],

[28], [29], [30], [31]. Wang et al. highlighted the influence of resin transverse flow on composite structure [32], while Sawicki et al. demonstrated that fiber tow gaps and overlaps diminish the compressive strength of composites [33]. Guin et al. investigated the effects of tow-to-tow gaps and overlaps in AFP manufacturing, revealing a substantial increase in waviness that reduces the tensile strength of both notched and unnotched composites [34]. Their research also proposes an allowable gap size during AFP manufacturing. These studies underscore how deposition-induced features introduced early in the process can significantly diminish strength, resulting in irregularities in the cured composite [22], [23], [28], [35]. These morphological irregularities, including resin-rich regions, waviness, and voids, form during the compaction of the deposited preform in the curing process [36]. While tolerances exist for fiber tow gaps and overlaps, overlooking their presence risks the development of defects in the composite laminate [34]. These regions with irregular morphology can serve as weak points, reducing the overall strength of the composite material [37], [38], [39].

One source of defects in composite manufacturing arises from the deposition of composite tow. The application of heat during tow deposition induces a transition of the resin to a more viscous state, exhibiting hyper-viscoelastic properties early in the curing cycle [40], [41]. Deposition-induced features such as gaps and overlaps are inevitable but can be significantly managed through strategic tow deposition techniques. The spacing between composite tows plays a critical role in the formation of tow deposition features. These features are influenced by tow spreading, where the tows deform under the pressure applied by rollers. While existing studies have investigated tow spreading in response to changes in deposition process parameters [34] - [38], there remains a limited understanding of the interactions between the prepreg laminate and the tow itself. Many studies focus on the adhesion (tackiness) between the deposited tow and the

substrate; however, the deformation of the tow, particularly in relation to the spreading phenomenon during deposition, has been largely overlooked.

As the thickness of the substrate increases, the underlying surface beneath the tow exhibits greater compliance compared to rigid aluminum tooling. Considering the non-linear nature of contact stresses [47], the interaction between the hyperelastic rubber roller and the non-linearity in both the deposited tow and the prepreg laminate substrate results in varying transverse spread of the tow during deposition (Figure 3). Consequently, insufficient control over tow spreading has been demonstrated to lead to increased defect formation [48], [49]. In this study, we investigate the role of the prepreg laminate in its interaction with the fiber tow during the deposition stage. Specifically, the elastic recovery of the prepreg after the roller passes influences variations in tow spreading due to its non-linear material behavior. This recovery process is influenced by transient heat transfer dynamics and the release of contact forces between the roller, the deposited prepreg tow, and the prepreg layup.

Moreover, the present study investigates the impact of substrate thermal conductivity on the mechanics of deposited tow deformation, emphasizing the contrast between the high thermal conductivity of metallic tools and the lower thermal conductivity of prepreg laminates. Variations in transient heat transfer, arising from substrate material differences and thickness, create temperature distributions that modify the hyperelastic compaction behaviors of both the prepreg tow and the substrate (Figure 3). With increasing thickness of the composite substrate, heat dissipation through the thickness slows down, influencing the substrate's compliance due to the temperature-dependent hyper-viscoelastic properties of the composite. The interplay among applied force, heat distribution, and non-linear contact affects the resulting tow width and spacing.

This complex interaction remains underexplored, motivating this study to offer insights into this multi-physics phenomenon.

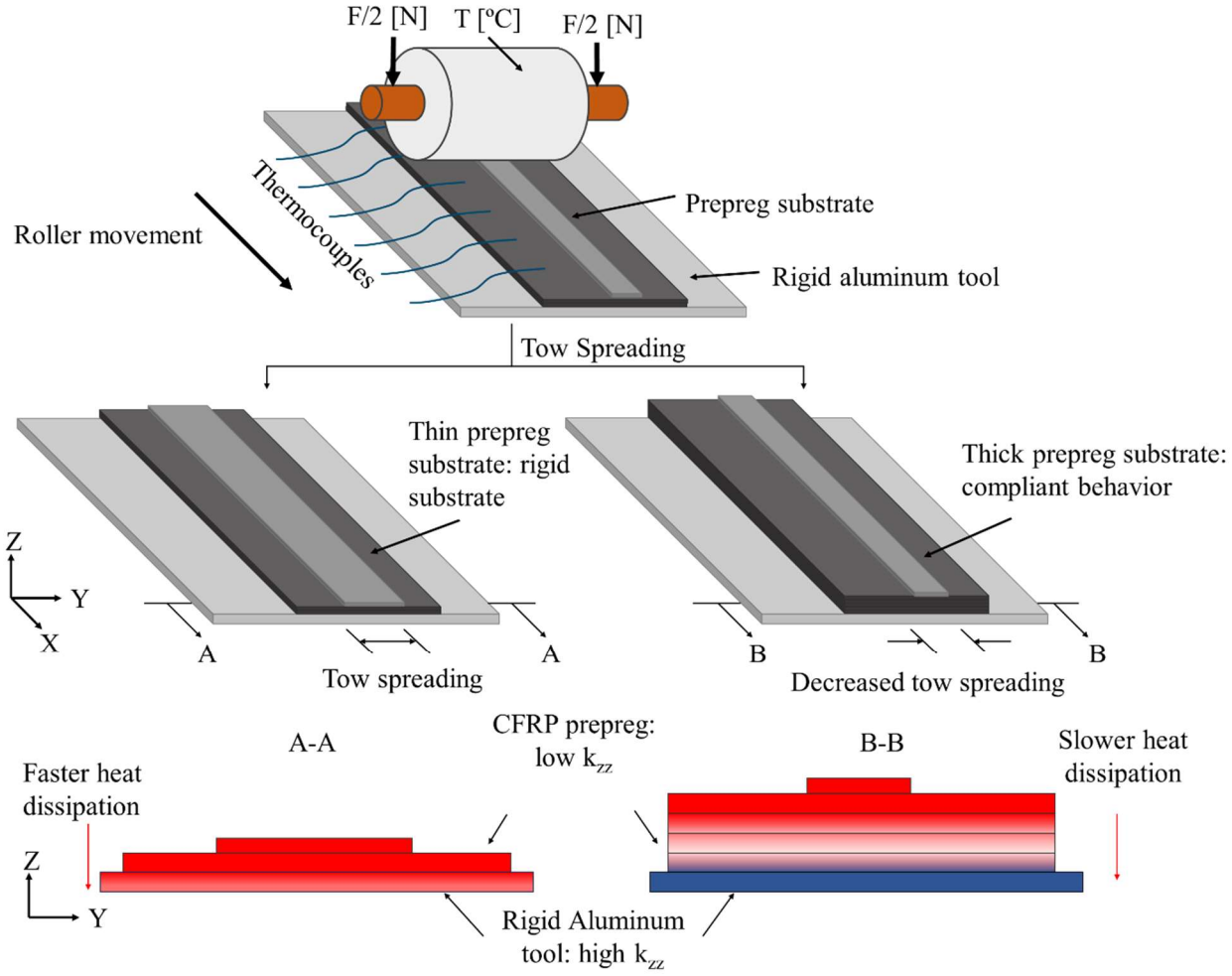

Figure 3. The experimental setup using roller deposition showing the effect of substrate rigidity on tow spreading

Defects in composites stem from various factors during the curing process, including variations in resin distribution and the spreading of composite tow. Fiber tow gaps and overlaps can be controlled during manufacturing within specified tolerances. However, during the curing process, which solidifies the material for structural application, these defects propagate from the early stages of deposition. The presence of layup defects such defects (Figure 4) comes from AFP

deposition features is unavoidable and should be accounted for in the manufacturing of AFP composites to accurately predict structural strength [50], [51]. Moreover, these resulting defects have been shown to significantly reduce the overall strength of composites due to the resultant morphology [12], [13]. Microscopic features, such as redistribution of fiber volume fraction, and mesoscopic features like ply thickness and waviness, are interconnected and should be analyzed comprehensively within a framework that considers their coupling effects【[21], [52], [53].

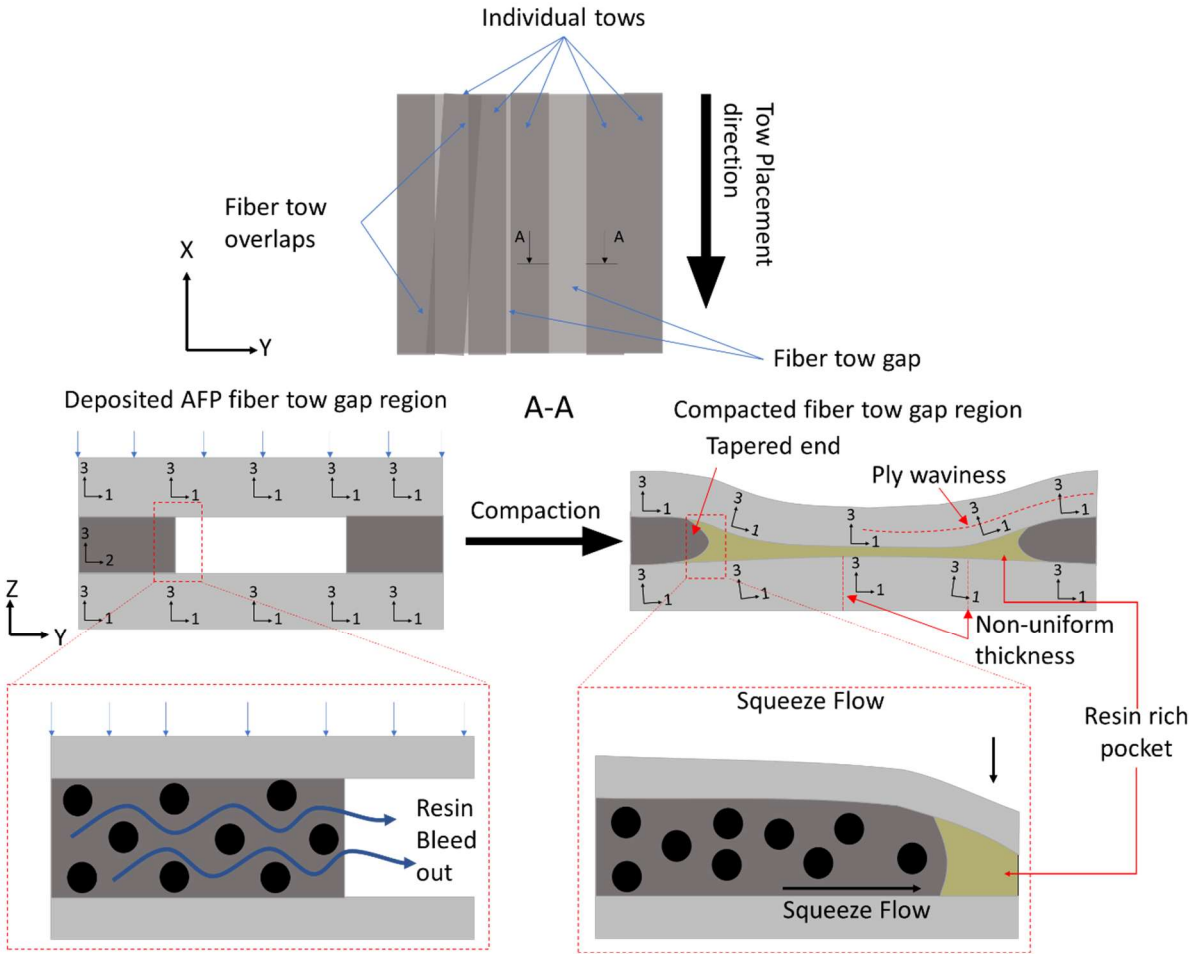

Figure 4. Diagrams illustrating gaps within a laminate and the influence of resin bleed out on the nonlinear morphology.

The resin undergoes a transition from an incompressible viscoelastic liquid to a viscoelastic solid upon gelation before vitrification. Compaction of AFP-deposited preforms begins prior to composite gelation, where resin viscosity depends on the degree of cure and temperature [19], [20]. The deformation of deposition features during this period results in irregular geometry. During this stage, prepreg deformation resembles that of a homogeneous medium, characterized by squeeze flow. In the case of a laminate with a fiber tow gap, the squeeze flow develops when the fiber tow above the gap region is pushed inside of the void space during the compaction. Simultaneously, resin bleed out occurs through the fiber bed (Figure 5), resulting in the formation of resin-rich regions within tow gap voids and localized variations in fiber volume fraction within the composite [21]. Traditionally, resin bleed out has been considered negligible in prepreg manufacturing; however, its impact on ply waviness becomes significant in AFP preforms with fiber tow gaps [22].

In composites with inextensible fibers, deformation of the prepreg matrix plays a crucial role. As the resin flows both axially and transversely to the fibers, distinct flow regimes emerge during fiber bed compaction. Specifically, squeeze flow involves the homogeneous deformation of the tow, while percolation flow drives resin infiltration through the fiber bed [54]. Squeeze flow occurs as the fiber tow above the gap region compresses into void spaces during compaction, leading to ply sinking and changes in fiber orientation due to tow waviness. Concurrently, resin from percolation flow contributes to the formation of resin-rich zones in the tow gap region and local increases in fiber volume fraction within the composite. These microscopic alterations in composite morphology significantly impact mechanical strength, resulting in substantial reductions in mechanical properties [24]. While individual studies have characterized the contributions of these flow regimes during composite compaction [55], [56], both phenomena

occur concurrently. Therefore, a primary objective of this research is to elucidate the combined impact of percolation flow and squeeze flow during the early stages of the curing cycle. Experimental characterization of percolation flow dynamics was undertaken to comprehensively understand resin outflow mechanisms prior to gelation.

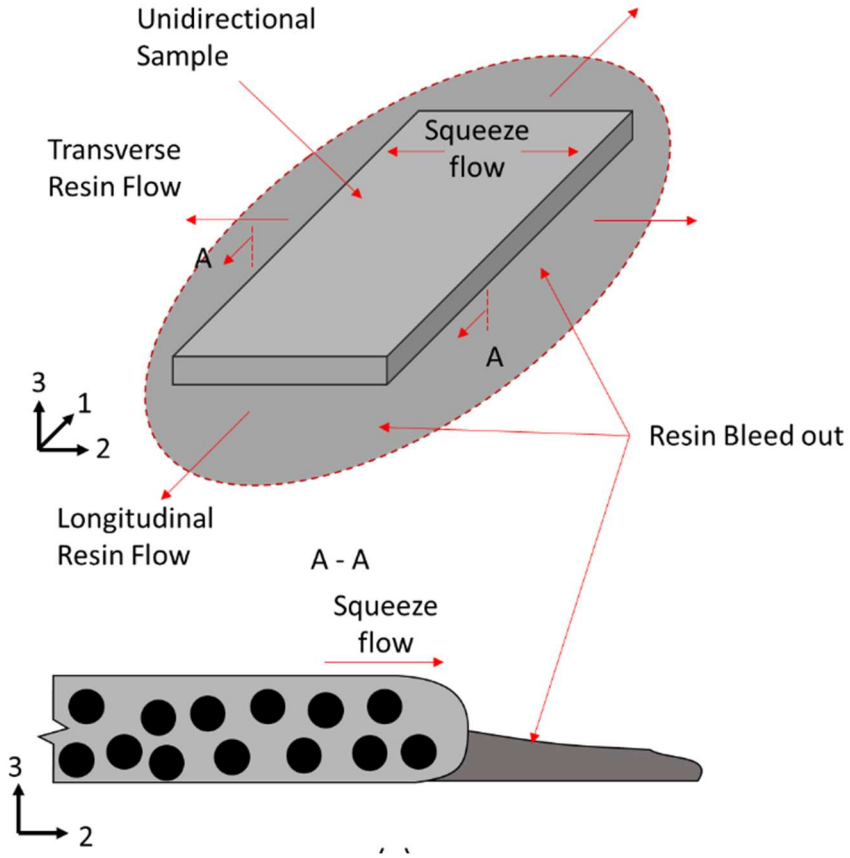

Figure 5. Schematics of the bleed out in a unidirectional composite sample.

The occurrence of gaps and overlaps early in the manufacturing process necessitates predictive methodologies. Establishing a digital thread enables a proactive approach to composite manufacturing. Finite element analysis (FEA) has emerged as a robust tool capable of modeling various aspects of composites. It has demonstrated efficacy in predicting stress-strain responses

across different length scales, failure modes in composite laminates, and buckling behaviors in structures with variable stiffness [57], [58], [59], [60]. For example, buckling in variable stiffness was also simulated with good accuracy using FEA [61]. Additionally, FEA can simulate the progressive failure analysis and fatigue simulations in composites [59], [62], [63], [64], [65]. Furthermore, FEA has been used to predict the chemical and thermal shrinkage due to the residual stresses after the manufacturing [66], [67]. Therefore, FEA's capability to simulate highly non-linear material behaviors and large deformations makes it suitable for analyzing both roller compaction and autoclave curing processes, which are crucial for predicting the appearance of deposition features requiring physical stress and thermal analyses. The interconnected physics of composite manufacturing necessitate simulation in a physically meaningful manner. Each manufacturing method and material system presents unique challenges, but both exhibit either an apparent viscous or viscous response to stress. Therefore, the application of FEA to simulate these complexities in the two-material system studied herein holds promise for advancing predictive capabilities in composite manufacturing.

Observing the manufacturing process of composites using fabrics presents challenges due to the nature of rapid preform compaction, particularly with varied molding geometries utilized in production [68]. Fabric infusion with resin hinges significantly on the permeability of the fiber bed to achieve uniform structures in textile-based composite manufacturing. Research indicates that resin infusion dynamics are influenced by fabric deformation, underscoring the importance of predicting NCF compaction behavior for achieving even resin distribution [69]. To address this, an experimentally informed viscoelastic model is employed to simulate NCF compaction during preform fabrication. The developed model utilizes Abaqus software coupled with a custom VUMAT subroutine to predict both compaction dynamics and fiber volume fraction in NCFs. The

constitutive model for NCFs employs a viscoelastic approach combining elastic and viscous components to accurately capture the behavior of transversely isotropic NCF structures.

A multi-physics model was employed to simulate the hyper-viscoelastic behavior of deposited tows and the prepreg substrate. Unlike fabrics, these fibers are preimpregnated with resin, and a critical component, the rubber roller, was modeled as a hyperelastic solid. This modeling approach successfully captured experimentally observed trends in non-linear tow spreading under applied pressure, as well as the influence of prepreg laminate thickness on tow deformation. The model accounted for contact stresses arising from roller-tow and tow-laminate interactions, alongside transient heat transfer effects that influenced tow mechanics during deposition (Figure 6). Elastic recovery within thicker prepreg substrates was identified as a significant factor contributing to tow contraction as the roller passed over deposited tows. Moreover, transient heat played a crucial role in the hyper-viscoelastic behavior of the tow, with reduced heat transfer correlating to increased prepreg substrate thickness. Experimental observations and finite element analysis (FEA) simulations aligned well, demonstrating the potential of the multi-physics modeling approach to predict deposition-induced features in AFP processes. This integrated modeling framework offers valuable insights into optimizing AFP parameters and understanding the complex interactions governing composite manufacturing processes.

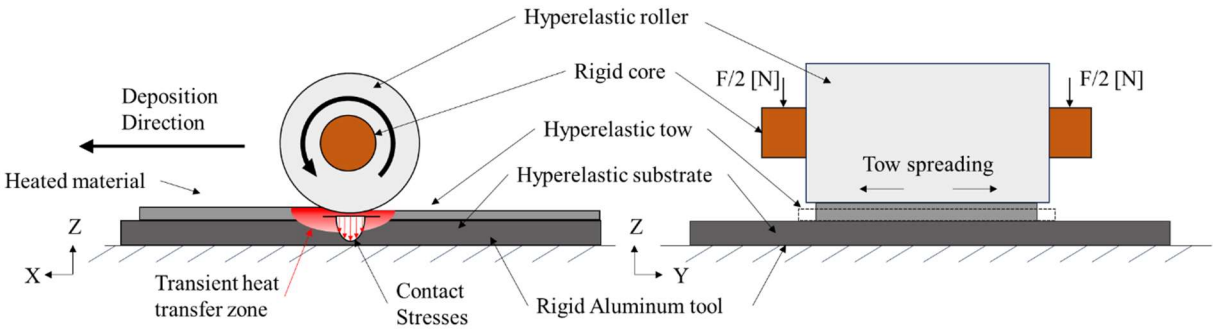

Figure 6. A schematic of the roller interaction with the deposition roller

As resin cures, it undergoes a phase transition from a solid to an incompressible liquid, altering its viscosity and impacting compaction behavior, thereby influencing fiber orientation. The proposed approach involves modifying the FEA model to incorporate fiber reorientation and evolution of fiber volume fraction. Initially, a rheological model was employed to determine temperature-dependent variables such as resin viscosity and degree of cure. This modeling framework integrates a hyperelastic component to simulate fiber bed compaction and a viscous component to model resin flow [70]. Prior research has utilized a visco-hyperelastic constitutive equations to represent the fiber bed [71], [72]. However, the research did not consider the anisotropic viscosity of prepreg tape and its dependence on the fiber volume fraction. Furthermore, earlier studies did not consider the effects of the resin bleed out from the compacted prepreg into the gap region. The present study considers the effect of resin bleed out on the formation of non-uniform morphology around the region of the fiber tow gap. To model prepreg behavior around the internal void, like in the case of debulking, a negative internal pressure gradient can be considered inside of the void using porous-cohesive elements[73]. Another approach is to consider the flow front filling the gap via a one dimensional numerical model [74].

These studies represent a two phase modeling scheme where a region other than the composite is represented [74], [75]. In the present work, a single-phase model was used and the effects of the resin bleed out into the gap was shown to have a larger impact on the morphology of the composite prior to resin gelation. The model focuses on comprehensively addressing complex multi-physics phenomena in defect regions, such as laminates with missing fiber tow gaps. Furthermore, an iterative modeling approach facilitates a novel method for simulating percolation flow.

The present treatise extends the use of a hyper-viscoelastic model by introducing the fiber volume-dependent anisotropic tensorial viscosity of the prepreg into the formulation of the viscous component [29], [23], [30]. This approach introduces the local fiber volume fraction as a coupling between the squeeze flow and resin bleed out. Resin bleed out measurements were obtained from the unidirectional tape compaction experiments and used to predict the amount of resin bleed out around the tow gap region. In the present case, a single-phase model was developed based on sequential compaction flow analysis which adds the influence of resin flow into fiber tow gaps without explicitly modeling the resin. First, the hyper viscoelastic FEA squeeze flow was performed, and the tow gap volume decrease was predicted. Once the tow gap volume reached the resin bleed out volume the time of filling was predicted. To capture the presence of resin inside of the tow gap, internal pressure was introduced in the tow gap based on the predicted time of void filling. The interaction between the squeeze flow and resin bleed out was investigated and the predicted resin-rich pocket shape agreed closely with the experimental observations. The proposed sequential compaction flow methodology can be extended to modeling various combinations of fiber tow gaps in AFP manufacturing to predict fiber waviness, resin-rich regions, as well as ply thickness variation in the region around the fiber tow gaps.

Typically, an AFP system deposits multiple layers of plies in a stacking sequence, often in a quasi-isotropic configuration with eight layers [2]. Consequently, multiple fiber tow gaps can be observed throughout the thickness of the AFP preform, significantly affecting the compaction-induced large deformations. The modeling approach initially developed for a single fiber tow gap can be extended to analyze quasi-isotropic laminates containing multiple fiber tow gaps. Specifically, employing the visco-hyperelastic model facilitates the prediction of resin bleed-out and adopts a sequential modeling approach to accurately anticipate the final morphology. The various models presented in this study collectively contribute to understanding composite manufacturing processes. Each concept builds upon or utilizes the underlying physics established in preceding models, enhancing the comprehensiveness and predictive capability of subsequent analyses.

2 Literature Review and Background

2.1 Derivations of the visco-hyperelastic model

A visco-hyperelastic model is a computational scheme for time-dependent simulation which can be employed for simulating composites. There are numerous visco-hyperelastic models which can be utilized by fiber-reinforced composite material systems. However, much of visco-hyperelastic model is derived from outside the field of composites. One example comes from the work of Kelly [76]. The work proposes that fibrous materials experience hysteresis when subjected to a cyclic load. This is the result of two properties, viscoelasticity, and a rate-dependent deformation. The work presented by Kelly proposes a phenomenological approach to modeling both the viscoelastic compaction and the relaxation of the fibrous material. The stress can be decomposed into two components, a strain and strain rate dependent functions as shown in Eq. (1).

$$\sigma = \sigma(\varepsilon, \dot{\varepsilon}) = f_{\alpha}(\dot{\varepsilon}) f_{\beta}(\varepsilon) \tag{1}$$

Where the ε is the strain and $\dot{\varepsilon}$ is the strain-rate. Furthermore, the nature of the multiplicative decomposition allows for the equation to be collapsed into a master curve. Using a reference strain, the strain rate function can be scaled. The equation then becomes:

$$\frac{\sigma(\varepsilon, \dot{\varepsilon}_1)}{\sigma(\varepsilon^{ref}, \dot{\varepsilon})} = \frac{\sigma(\varepsilon, \dot{\varepsilon}_2)}{\sigma(\varepsilon^{ref}, \dot{\varepsilon})} = \frac{f_{\beta}(\varepsilon)}{f_{\beta}(\varepsilon^{ref})} \tag{2}$$

The scale of the stress at the reference strain becomes a scaling factor, $\frac{\sigma}{\sigma(\varepsilon^{ref}, \dot{\varepsilon})}$. At ε^{ref}, the scaling factor would equal one. This phenomenological approach allows for numerous functions to be utilized for the strain dependent term. This collapsing into a single master curve simplifies modeling for temperature dependent viscoelastic materials. These terms can be based on any

relevant factors, such as temperature or fiber volume fraction in the case of composites. For Kelly's example, the strain was represented as the fiber volume fraction and the strain rate was the compaction rate. The model is not applicable to all materials, such those who exhibit standard viscoelastic properties such as Maxwell, Voigt, and Burgers. However, the model is applicable to many viscoelastic materials, such as bundles of composite fibers, or fibers infused with viscous resin.

However, to consider the stiff fibers of the fibers, and the flow of resin in prepregs, both component needs to be considered. The work by Belenoue establishes a good basis for the model of a composite prepreg [72]. The model is derived from the work of Bonet and Burton where they present a model for a material that exhibits transversely isotropic properties [77]. The finite motions of a solid can be tracked using the deformation gradient, F.

$$\hat{F} = \frac{\partial \vec{x}}{\partial \vec{X}} \tag{3}$$

Where **x** is the current position vector of a particle in that solid, and **X** is the initial position vector. The Jacobian of this vector can be expressed as:

$$J = det\ \hat{F} = \frac{d\vec{v}}{d\vec{V}} \tag{4}$$

The deformation of a highly fiber oriented elastic material can be expressed through large displacements through the right Cauchy-Green tensor, *C*, which is solved through the deformation gradient, and the Lagrangian strain Tensor, *E*, using the deformation gradient as shown in Eq. 3.

$$\hat{C} = \hat{F}^T \hat{F}; E = \frac{1}{2}(\hat{C} - \hat{I}) \tag{5}$$

Where F is the deformation gradient, and I is an identity matrix. Additionally, the strain can be measured with the left Cauchy-Green tensor, *b*.

$$\hat{b} = \hat{F}\hat{F}^T \tag{6}$$

The stress tensor work conjugate using the Lagrangian strain is the Piola-Kirchoff stress tensor, **S,** which can be solved using the Cauchy Stress. The deformation of composites during curing and compaction typically results in large strain elasticity or hyperelasticity. This implies that the strain energy function must be used which can relate to the Piola-Kirchoff stress tensor as:

$$\hat{S} = \frac{\partial \psi}{\partial E} = 2\frac{\partial \psi}{\partial \hat{C}} \tag{7}$$

Where C can be related to either the Cauchy-Green tensor, or the Lagrangian. This formulation results in the elasticity tensor, $\hat{\mathbb{C}}$

$$\hat{\mathbb{C}} = \frac{\partial S}{\partial E} = 2\frac{\partial S}{\partial \hat{C}} = 4\frac{\partial^2 \psi}{\partial \hat{C}\,\partial \hat{C}} \tag{8}$$

This establishes a relationship for solving the stress via an energy a strain energy equation for any visco-hyperelastic part. The main part of the model constitutive equation for composite prepregs comes from the work of Limbert and Middleton [77]. The constitutive model in their work is derived for soft fibrous biological connective tissue. However, the transversely isotropic nature of this kind of tissue is analogous to fiber-reinforced composites. Therefore, the same formulation can be applied for composites. In their work, they establish that the strain energy function of a fiber-reinforced continuum can be a function of its position, the Cauchy-Green strain tensor, the structural tensor, and any other thermodynamic variables. Following this assumption of the strain energy function or the Helm-Holtz free energy equation is

$$\psi = \psi(\vec{X}, \hat{C}, \vec{N}_0, A_k) \tag{10}$$

Where A_k is the thermodynamic variables to consider. At a fixed deformation gradient, as time goes to infinity, the free energy function of the elastic portion is defined as

$$\psi^e = \psi^e(\vec{X}, \hat{C}(\vec{X}), \vec{N}_0(\vec{X})) \tag{11}$$

The function can be solved to satisfy the Clausius-Duhem inequality which reduces the first and second Principles of thermodynamics. This This creates the inequality:

$$\Xi_{int} = \frac{1}{2}\left(\hat{S} - 2\psi^e\right) : \dot{\hat{C}} \geq 0 \tag{12}$$

Where Ξ_{int} is the internal dissipation or local entropy production. The free energy equation can be derived with respect to time to obtain:

$$\Xi_{int} = \frac{1}{2}\left(\hat{S} - 2\frac{\partial \psi^e}{\partial \hat{C}}\right) : \dot{\hat{C}} \geq 0 \tag{13}$$

As for the viscous effects, a viscous potential energy equation can be as shown in eq. 10.

$$\psi^v = \psi^v(\vec{X}, \hat{C}(\vec{X}), \dot{\hat{C}}(\vec{X}), \vec{N}_0(\vec{X})) \tag{14}$$

Where an additional rate of material tensor, $\dot{C}$, is added to the free energy equation. This can be expressed as

$$\dot{\hat{C}} = \dot{\hat{C}}\left(\vec{X}, t\right) = \dot{\hat{F}}^T \cdot \hat{F} + \hat{F}^T \cdot \dot{\hat{F}} = 2\hat{F}^T \cdot \hat{\mathrm{d}} \cdot \hat{F} \tag{15}$$

Where $\dot{\boldsymbol{F}}$ is the spatial deformation gradient which is given by:

$$\dot{\hat{F}} = \frac{\partial \hat{F}}{\partial t} = \hat{\mathrm{l}} \cdot \hat{F} \tag{16}$$

where **l** is the spatial velocity gradient:

$$\hat{\mathrm{l}} = \dot{\hat{F}} \cdot \hat{F}^{-\mathbf{1}} \tag{17}$$

And d is the spatial rate of the deformation tensor, and the symmetric part of **l**

$$\hat{\mathrm{d}} = \frac{1}{2}(\hat{\mathrm{I}} + \hat{\mathrm{I}}^{\mathrm{T}}) \tag{18}$$

To ensure that the local entropy is greater than zero for any $\dot{\boldsymbol{C}}$, the second Piola-Kirchoff stress tensor must be.

$$\hat{S} = \hat{S}^e + \hat{S}^v = 2\left(\frac{\partial \psi^e}{\partial \hat{C}} + \frac{\partial \psi^v}{\partial \dot{\hat{C}}}\right) \tag{19}$$

These two additive components create the core of the visco-hyperelastic model. The superposition between the elasticity of the fibers, and the viscous component of the mixture results in the cured morphology as shown in Figure 7. The elastic components form the reversible reaction of the laminate while the viscous component records the hysteresis due to the interaction between the applied force and the thermal variables. This basic principle can be applied to

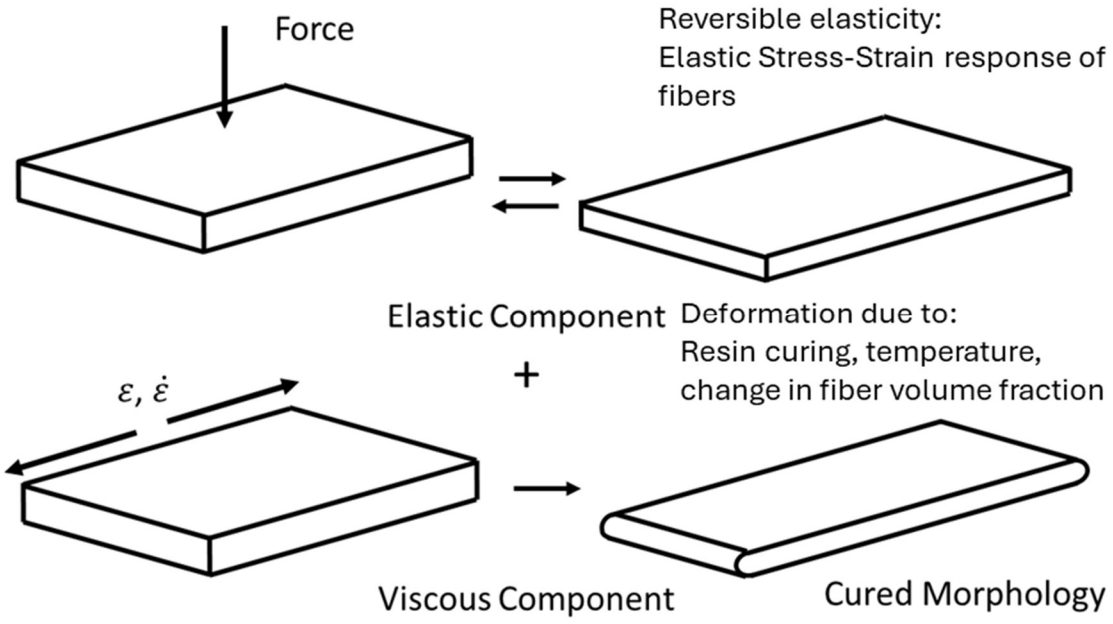

Figure 7. The basics schematics of the visco-hyperelastic model

2.2 Anisotropic tensorial viscosity

The anisotropic viscosity can be derived based on the configuration shown in Figure 8. This derivation was used for the rate term in the visco-hyperelastic model. This results in a more accurate solution when it comes to the spreading of the tow. Another assumption that these equations require for the fluid to be incompressible.

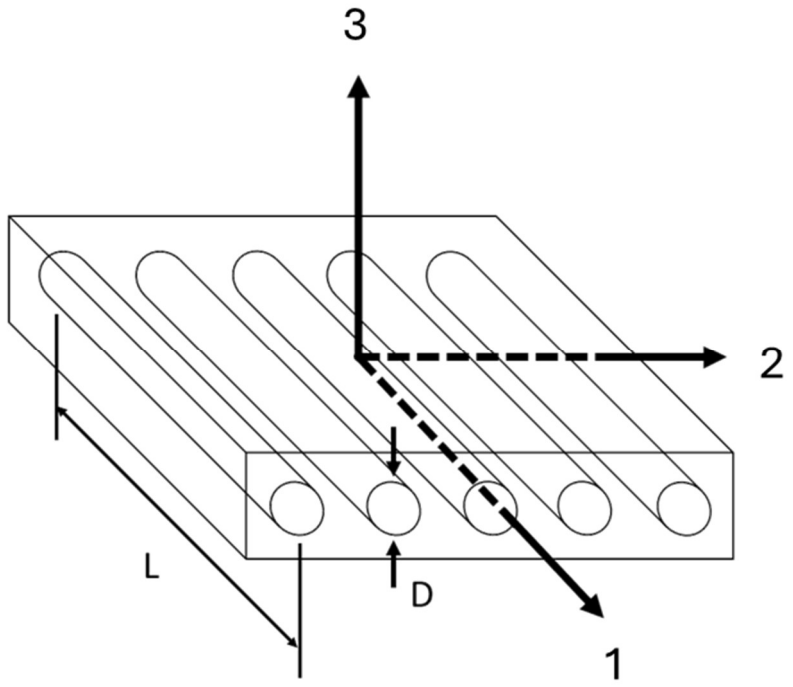

Figure 8. The transversely isotropic assembly of the fiber, which causes different rates of resin flow due to its anisotropy.

The axial deformation of the rate terms comes from the assumption that the fibers are traveling through the fiber direction through their centroids. The average shearing rate can in the matrix of the fluid based on the velocity of the fibers through their centroids is:

$$\dot{\gamma} = \frac{\dot{\epsilon}_1 L}{2(S-D)} \tag{20}$$

Where $\dot{\epsilon}$ is the average elongation strain of the composite assembly, L is the length of the fibers, D is the diameter of the fiber, and S is the fiber spacing. After proving the validity of the assumption of using the average strain rate (based on the range of fiber volume fraction), a shear stress τ is assumed to be applied on the matrix fluid. Meanwhile, the average axial stress in the fibers is:

$$\sigma = 2\frac{\sigma_1}{f} \tag{21}$$

Where f is the fiber volume fraction. The relationship between the shearing stress and the fiber stress can be determined through a force equilibrium based on the force balance on a composite thread.

$$\tau = 2\frac{\sigma_1}{f}\left(\frac{D}{L}\right) \tag{22}$$

The relationship between the fiber spacing and the diameter can be used to calculate the normalized fiber volume fraction.

$$\frac{D}{s} = \sqrt{\bar{f}} = \sqrt{\frac{f}{F}} \tag{23}$$

Where F is the maximum packing for the cross-sectional geometry. Finally, using the stress-strain relation, the effective elongational velocity can be solved.

$$\eta_{11} = \frac{\eta_{resin} f}{2}\left[\frac{\sqrt{\bar{f}}}{1-\sqrt{\bar{f}}}\right]\left(\frac{L}{D}\right)^2 \tag{24}$$

For the in-plane shear viscosity, based on a square packing of a fiber, the average shearing rate, $\dot{\gamma}$, is based on the effective strain rate, $\dot{\gamma}_{12}$.

$$\dot{\gamma} = \frac{1}{2}\left[\frac{2-\sqrt{\bar{f}}}{1-\sqrt{\bar{f}}}\right]\dot{\gamma}_{12} \tag{25}$$

Based on the direction, pure shearing that occurs only affects the resin. Therefore, the applied shearing stress and the shearing stress in the fluid at this direction is assumed to be equal or $\tau = \tau_{12}$. Consequently, the viscosity in the 1-2 plane is simply:

$$\eta_{12} = \frac{\eta_{resin} f}{2}\left[\frac{2-\sqrt{\bar{f}}}{1-\sqrt{\bar{f}}}\right] \tag{26}$$

As for the transverse shearing at the 2-3 plane, the shearing rate based on the fiber volume fraction is:

$$\dot{\gamma} = \left[1-\bar{f}\right]^{-1}\dot{\gamma}_{23} \tag{27}$$

Similarly to the in-plane shearing, the fluid shearing stress is equal to the applies shear stress or $\tau = \tau_{23}$. Therefore, the effective transverse shearing viscosity is simply:

$$\eta_{23} = \eta\left[1-\bar{f}\right]^{-1} \tag{28}$$

Finally, the transverse elongation viscosity is what influences the spreading of the composite tow. Based on the configuration of the unit cell in the 2-3 direction, the maximum shearing strain can be derived as:

$$\dot{\gamma} = \frac{2S}{S - D}\ \dot{\epsilon}_2 \tag{29}$$

Meanwhile, the matrix shearing stress based on the configuration becomes:

$$\tau = \frac{\sigma_2}{2} \tag{30}$$

Combining the two equation results in the corresponding transverse elongational viscosity:

$$\eta_{22} = \frac{4\eta}{[1 - \bar{f}]} \tag{31}$$

2.3 Multiphysics FEA Simulation Framework for AFP Fiber Tow Preform Compaction

The interconnected nature of the cure and compaction process was studied via a unified process modeling approach in the form of a physics-based simulation that captured the chemo-rheological transformation of the resin, squeeze flow and resin bleed out. Fig. 8 shows a highly non-linear multivariable model in which chemo-rheological resin behavior was used to determine the effective flow-compaction characteristics of the prepreg. Therefore, the proposed model was implemented in a commercially available FEA software ABAQUS/Explicit (Dassualt Systemes, Vélizy-Villacoublay, France) using custom-built subroutines. The rheological and physical state properties, such as the degree of cure, viscosity, fiber volume fraction and fiber orientation, updated the in-situ effective anisotropic viscosities of the fiber tow. The elements of the present model may be calibrated for different elastic and rheological properties for different material systems. With a large number of factors involved in the model, future algorithms, such as smoothed-FEA, and machine learning, can be used to predict the deformation response of

composites during manufacturing [78], [79]. However, the present methodology is a more accessible approach for the process modeling of composites [80], [81].

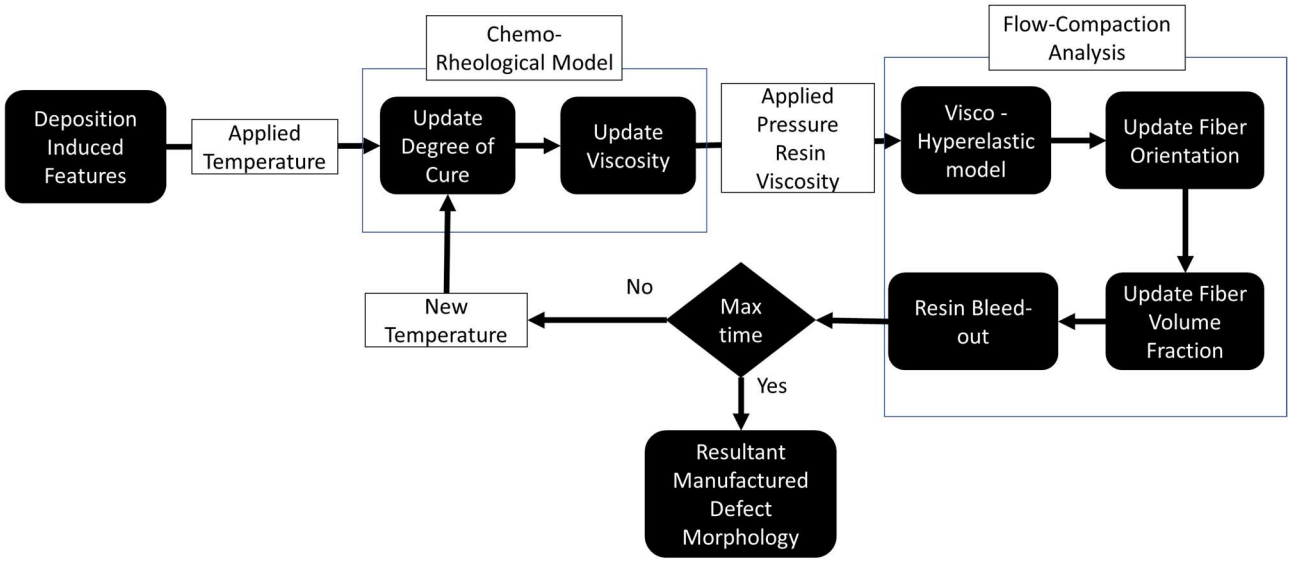

Figure 9. Coupled chemo-rheological and compaction model for predicting defect morphology in AFP manufactured composites.

2.3.1 Chemo-Rheological model

When resin is heated, resin slowly turns from a viscous solid to a viscous liquid and finally to a solid. Therefore, to model the manufacturing process it is crucial to simulate the distribution of heat throughout the laminate and the evolution of the resin. Most of the material systems of this work uses prepreg, which necessitates a model to simulate the conduction of heat and the evolution of the resin. The governing equation of heat conduction of the model comes from a three-dimensional energy balance of Fourier's heat conduction equation Eq. 20.

$$\rho_c c_c \frac{\delta T}{\delta t} + \rho_m c_m V_D \nabla T = \nabla \cdot (k \nabla T) + \rho_m \nu_m Q_t \frac{d\alpha}{dt} \tag{20}$$

Where the subscript *c* and *m* indicates the homogenized composite and the matrix, respectively. The ρ, k, Q_t, v_m, and C indicates the density, thermal conductivity, heat of reaction, fiber volume fraction and the specific heat. Finally, the T, V_D and α are the temperature, Darcy velocity and the degree of cure.

Similar to the roller compaction deposition model, heat plays a significant role in the curing process of composites. Prolonged exposure to elevated temperatures induces phase changes in the composite material, necessitating a material model to simulate the viscous flow of the resin. These changes in viscosity lead to the transverse spreading of the ply. Variables such as the degree of cure and the viscosity of the resin govern the squeeze flow behavior of the prepreg during compaction [82]. Hence, the first component is the chemo-rheological model.

The model can simulate the exothermic reactions of the resin and heat conduction for thicker composites [10]. The model's outcome includes the flow-compaction model, the degree of cure (α), and the viscosity (μ).

The first step in the chemo-rheological model is simulating the degree of cure. The curing of the resin was calculated using an equation by Hubert which was a modified autocatalytic resin kinetics equation as shown in Eq. 21 [83].

$$\frac{d\alpha}{dT} = \frac{Ae^{-\frac{\Delta E}{RT}}\alpha^{m_\alpha}(1-\alpha)^{n_\alpha}}{1+e^{C_\alpha\{\alpha-(\alpha_{c0}+\alpha_{CT}T)\}}} \tag{21}$$

For the Arrhenius equation, ΔE is the activation energy, A is a pre-exponential cure rate coefficient, and R is the gas constant, m_α is the first exponential coefficient, n_α is a second exponential coefficient, C_α is a diffusion constant, α_{C0} is the critical degree of cure at T = 0 K and finally α_{CT}

is a constant that governs the increase in critical resin degree of cure with temperature, α is the degree of cure, and T is the imposed temperature.

An initial thick unidirectional composite test model was first used to determine the capabilities of the thermo-chemical model. The had an initial temperature of 20 ºC with and a convective surface film boundary condition with a coefficient of 50 $\frac{W}{m^2K}$ was applied on the top surface and the sides of the composite. A cure cycle is shown in Figure 10. The temperature profile was applied to an FEA model and the development of the degree of cure was recorded. The variables used in the thermodynamic model is shown in Table 1.

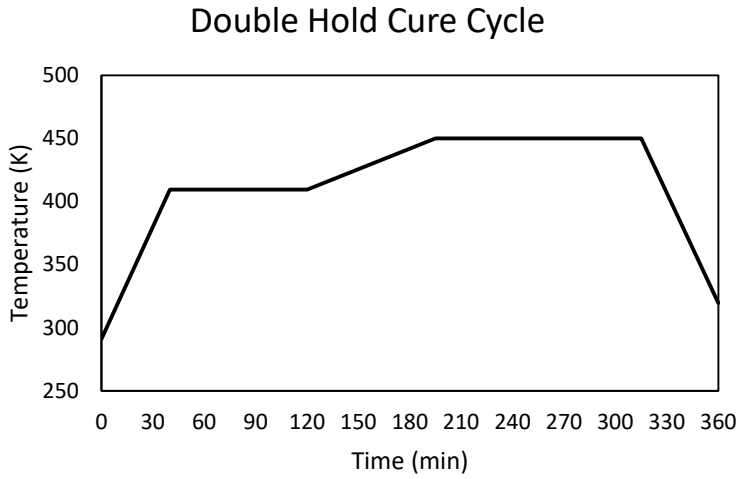

Figure 10. The temperature profile of the manufacturer recommended double hold cure cycle of IM7-8552 composite prepreg

The result of the thermodynamic model is shown in Figure 11. At 60 minutes, the temperature gradient of the laminate shows an exothermic reaction. The temperature in the middle of the laminate was shown to be 462 ºC. Compared to the outer parts of the laminate, with a temperature of 433 ºC, the middle of the laminate is shown to be a higher temperature. This

indicates demonstrates the model being capable in simulating the increase of temperature due to the exothermic reactions of the resin.

Table 1. The variables of the thermo-dynamic test	
K_1	$4.9\frac{\mathrm{W}}{m\,K}$
K_2	$0.58\frac{W}{m\,K}$
ρ	$1520\frac{kg}{m^3}$
ΔH	$474.9\ kJ$

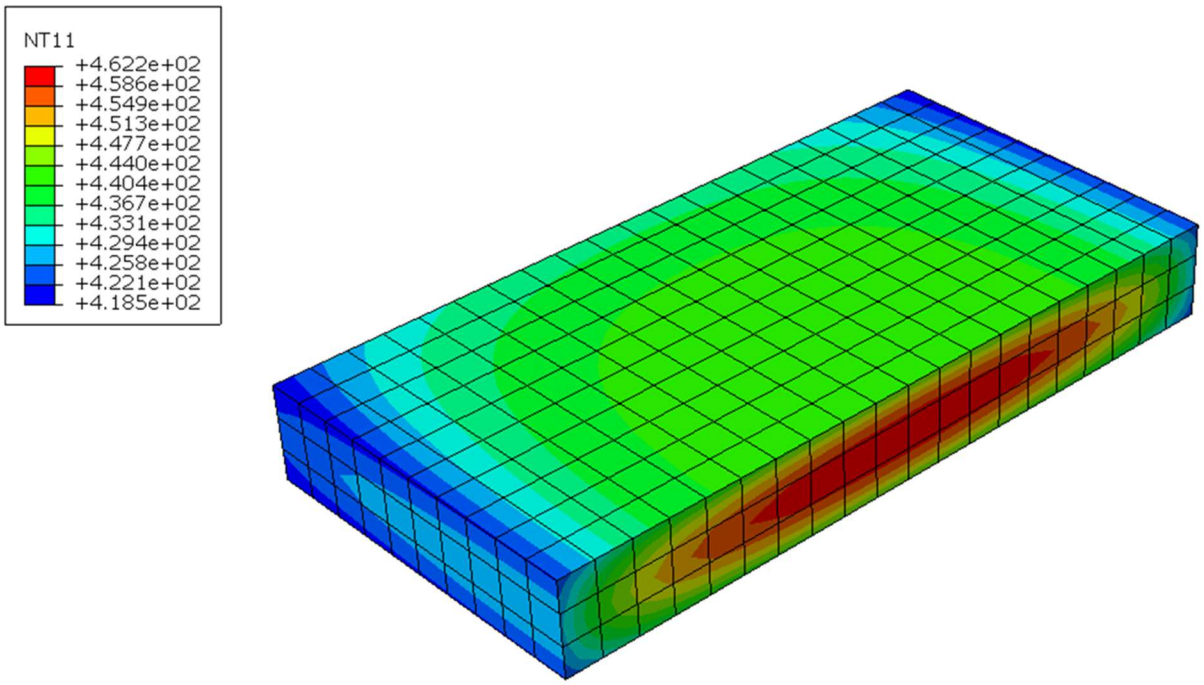

Figure 11. The unidirectional laminate at 60 minutes into the cure cycle. The model demonstrates an exothermic reaction of the resin causing an increase in temperature in the middle of the ply.

2.3.2 Hyper-viscoelastic model

From the compaction of a dry fabric to the deposition of a thermoset prepreg, the material can be described as visco-hyperelastic. In the work of Kelly et al. [76], the compaction of

composite was modeled component with two parts: an elastic model and a viscous model. Furthermore, the viscous component is a function of strain and strain rate. The elastic model for the composite was derived from the works of Limbert and Middleton [28] where they modeled soft connective tissue using transversely isotropic visco-hyperelastic constitutive equations. The same principle can be applied to the fiber reinforced composites which exhibit transverse isotropy and show viscous properties during curing and compaction.

The Cauchy-Green tensor can now be used to define the Piola-Kirchhoff stress tensor shown in Eq. 22. To derive the elastic component, the five invariants of the Cauchy-Green tensor will be used to simplify the stress tensor.

$$I_1 = 2{:}\hat{C}, I_2 = \frac{1}{2}\left[I_1^2 - \left(1{:}\hat{C}^2\right)\right], I_3 = \det\left(\hat{C}\right), I_4 = \vec{N}_0{:}\hat{C}, I_5 = \vec{N}_0{:}\hat{C}^2 \tag{22}$$

By deriving the invariants with respect to C, the Piola-Kirchhoff stress tensor can be solved as show in Eq. 23.

$$S = 2\psi_1 I + 4\psi_2 \hat{C} + 2I_3\psi_3\hat{C}^{-1} + 2\psi_4 \vec{A}\otimes\vec{A} + 2\psi_5(\hat{C}\vec{A}\otimes\vec{A} + \vec{A}\otimes\hat{C}\vec{A}) \tag{23}$$

Where A is the fiber direction. This equation can be pushed forward to derive the Cauchy stress tensor to be used directly in the FEA as shown in Eq. 24.

$$\sigma = \frac{2}{J}\left(\hat{F}\cdot\frac{\partial\psi^e}{\partial\hat{C}}\cdot\hat{F}^T\right) + \sigma^v \tag{24}$$

To simulate the compaction process, the model employs visco-hyperelastic equations to represent the flow of the ungelled resin [72]. The compaction model comprises both an elastic and a viscous component. For the elastic component, a transversely isotropic hyperelastic equation is employed, applicable to fiber-reinforced composites. The model utilizes five invariants of the Cauchy-Green deformation tensor as shown previously.

$$\sigma = \sigma^e + \sigma^v = 2\left(\frac{\partial \psi^e}{\partial \hat{C}} + \frac{\partial \psi^v}{\partial \dot{\hat{C}}}\right) = 2\sum_{\alpha=1}^{5}\left(\frac{\partial \psi^e}{\partial I_\alpha}\frac{\partial I_\alpha}{\partial \hat{C}}\right) + \sigma^v = \frac{2}{J}\left(\hat{F}\cdot\frac{\partial \psi^e}{\partial \hat{C}}\cdot \hat{F}^T\right) + \sigma^v \quad (25)$$

Through a push-forward operation, the stress becomes a function of the deformation gradient, $\hat{F}$, and its Jacobian, *J*. The fiber direction was solved using the linear-elastic behavior from the fiber instead of the homogenized composite since it is governed by inextensible fibers. The constitutive equation for the stress is given by eq. 26 [84].

$$\sigma_{11}^e = 2\mu_f \varepsilon_{11} + \lambda_f tr(\varepsilon) \quad (26)$$

where ε_{11} is the strain in the fiber direction and $tr(\varepsilon)$ is the trace of the strain. The constants μ and λ are related to the fiber material properties as

$$\mu_f = \frac{E_f}{2(1+\nu_f)} \quad (27)$$

$$\lambda_f = \frac{\mu_f \nu_f}{(1-2\nu_f)} \quad (28)$$

where E_f = 168 GPa and $\nu_f = 0.027$ are the modulus of elasticity and Poisson's ratio of the IM7 fiber, respectively.

For the transverse and shear properties, a transversely isotropic neo-Hookean model was used to calculate the stress of the current configuration. The strain energy potential used for the 2-3 plane for the stress is shown in eq. 29.

$$\psi^e = \frac{1}{2}\mu(I_1 - 3) - \mu\ln(J) + \frac{1}{2}\lambda(J-1)^2 + [\beta + \zeta\ln(J) + \kappa(I_4 - 1)](I_4 - 1) - \frac{1}{2}\beta(I_5 - 1) \quad (29)$$

I_1-I_5 are the invariants of the Cauchy Green strain tensor. The material constants, λ, μ, β , ζ, and κ, are material constants derived from the properties of the homogenized composites using eq. (30)-(36) [71], [85].

$$\lambda = \frac{E_{22}(\nu + n\nu^2)}{m(1+\nu)} \tag{30}$$

$$\mu = \frac{E_{22}}{2(1+\nu)} \tag{31}$$

$$\beta = \mu - G_{23} \tag{32}$$

$$\zeta = \frac{E_{22}\nu(1-n)}{4m(1+\nu)} \tag{33}$$

$$\kappa = \frac{E_{11}(1-\nu)}{8m} - \frac{\lambda + 2\mu}{8} + \frac{\beta}{2} - \zeta \tag{34}$$

$$m = 1 - \nu - 2n\nu^2 \tag{35}$$

$$n = \frac{E_{11}}{E_{22}} \tag{36}$$

where, E_{11} = 25 MPa and E_{22} = 1 Pa are the Young's modulus in the fiber and transverse to the fiber directions of the homogenized uncured composite to ensure the correct bending stiffness and the stability of the FEA, respectively. $\nu = 0.01$, and G_{23} = 1 MPa are the Poisson's ratio and the shear modulus of the homogenized composite, respectively [72]. The Cauchy stress tensor can then be derived by differentiating the strain energy potential and pushing forward with a double multiplication of the deformation gradient provided by Abaqus [71]. Since the flow and the hyperelasticity constitutive equations are dependent on the fiber direction, the fiber orientation is updated every step. A model assumed that the fiber orientation follows an affine motion based on the deformation gradient characterized by the following equation [86]:

$$\vec{P} = \frac{\hat{F} \cdot \overrightarrow{p_0}}{\left\| \hat{F} \cdot \overrightarrow{p_0} \right\|} \tag{37}$$

where $\vec{p}$ is the fiber direction vector and $\overrightarrow{p_0}$ is the initial fiber direction vector. The fiber direction is used to inform the anisotropic component of the hyperelastic model, where it becomes the variable for the function of stress based on the strain energy potential [77].

This works involves carbon fiber composites. NCFs have an interweaving pattern creating a quasi-isotropic ply which results in two directions being modeled as inextensible fibers. However, for the prepreg tape, the axial viscosity is significantly greater than the shear viscosity. Consequently, the unidirectional structure of the material exhibits transversely isotropic properties, which must be represented in the constitutive model. The difference comes from the viscous components of the model. For the non-crimp fabric, the viscous component comes from the architecture of the fabric [87], [88]. For most of the research, the material consists of a preimpregnated carbon fibers where the viscous component comes from the resin.

The microscopic fibers suspended in resin show time dependent behavior based on the strain rate effects and resin viscous behavior. Research from Kelly [76] used the multiplicative decomposition of apparent viscosity to describe the squeeze flow. To quantify the homogenized prepreg tape response, the proposed approach for the viscous term uses multiplicative components that consist of strain- and strain rate dependent terms [72], [76], [56]. The strain dependent terms take into account the ply geometry and the strain rate described the resin behavior [72]. The viscous stress term followed the behavior as shown in Eq. 38.

$$\sigma^{v}{}_{ij} = \eta_{rate\,ij} \cdot \eta_{ply_{ij}} \cdot \eta_{micro\,ij} \cdot \hat{\dot{\varepsilon}}_{ij} \tag{38}$$

where $\hat{\eta}_{rate}$ is a strain-rate dependent viscosity tensor component and $\hat{\dot{\varepsilon}}$ is the strain rate tensor. $\hat{\eta}_{ply}$ is the term responsible for ply geometry and $\hat{\eta}_{micro}$ is the phenomenological strain dependent term derived from micromechanical considerations at the micro level.

The major difference between added to the visco-hyperelastic model is a tensorial anisotropic viscosity to represent the strain rate dependent term. During the curing, the fiber-resin system can be assumed to function as a power-law viscous fluid. Previous work described the anisotropic viscosity of oriented discontinuous fibers suspended in Newtonian fluid [56]. The same principles may be applied to continuous fiber with a finite length. Therefore, when considering an assembly as shown in Figure 8 a tensorial viscosity approach was used to model the $\hat{\eta}_{rate}$ term where the resin matrix follows a power-law behavior. Since the composite tow is transversely isotropic, the in-plane directions (transverse to the fiber) were assumed to have the same properties, while the fiber direction is assumed to be inextensible.

The proposed rate term for the current study uses effective properties of the composite derived from the anisotropic viscosity as a function of strain rate, fiber volume fraction, and a power law exponent using the following tensor components. The constitutive equation for a power-law fluid (eq. 39)

$$\tau = \eta \dot{\gamma}^{m} + \tau_0 \tag{39}$$

Where τ_0 is the yield stress. This power law fluid constitutive equation can be combined with equations (24), (26), (28) and (31) in order to form the strain rate dependent tensor of the visco-hyperelastic constitutive model.

$$\eta_{rate_{11}} = \eta_{resin} 2^{-mf} \left[\frac{\sqrt{\bar{f}}}{1-\sqrt{\bar{f}}}\right]^{m} \left(\frac{L}{D}\right)^{m+1} \dot{\epsilon}_{11}{}^{m-1} \tag{40}$$

$$\eta_{rate_{22}} = \eta_{rate_{33}} = \eta_{resin} 2^{m+1} \left[1-\sqrt{\bar{f}}\right]^{-m} \dot{\epsilon}_{22}{}^{m-1} \tag{41}$$

$$\eta_{rate_{23}} = \eta_{resin} \left[1-\sqrt{\bar{f}}\right]^{-m} \dot{\gamma}_{23}{}^{m-1} \tag{42}$$

$$\eta_{rate_{12}} = \eta_{rate_{13}} = \eta_{resin} 2^{-m} \left[\frac{1-\sqrt{\bar{f}}}{1-\sqrt{\bar{f}}}\right]^{m} \dot{\gamma}_{12}{}^{m-1} \tag{43}$$

where $\bar{f}$ is the normalized fiber volume fraction, L is the fiber length, D is the fiber diameter and $m = 0.5$ is the power law exponent.

The ply geometry term is derived from an analytical solution by Rogers [70] and describes the geometry and surface conditions of the ply. A frictionless boundary condition was assumed for the solution since the scope of the curing and compaction has the resin as a fluid. A solution to the work, rearranged by Belnoue et al. [72], was used in this study, as shown in the equations below.

$$\eta_{ply_{11}} = \hat{\eta}_{ply_{12}} = \hat{\eta}_{ply_{13}} = \hat{\eta}_{ply_{23}} = 1 \tag{44}$$

$$\eta_{ply_{22}} = 2\left(\frac{w_0}{h_0}\right)^2 e^{-4\varepsilon_{22}} \tag{45}$$

$$\eta_{ply_{33}} = 2\left(\frac{w_0}{h_0}\right)^2 e^{-4\varepsilon_{33}} \tag{46}$$

where w_0 is the initial width of the ply, and h_0, is the initial height of the ply. The ply term describes the squeezing or the transverse expansion of a tow with geometry based on the tow geometry as shown in Figure 12.

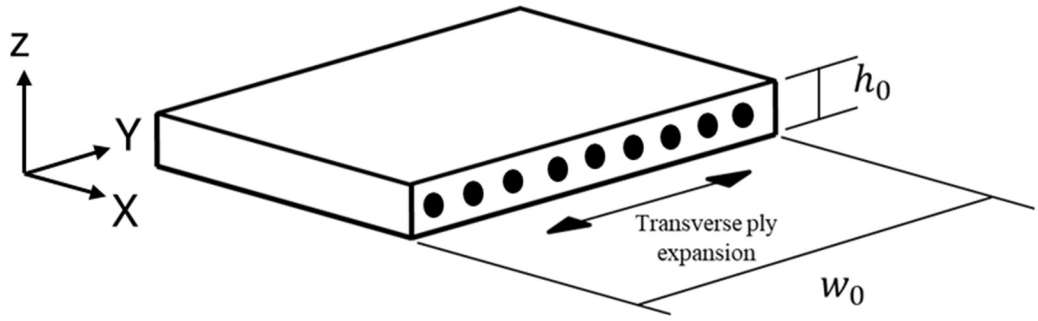

Figure 12. The geometry of the composite tow describes the expansion of an individual tows or the whole ply with the dimensions h_0 and w_0

The next term in the visco-hyperlastic equation considers the flow of the resin through the, η_{micro} is derived from micromechanical consideration. Belnoue considered the different types of packing from Hubert and Poursatip [89], where the flow of the resin through the unit cell of the tow is approximated in a phenomenological equation. Essentially, this term replaces the conventional modeling of Darcy flow through the fibers and simplifies the phenomenon in the modeling framework. An approximation of the fiber architecture can be implied using the strain and the shearing strain of the equation. As the gap between the fibers decreases the apparent viscosity increases. The η_{micro} also relies on the phenomenological parameters that govern the flow regimes between an incompressible solid to a compressible one due to resin bleed out in the fiber direction as a result of fiber locking during compaction [90].

$$\eta_{micro_{11}} = \eta_{micro_{12}} = \eta_{micro_{13}} = \eta_{micro_{23}} = 1 \tag{47}$$

$$\eta_{micro_{22}} = 2\sqrt{\chi_l} e^{\varepsilon_{22}} k \left(\left(\frac{k}{\sqrt{\chi_f} e^{\varepsilon_{22}} - k} \right)^2 + 3 \right) \tag{48}$$

$$\eta_{micro_{33}} = 2\sqrt{\chi_l} e^{\varepsilon_{33}} k \left(\left(\frac{k}{\sqrt{\chi_f} e^{\varepsilon_{22}} - k} \right)^2 + 3 \right) \tag{49}$$

where, $\chi_l = 0.63$ is the aspect ratio during locking and $\chi_f = 0.785$ is the final aspect ratio based on the maximum packing fraction of the composite [91]. The packing in this case is interpreted as the fiber volume fraction. This viscosity describes the behavior of the resin flowing through the fibers as unit cell shown in Figure 13. This flow viscous terms controls the compressibility of the material and can change its properties if there is a change in flow regime.

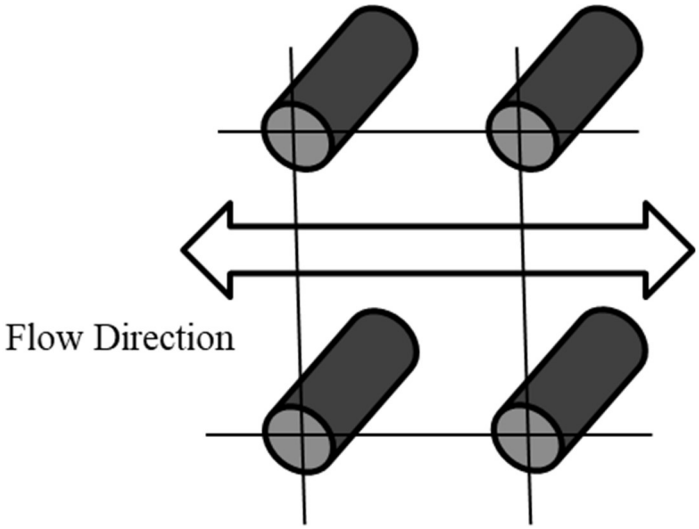

Figure 13. The unit cell of the flow through the fibers for a typical fiber reinforce composite.

3 Methodology

3.1 Non-crimp fabric compaction

The focus of this research involves NCFs which maintain their fiber orientation unlike conventional woven composites. This allows the fabric to maintain its strength since the fibers allow for better load transfer and reduces stress concentrations. However, NCFs experiences wrinkling and local variations of fiber volume fraction when compacted. These directly influence the permeability and affect the resin infusion process. The manufacturing processes for NCFs comprise of a fiber preform, a mold, a press and resin injection system infusing resin called resin transfer molding (RTM). The manufacturing process utilizes a mold, which allows for the rapid manufacturing of a part. A variation of this method used in the automotive industry is high pressure RTM (HP-RTM), which has a faster cycle time due to the large pressure placed on the fiber bed. This process has been frequently used in commercial industries such as the automotive industry to manufacture seat backing, and leaf springs (Fig. 1a). Since the NCFs needs to be infused with resin, the permeability of the fiber bed becomes an important factor for the manufacturing process of the textile-based composites structures.

One of defining factors for the quality of a NCFs is the integrity of the resin infusion. This makes the permeability of the weave a critical factor when processing the textile. Furthermore, research indicates that the behavior of resin infusion depends on in response to fabric deformation [69]. Monitoring the fiber volume fraction of a laminate during the manufacturing process is difficult. However, it can be predicted using an FEA model. This research was first originally presented at SPE ACCE 20 [10]. The experimental data was derived from the collaboration with

Laredo [9]. The data was fitted into a rudimentary constitutive model and fiber volume fraction equation for the convention. It managed to showcase a gradient of the fiber volume fraction and the potential for the simulation of NCFs with respect to fiber volume fraction prediction and wrinkling between the quasi-isotropic plies. However, the constitutive model of the NCF compaction has been improved with a larger fidelity with a reasonably quick model. The constitutive model was developed data from the same compaction experiments of NCFs. These models would be able to predict the variability of the fiber volume fraction and the morphology, such as fiber redistribution or reorientation, during the compaction process.

3.1.1 Compaction of a non-crimp fabric experiment

The compaction test analyzed several variables, including thickness, sample dimensions, compaction speed, and the number of testing cycles. Of these, initial and final thickness are likely the most critical, as pre-compacted areas of the fabric may introduce flaws and defects during or after the curing process. The resin flow is affected by the gradient of fiber volume fraction. The evolution of the fiber volume fraction during compaction is further affected by multiple factors such as the total compaction and the rate of the compaction. The data from compaction experiments done by Laredo was used to establish a constitutive model for the compaction of NCFs [9].

The compacted material was Saertex multiaxial non-crimp fabric with a layup configuration of [+45/-45/0/90/0/-45/+45] where the layers are held together by a polymer thread as shown in Figure 14a. This results in a fabric without any crimping or undulations unlike other woven fabric (Figure 14b). The fabric's dimensions and the crosshead velocity were varied in the experiments. The samples of NCFs were 152 mm x 152 mm in length and width. The 152x152 mm samples had an average thickness of 3.94 mm, and samples 4-6 had an average thickness of

8.08 mm. The wider samples had an overall average thickness of 4.00 mm and 8.18 mm. The NCF's thickness was varied between 4- and 8- mm, where each quasi-isotropic layer was 2 mm.

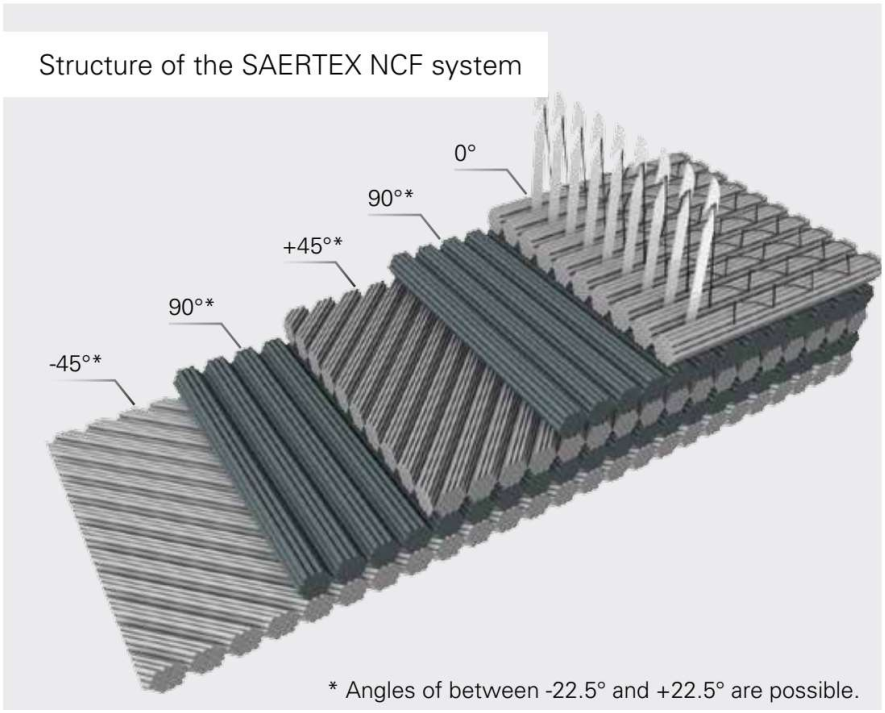

(a)

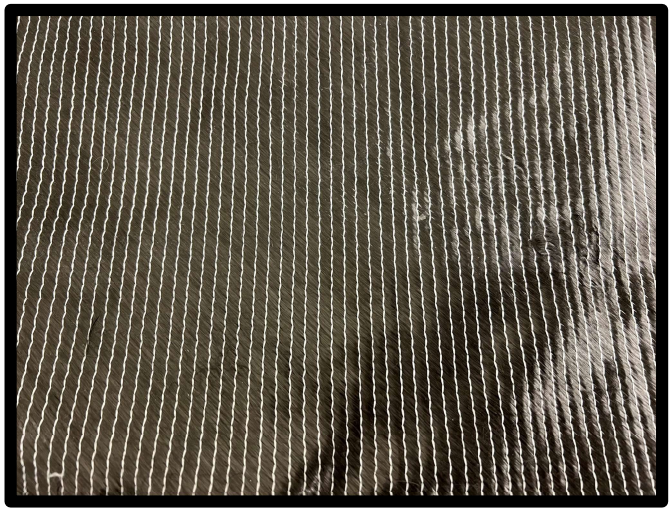

(b)

Figure 14. a) Schematics of the of the stitching of the NCF and the stacking sequence. b) What top surface of the non-crimp fabrics with the nylon stitching

The compaction rate of 1, 2, and 5 mm/min was set on the Tinus Olsen 10ST universal testing machine. The fixture consisted of two circular platens with the top platen having a diameter of 48.32 mm and the bottom platen having a diameter of 147.32 mm (Figure 15). Mitsuyo calipers were used to measure the thickness of the sample before the experiment. The data was recorded at a frequency of 10 Hz where the data was used to calibrate a visco-hyperelastic model. However, it is difficult to observe the compaction process during the rapid process especially with different molding geometry used in the manufacturing process [4]. Therefore, to eliminate the trial-and-error process, a digital twin can be constructed using numerical modeling. These models will be able to predict the compaction fiber orientation and the fiber volume fraction in the NCF and predict the permeability to replicate the resin infusion. With the multiple components of the HP-RTM, a digital twin can be developed from the preforming to the finished product of an NCF.

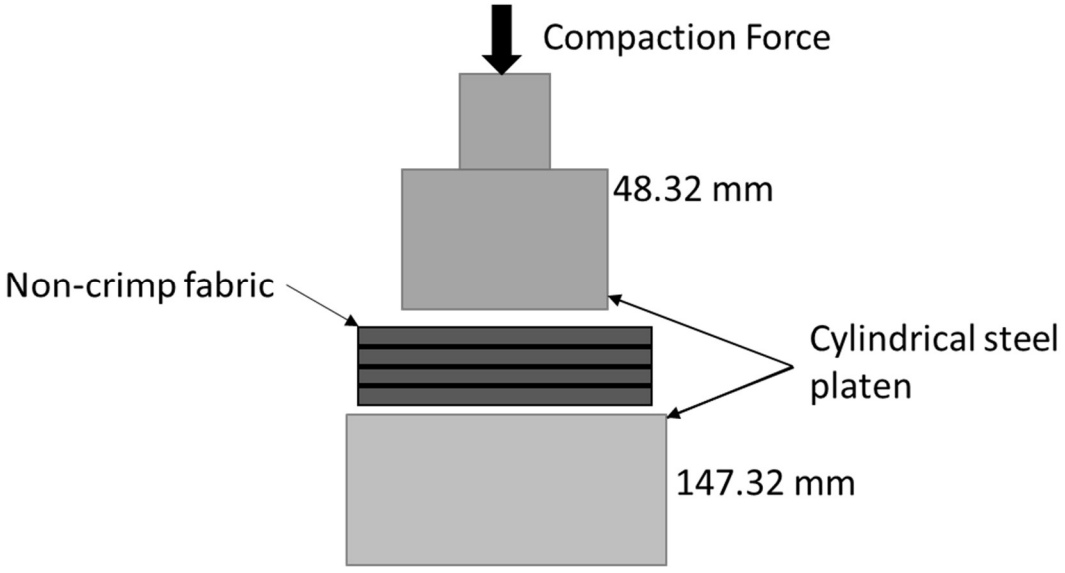

Figure 15. Image of the quasi-isotropic layers of non-crimp fabric and the stitching

3.1.2 Constitutive model for compaction of a non-crimp fabric

In the present constitutive equation, the quasi-isotropic arrangement of the non-crimp fabric displayed transversely isotropic characteristics. Specifically, across the thickness, the material formed bundles of fibers demonstrating viscoelastic properties [76], [92]. While within the plane, the fibers exhibited linear elasticity with a high modulus to reflect their inextensibility. Thus, the proposed approach for the constitutive model of the non-crimp fabric involves a superposition of two stress components—an elastic component and a viscous component, as depicted in eq. 25.

It was assumed that the stress and strain within the plane exclusively adhered to the linear elasticity of the carbon fibers. Hence, the in-plane behavior was characterized by a generalized Hooke's law equation to represent the elastic component of the constitutive model, as illustrated in Eq. 26 [14]. However, young's modulus is affected by the fiber volume fraction through the rule of mixtures. The mechanical properties of the fiber are derived from data sheet for the carbon fiber Zoltek PX35, which has properties shown in table 1 [93].

Table 2. Properties for Zoltek PX35	
Tensile Modulus	242 GPa
Density	1.81 g/cc

The fiber bundles in the weave exhibit a time-dependent stress-strain relationship for compaction. Hence, an apparent viscosity was applied to simulate the compaction of the non-crimp fabric. The constitutive equation proposed by Kelly, originally intended for plain weave textiles, was adopted for modeling the compaction process of the non-crimp fabric, employing similar principles [6]. Experimental stress-strain data of non-crimp fabric was utilized to derive the

viscous. The formula derives a multiplier for a reference stress-strain curve which makes a multiplicative apparent viscosity term as shown in eq. 3.

$$\sigma_{33} = \sigma_v(V_f, v) = \sigma_\beta(V_f)\sigma_\alpha(v) \tag{50}$$

The fiber volume fraction, V_f, serves as the variable for strain, while the crosshead velocity, v, serves as the strain rate. The expressions were derived by analyzing the experimental stress-strain behavior of the non-crimp fabric under various compaction speeds. In this study, it was assumed that the fiber volume fraction and the strain are directly correlated. Thus, an exponential equation representing the strain-dependent term could be fitted to an experimental curve using median parameters, as illustrated in Eq. 4.

$$\sigma_\beta(V_f) = \beta_1^{\beta_2 * Vf - \beta_3} + \beta_4 \tag{51}$$

where $\beta_i, i = 1{,}5$ taken from a single experiment. In this case, the data was fitted at a reference compaction speed of 2 mm/min of a 152 x 152 mm, 4 mm thick laminate as the reference. The function, with parameters shown in Table 2, was compared to the experimental data which showed good correlation between the two curves (Figure 16).

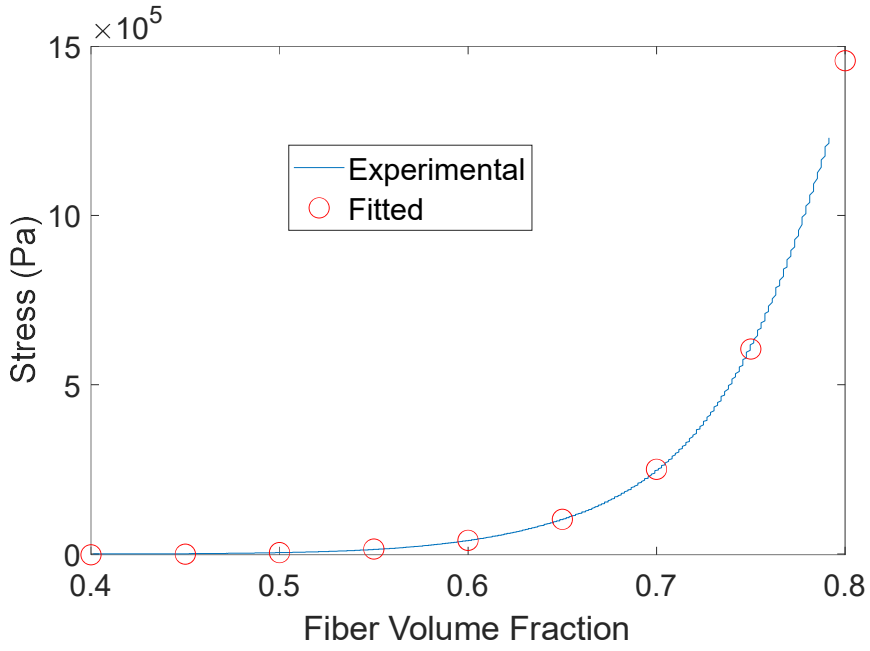

Figure 16. The compaction curve of 152 x 152 mm, 2 laminates, at 2 mm/min compaction speed with respect to the fiber volume fraction.

The experimental investigation also reveals a correlation with strain rate, with higher velocities resulting in greater stress. Nonetheless, this trend follows a consistent exponential trend. A scaling factor was formulated to account for the strain rate's influence, thereby standardizing various velocities into a single master curve. This rate-dependent factor was derived from the stress values across different compaction curves, using a reference fiber volume fraction of 0.60, as depicted in Figure 17. The stresses corresponding to the reference fiber volume fraction were fitted using the following equation:

$$\frac{\sigma(v)}{\sigma(0)} = \frac{\sigma(\infty)}{\sigma(0)} - \left[\alpha_1 \left(\frac{v}{v_{ref}}\right)^{\alpha_2} + \left(\frac{\sigma(\infty)}{\sigma(0)} - 1\right)^{-\alpha_3}\right]^{\frac{1}{\alpha_3}} \tag{52}$$

Where σ(0) represents the minimum stress observed at the lowest speed (1 mm/min), and σ(∞) indicates the maximum stress recorded at the highest speed (5 mm/min). v_{ref} denotes the

compaction speed utilized to fit Eq. 47, which stands at the midpoint between these two extremes (2 mm/min). The parameters derived from fitting, namely $\alpha_1, \alpha_2\alpha_3$, $\sigma(0)$ and $\sigma(\infty)$, are presented in Table 2. This equation facilitates the normalization of stresses according to the specified simulation velocity.

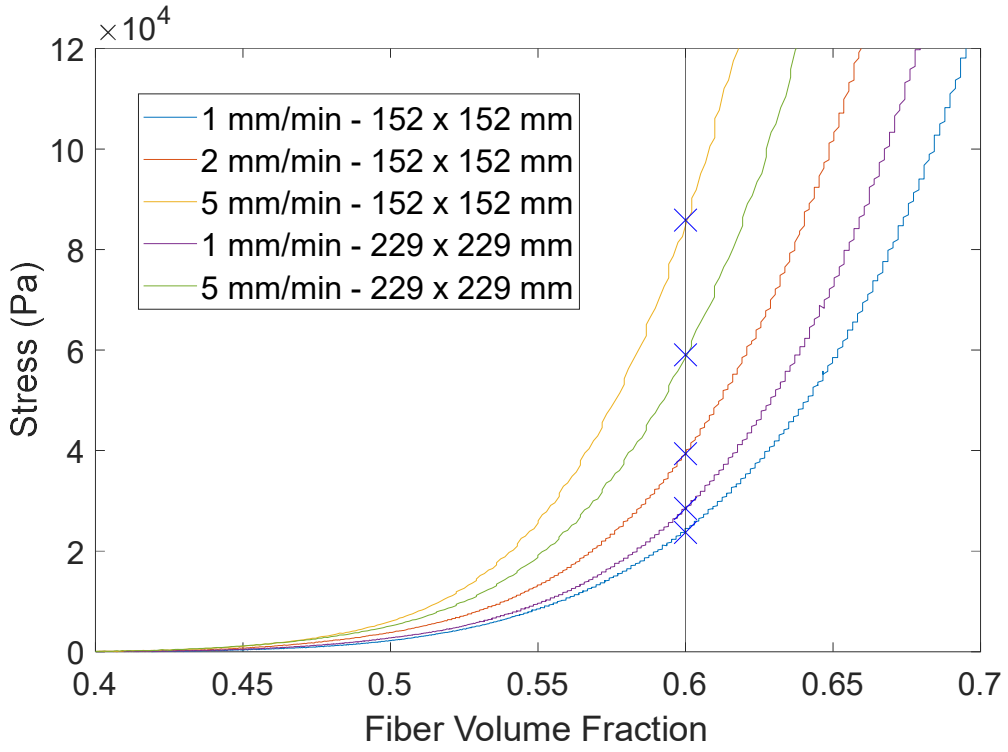

Figure 17. The compaction curves were used for the strain rate-dependent analysis.

Table 3. Fitted parameters for the composite material used in the work			
β_1	9.6605E4 Pa	α_1	0.1254
β_2	1.5238 Pa	α_2	3.2054
β_3	-0.0176 Pa	α_3	1.6507
β_4	-2.254E3 Pa	$\sigma(\infty)$	8.5829e4 Pa
V_f^{dat}	0.60	$\sigma(0)$	2.3726e4 Pa
v_{ref}	2 mm/min		

One assumption made in this study was the direct correlation between fiber volume fraction and through-thickness strain. Predicting the distribution of fiber volume fraction throughout the thickness is crucial for understanding the effects of compaction on composite weaves. An analytical solution was employed to homogenize multiple layers of quasi-isotropic non-crimp fabric into a single analytical solution. This relationship can aid in calculating the layers at the onset of the simulation. Before compaction begins on the non-crimp fabric, the composite thickness is measured. Using the areal density of the fabric and the known density of the fibers, the initial fiber volume fraction is calculated (Eq. 6).

$$V_{f_0} = \frac{\rho_a n}{\rho_f T} \tag{53}$$

In the equation, ρa represents the fabric's areal density, n is the number of laminates in the sample, ρf signifies the density of the specific fiber, and T denotes the sample's thickness. For the textiles employed in this study, the values are as follows: ρa=1425 g/m^2, ρf=1.79*10^6 g/m^3 and n=1, as the fiber volume fraction is computed for each layer. As the material undergoes compression, the fiber volume fraction increases. Previous studies have demonstrated that this increase can be expressed as a function of the logarithmic through-thickness strain. Consequently, for each time increment, the fiber volume fraction can be determined using Eq. 7. [94], [95].

$$V_f = V_{f_0} e^{\varepsilon_{33}} \tag{54}$$

The through-thickness strain, denoted as ε_{33}, is directly obtained from the subroutine, while V_f represents the fiber volume fraction at the current time step, and V_0 denotes the initial fiber volume fraction calculated using Equation 5. This assumption in the fiber volume homogenizes the non-crimp fabric into a single element through the thickness Figure 18.

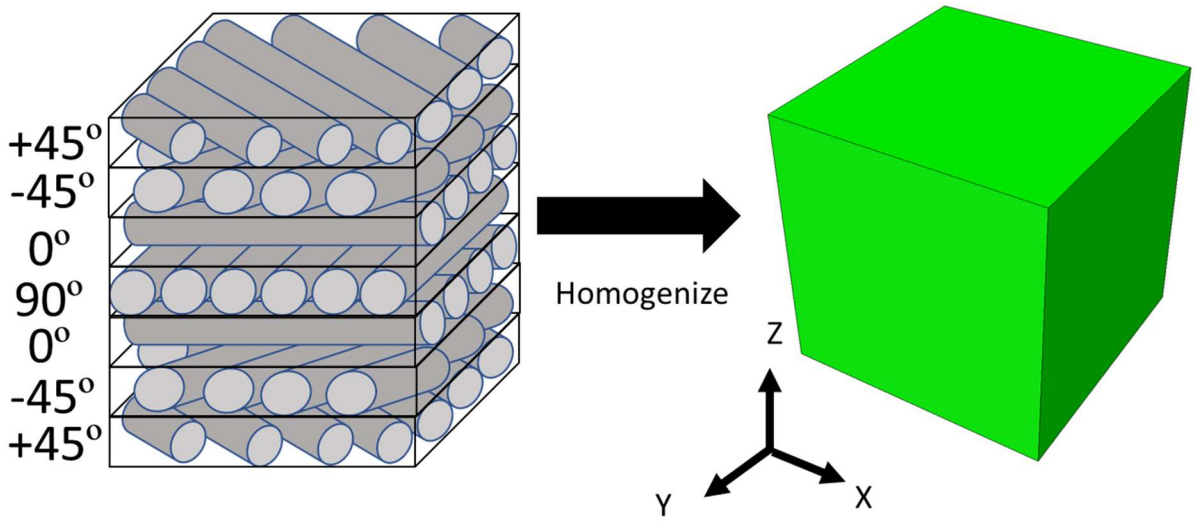

Figure 18. The non-crimp fabric was assumed to be homogenous to fit the assumption of the fiber volume fraction evolution based on the areal density of the material

To simulate the compaction of a NCF in HP-RTM, a FEA model was developed. The model comprises an NCF with four layers of quadaxial fabric, each 8 mm thick. A downward compaction force was applied to the roller. The pressure was applied with a 5 mm diameter tip (Figure 19a). Three different velocities—1 mm/min, 2 mm/min, and 5 mm/min—were applied to the roller, mimicking experimental conditions. The NCF was discretized into 52010 C3D8R elements, with frictionless boundary conditions set between each layer. For testing the stress-strain response, single-element tests were conducted. Similar to the single-element compaction, the model was constrained vertically in the through-thickness direction to simulate the tool used in the experiment (Figure 19b). The roller was modeled with steel properties, including a Young's modulus of 215 GPa, a Poisson's ratio of 0.3, and a density of 7.85 g/cc.

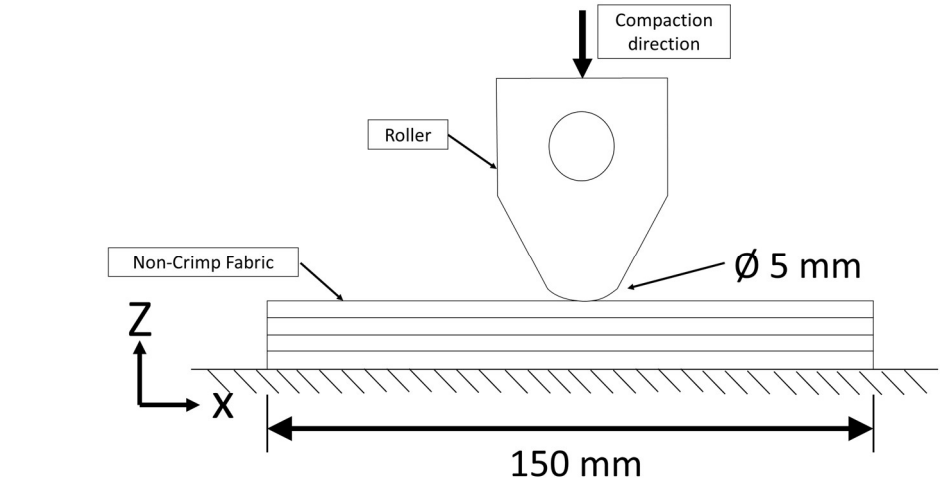

(a)

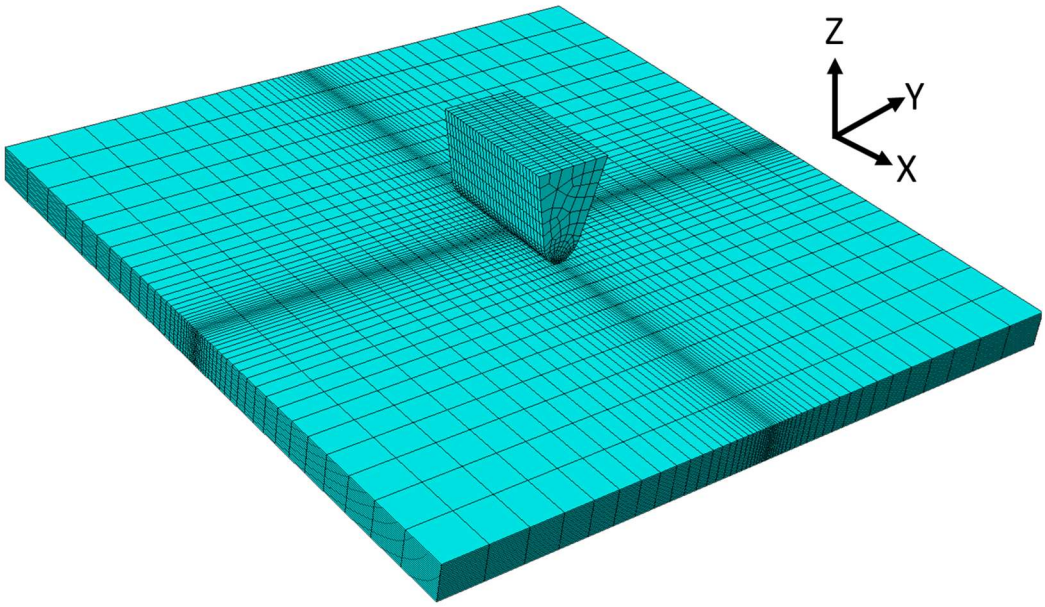

(b)

Figure 19. a) The schematics of the roller compaction and b) The FEA model of the roller and the NCF fabric

3.2 Pre-preg roller compaction

Prepreg composite are unidirectional fibers infused with resin which comes in strips or sheets. These composites are placed on molds with the desired geometry of the composite structure. Since these composites comes with the resin already active, they are frozen in order to stop the curing of the resin before its usage. This results in the need for refrigeration to store these types of composites compared to dry fabrics which can be stored indefinitely. The strength of prepreg composites strips comes from the versatility and automation of the process. The thin strips allow for an additive manufacturing process which are preprogrammed and operated via a robotic arm. Processes such as AFP allow for versatility in the fiber directions throughout the laminate.

One study in the overall research involves the transverse spreading of these tows when it is deposited on either a metal or composite substrate. As of this moment, the work is being edited in order to be released into a journal to publish the work. However, the work was originally presented in SAMPE 2023 [96]. Where the testbed for the roller was presented along with preliminary results deformation and the heat transfer models. The model has improved to accommodate the deformation and the heat transfer of increasing composite substrate layers.

3.2.1 Roller deposition experiments

Experiments were conducted on unidirectional samples with varying compaction force and laminate prepreg thickness. A robotic system was utilized to deposit composite tows via a heated roller, laying tows on increasing layers of composite substrates. The AFP deposition process was implemented using the Sawyer 7 DOF robotic manipulator, featuring a custom-designed end-effector (Figure 20a). More specifically, the mechanical structure of the end-effector housed three modules: 1) a roller used to apply compaction and pressure on the prepreg tape, 2) a centrally positioned heating element within the roller, and 3) a prepreg tape feeding system. The feeding system frame was designed and 3D-printed using a rigid polymer and mounted onto the Sawyer robot's end-effector flange (Figure 20b). The middle section of the feeding system was attached to the roller module, and the upper section consisted of a spool that housed and fed the prepreg tape to the roller. The roller itself featured a pair of ball bearings encased within a 3D-printed rubber cylinder, securely mounted onto the robot's end-effector flange through a 3D-printed holder. The hyperelastic rubber, manufactured by 3M, was wrapped around the cylindrical roller. To achieve temperature control of the roller, a microcontroller-based hardware electronics system was prototyped. This system utilized a ceramic cartridge-based heating element housed in a copper tube concentric to the roller shaft. A potentiometer allowed for the setting of the desired temperature, while a thermistor sensed the current temperature of the heating element. Finally, a microcontroller utilized the inputs from the two components to regulate the temperature through a Proportional-Integral-Derivative (PID) controller.

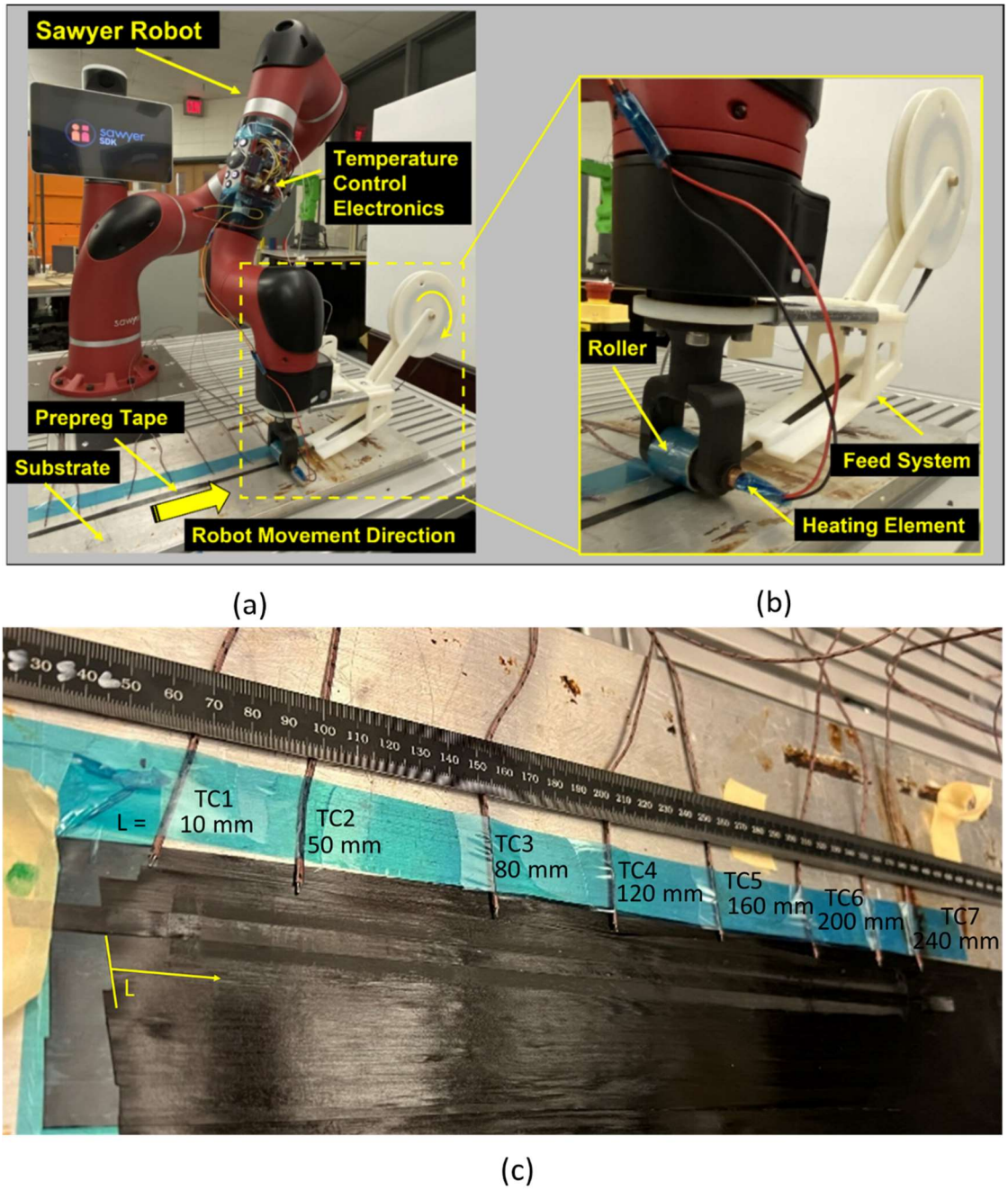

Figure 20. a) The components of the robotic roller compaction setup with feeding mechanism b). The robotic end effector with tape feeding system; c). The experimental setup of the aluminum tool plate with the thermocouple attached to the substrate. The distances from the origin of the roller are labeled for each thermocouple.

The Sawyer robotic arm was used to reproduce deposition step in the AFP manufacturing process. To control the robotic arm with the fiber tow deposition end effector, the Robot Operating

System (ROS) was used directly to program the path planning of the Sawyer robot movements, where the kinematic motion and force data from the robot were also collected. With full control of its programming, the developed deposition system simultaneously laid the tows and provided feedback data for parameters such as compaction force and speed. The controller and databank used a computer with a Linux operating system, which stored and visualized the operational feedback data. The robotic system allows an accessible testing environment to investigate the effects of AFP parameters on the deformation of the deposited tow.

To aid in experimental measurements of tow spreading, the tow prior to roller compaction was deposited on the substrate of interest, such as uncured prepreg laminate or aluminum tool. While the robotic setup was able to feed the tow, this particular experiment opted not to utilize the feeding system to facilitate a more straightforward comparison between the undeformed and deformed tows both before and after the experiment. Otherwise, due to the natural stochastic variation in tow width, it would have been hard to track the changes in tow deformation. Instead, the tow was aligned along a path which the robot's end-effector moved parallel to, while maintaining orthogonal contact with the fiber direction of the tow. Minor tension was applied near the starting point of the roller to secure one end of the tow as the roller moved across the fiber direction. Thermocouples were aligned along the roller path, about 6 mm away from the tow edge and spaced along the length of the tow to monitor the heat induced by the roller as it passed, as shown in Figure 20c. The roller's core temperature was set to 80ºC and allowed to reach roller surface temperature of about 60ºC.The material used was Hexcel's IM7/8552-1 prepreg tape was selected due to its compatibility with AFP technology, as the 8552-1 epoxy resin is specifically designed for the AFP process. Compared to the original 8552 resin, the 8552-1 variant has a lower tack, reducing the potential for fiber tow wrinkles during steering. he IM7 carbon fiber (12K, G

sizing) features a fiber areal weight of 0.04 lb./ft². The IM7/8552-1 prepreg tape, with a cured ply thickness of 0.0072 inches per ply and a resin content of 33 ± 2% by weight, was fabricated at Hexcel Corp in Salt Lake City, UT, and slit at Web Industries in Atlanta, GA. The prepreg laminate was made of T700S carbon fibers and epoxy resin, supplied by RockWest.

In prepreg laminate, the After the initial compaction of the roller, the crosshead moves across a pre-programmed path which deposits more of the material. The laminate thickness varied, consisting of 0, 2, 5, and 10 prepreg layers, while the aluminum tool had a thickness of 13 mm. The applied compaction forces during the deposition experiment were 10 N, 30 N, and 50 N. To record the undeformed dimensions of the tow, the tow was laid on the uncured prepreg laminate of a given thickness, allowing pictures to be taken at specific locations 100 mm, 150 mm, and 200 mm along the tow length for each case using a Dino-Lite Edge 3.0 digital microscope. Next, deposition pressure was applied via the roller, which moved at a speed of 50 mm/s for a total length of 300 mm for each case. The deformed tow configuration was recorded afterward by taking pictures at the same locations (Figure 21). The changes in the width of the tow and corresponding transverse strain were measured using the image processing program ImageJ.

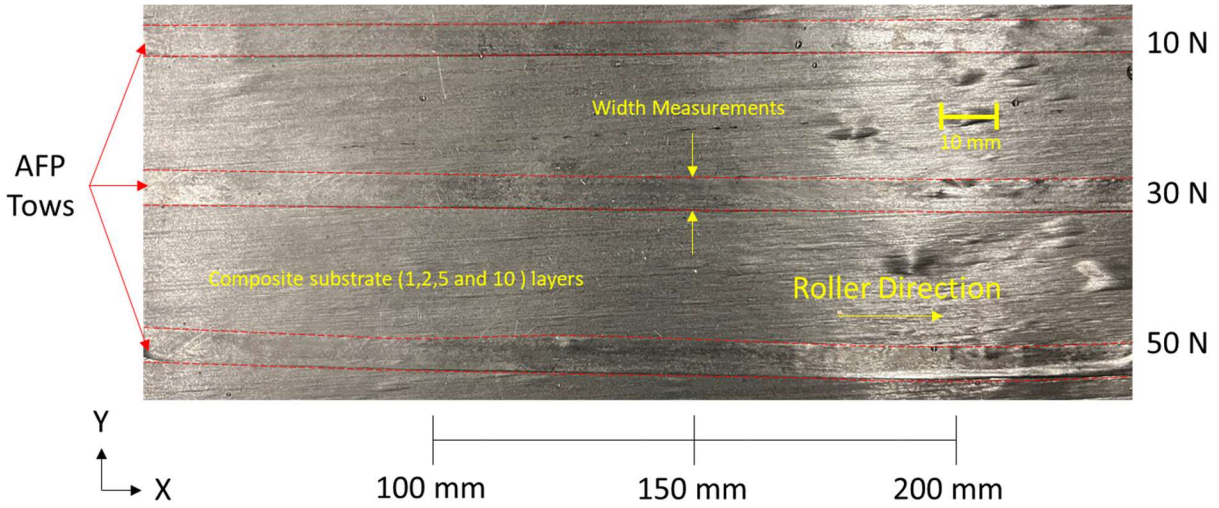

Figure 21. Top view on prepreg tows after roller compaction with different force levels

3.2.2 Hyper-viscoelastic constitutive behavior of prepreg tow during roller deposition

To understand and predict the experimentally observed behavior, the present research utilized a multi-physics computational model that captured hyper-viscoelastic deformation of the tow and the transient heat transfer during deposition [97]. The model utilizes the chemo-rheological model despite the minuscule increase in degree of cure during this phase. The heat transfer model wrapped around the heat transfer may be utilized to analyze the temperature distribution throughout the laminate (Figure 22). Finally, the same stress deformation model can be utilized to predict the spreading of the tow, since the stepwise function of the model allows for the range of temperature present in the deposition of the tow.

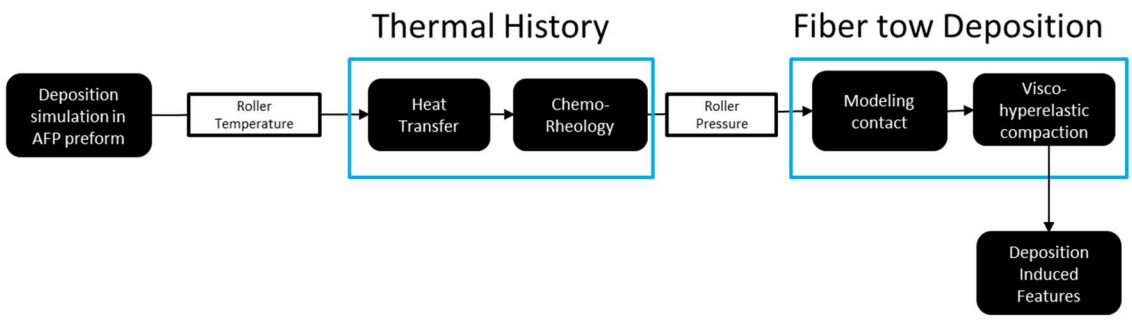

Figure 22. A simple constitutive model for the deposition of composite plies

A finite element model was developed to simulate the fiber tow deposition experiment. The roller model used neo-Hookean hyperelastic properties with C_{10} = 248.4, and D_1 = 1.0, and consisted of 58,560 C3D8RT elements. The density of the rubbery material was 0.0443 kg/m³. A rigid cylindrical core, modeled as an undeformable shell with a radius of 10 mm, was used at the center of the roller. The cylindrical core was surrounded by hyperelastic rubber with a radius of 40 mm. Instead of heat originating from this core, a temperature boundary condition of 60ºC was applied to the surface of the roller since the roller was allowed to reach a steady state temperature during the deposition experiments. The initial temperature of the tow and the composite substrate was 20ºC. A reference point at the midpoint of the rigid core was used to apply the force and displacement boundary conditions.

The tow used the constitutive properties from our previous research, which employed the same material system [98]. The density of the prepreg was 1590 kg/m³. The tow was 6.25 mm wide and 100 mm in length, consisting of 10,200 C3D8RT elements to couple the deformation and heat transfer through the prepreg. The experimentally measured temperature was used to calibrate the thermal conductance between the roller and the tow in the FEA model (Table 3). The thermal conductivity of the tow was 4.900 $W \cdot m^{-1} \cdot K^{-1}$ in the fiber direction and 0.584 $W \cdot m^{-1} \cdot K^{-1}$ in the

matrix-dominated directions. A surface film condition was used on the tow closest to the tool to simulate the heat transfer between the composite tow and the rigid tooling. The film had a coefficient of 180 $W \cdot m^{-1} \cdot K^{-1}$ to simulate the high thermal conductivity of aluminum.

Table 3. Heat conductivity constants.

Prepreg Density	1590 kg/m^3
Thermal conductance – Roller to substrate	583.5 kW/K
Surface film condition - Composite substrate to rigid tool	180 kW/K
Thermal Conductivity – Composite – Fiber Direction	4.900 $W \cdot m^{-1} \cdot K^{-1}$
Thermal Conductivity – Composite – Transverse Direction	0.584 $W \cdot m^{-1} \cdot K^{-1}$
Specific Heat – Composite	904.3 $KJ/kg^{-1} \cdot K^{-1}$

The heat transfer between the roller and the tow influences the compaction behavior of the tow and the prepreg laminate. This, in turn, affects the squeeze flow and the elastic recovery of the tow during compaction. The aluminum plate was modeled as a deformable solid with linear elastic and thermal properties. Each surface had a friction coefficient of 0.3 for the boundary conditions between the substrate and the tow. The assembly of the FEA model is shown in Figure 23, where a unidirectional tow is compacted by a roller. Two steps were created for the roller compaction: an initial step (1s) to apply the specified downward force of 10 N, 30 N, and 50 N, and a second step where the roller moved across the 300 mm length (6s) at a velocity of 50 mm/s. Finally, the roller was lifted from the tow, which was allowed to recover for one second. Measurements were taken at the same location as the experiment, and both results were compared.

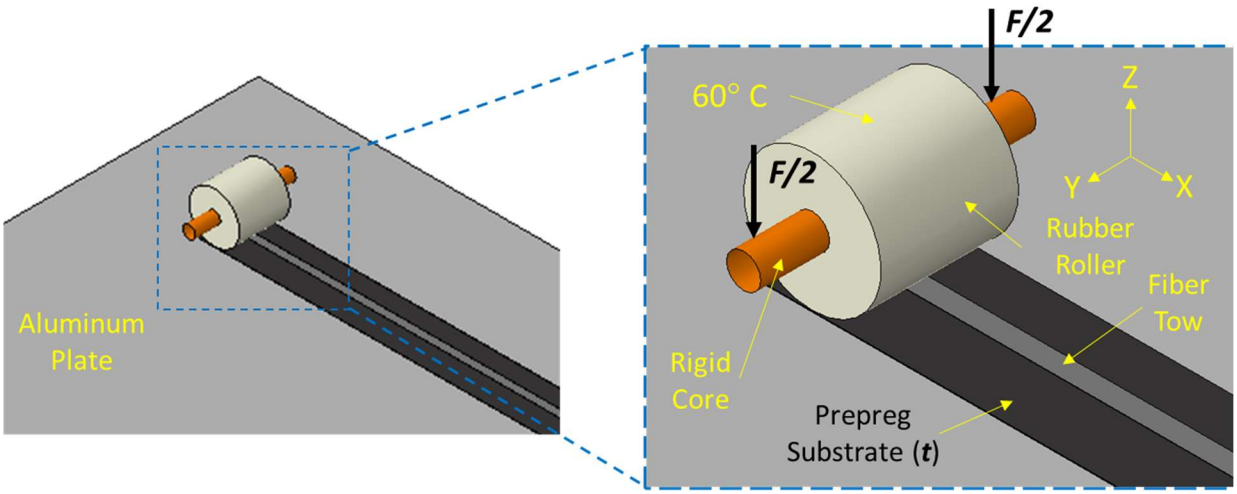

Figure 23. The finite element model for the roller compaction.

3.3 Resin Bleed out in laminates in single gaps

After the deposition of the tow, the laminate goes through a curing process to solidify the resin. However, the features produced from the deposition of the composite tow may result from inaccuracies in the tow placement. This work continues from the previous manufacturing stage, where the spreading of the tow would have left fiber tow gaps or overlaps. These features may be left purposely on the laminate or otherwise. However, the presence of these defects causes a non-linear deformation during the curing process [27], [34], [99]. The initial work of the model with a single tow gap was first introduced as a master's thesis. Later an improved version of the study was presented at AIAA SciTech Forum 2022 and a project for Virginia Space Grant Consortium which introduced the concept of the visco-hyperelastic models to represent the deformation of composites [52], [100]. Since the original concept, the work has expanded to encompass more physical phenomena which describes the deformation of the composite tow. This work is published in Polymers [97].

The visco-hyperelastic results in non-linear deformation in the composite tows. Furthermore, manufacturing defects occur during the early stages of curing and compaction, prior

to resin gelation, and significantly impact the mechanical properties of composites [23], [24], [25]. These imperfections often originate from deposition defects (Fig. 4) and stochastic material phenomenon, such as fiber misalignment and initial fiber volume fraction distribution. Layup issues, including gaps and overlaps, result in non-linear deformations and local morphological variations, such as ply thickness inconsistencies, waviness, and resin pockets. These defects decrease the overall strength of the composite (Figure 24). Such irregularities, which are inherent to the AFP manufacturing process, must be considered an integral aspect of AFP composites. Other studies have demonstrated that FEA can simulate various composite behaviors, such as rheology and residual deformation [53], [101], [102], [103]. Consequently, this approach was employed to predict the multivariable interactions within composites.

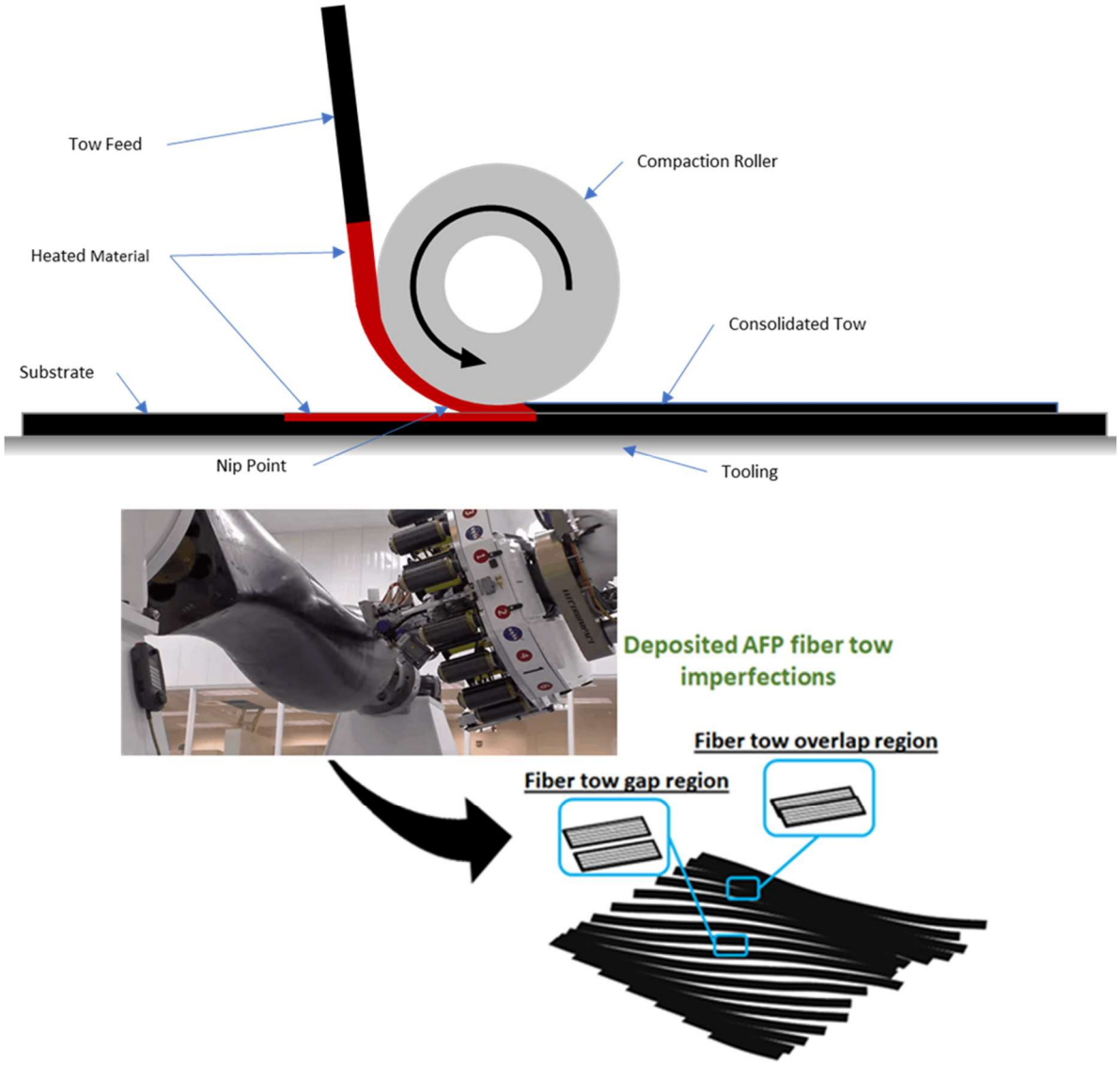

Figure 24. AFP systems and the resulting deposition features that lead to manufacturing defects

In composites with inextensible fibers, the transverse deformation is facilitated by the matrix. As the resin flows axially and transversely to the fibers during compaction, different flow regimes emerge. Specifically, squeeze flow involves the fiber tow deforming as a homogeneous medium, while percolation flow forces the resin through the fiber bed [54]. The squeeze flow develops when the fiber tow above the gap region is pushed into the void space during compaction, causing changes in fiber orientation due to the tow's waviness. Concurrently, resin from the

percolation flow forms resin-rich zones in the tow gap region, leading to a local increase in the fiber volume fraction of the composite. These microscopic changes in composite morphology significantly impact the composite's strength and result in a substantial reduction of its mechanical properties [24].

Although work has been done to characterize the individual contributions of these flow regimes during composite compaction, both phenomena often occur simultaneously [55], [56]. Therefore, a key goal of this section of research was to describe the impact of percolation flow in conjunction with squeeze flow during the early stages of the cure cycle. Experimental characterization of percolation flow was conducted to understand resin outflow before gelation.

3.3.1 Unidirectional tow compaction experiments

Experiments were conducted on unidirectional samples of varying geometries aimed at quantifying tow spreading and predicting resin bleed out from prepreg during compaction. The same prepreg as the compaction experiment, IM7-8552, was used for the experiment. Each tow measured to 6.57 mm in width and 0.14 mm in thickness. Compaction of the unidirectional tows was observed during the initial stages of manufacturing, specifically utilizing the first hold stage of the manufacturer's cure cycle. This phase involved maintaining a temperature of 110 ºC with an initial ramp rate of 3 ºC/min. A compaction pressure of 0.551 MPa (80 psi) was applied, increasing at a rate of 0.034 MPa/min.

The study encompassed six distinct configurations for the unidirectional samples, where variations in tow width and length were used across one, two, and four plies. Consequently, the thicknesses measured 0.14 mm, 0.28 mm, and 0.56 mm, while the corresponding widths were 6.46 mm, 12.92 mm, and 25.84 mm, respectively, with a constant sample length of 25.84 mm. For each

configuration, six samples were prepared, and experimental measurements were averaged to derive representative results. An example of each sample is shown in Figure 25a.

To analyze the tow spreading during curing, the dimensions of unidirectional samples were measured at 5, 15, 30, and 60 minutes into the hold stage by capturing images of the top x-y plane using a Dino-Lite Edge 3.0 digital microscope. Upon completion of the initial isothermal stage of the curing cycle, resin bleed out on the outer surface of the ply was identified (Figure 25b). The extruded resin was removed using a knife, and its mass was quantified via a sensitive mass scale. Images acquired throughout the curing cycles were analyzed to estimate the extent of resin bleed out both along the fibers and in the transverse direction relative to the fibers over the course of curing.

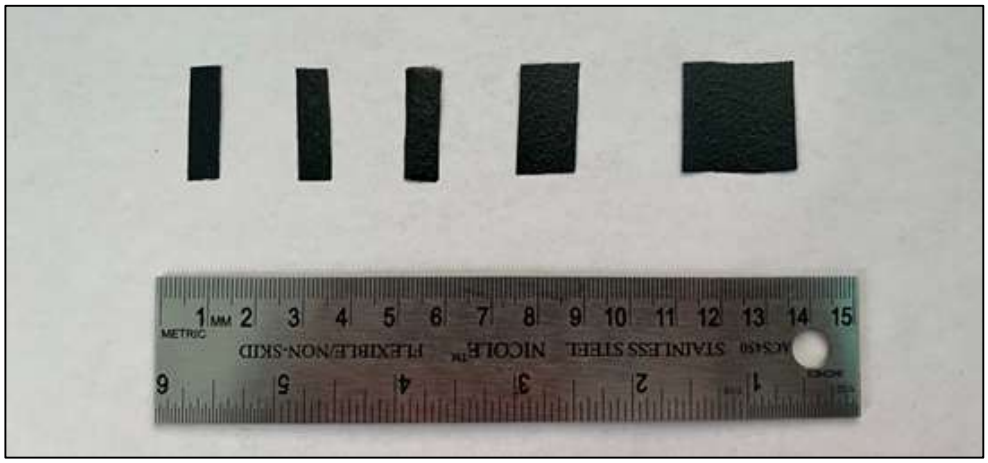

(a)

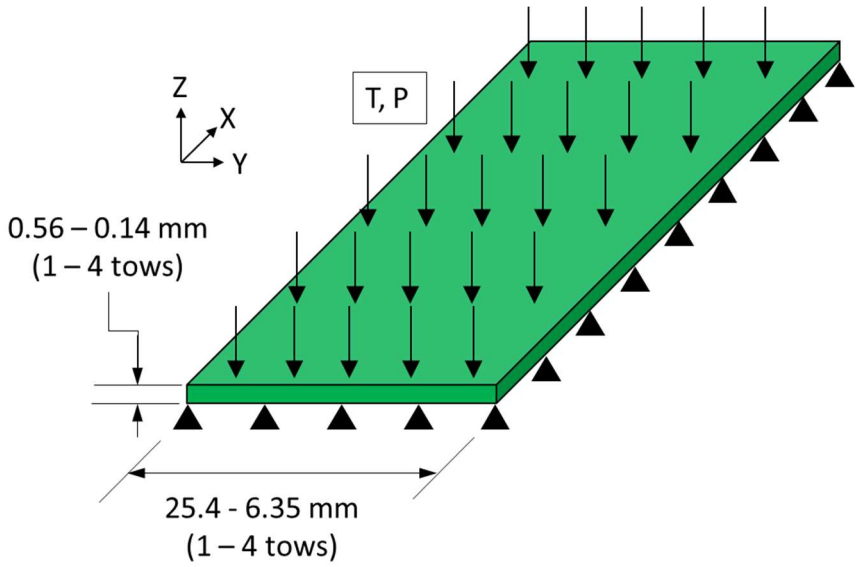

(b)

Figure 25. (a) The fully cured samples of the unidirectional experiments and the aspect ratio in order from left to right and labeled with the aspect ratio (ξ): one ply thick (ξ =1.0), two ply thick (ξ =0.5), four ply thick (ξ =0.25), two ply wide (ξ =2.0), and four ply thick (ξ =4.0) (b) Schematics of the unidirectional FEA models, where it was varied by the same aspect ratios

3.3.2 Fabrication of an embedded fiber tow gap

A cross-ply laminate configuration incorporating an embedded tow gap was fabricated to investigate compaction behaviors specifically around the area of the tow gap. The stacking sequence employed was [0°/90°/0°], with a centrally positioned 90° tow gap oriented along the y-axis (Figure 26). The sample width consisted of four layers of 0° fiber tows and two layers of 90° fiber tows. Prior to curing, the dimensions of the specimen were 25.15 x 25.15 x 0.40 mm. During layup, a hand roller was used to apply a uniform contact force to ensure proper consolidation. Upon deposition of the top 0° layers, no additional spreading of fibers was observed, and the 0° tows settled into the central region of the tow gap. Subsequently, the sample underwent curing using a standardized cycle followed by post-curing at 180°C for two hours.

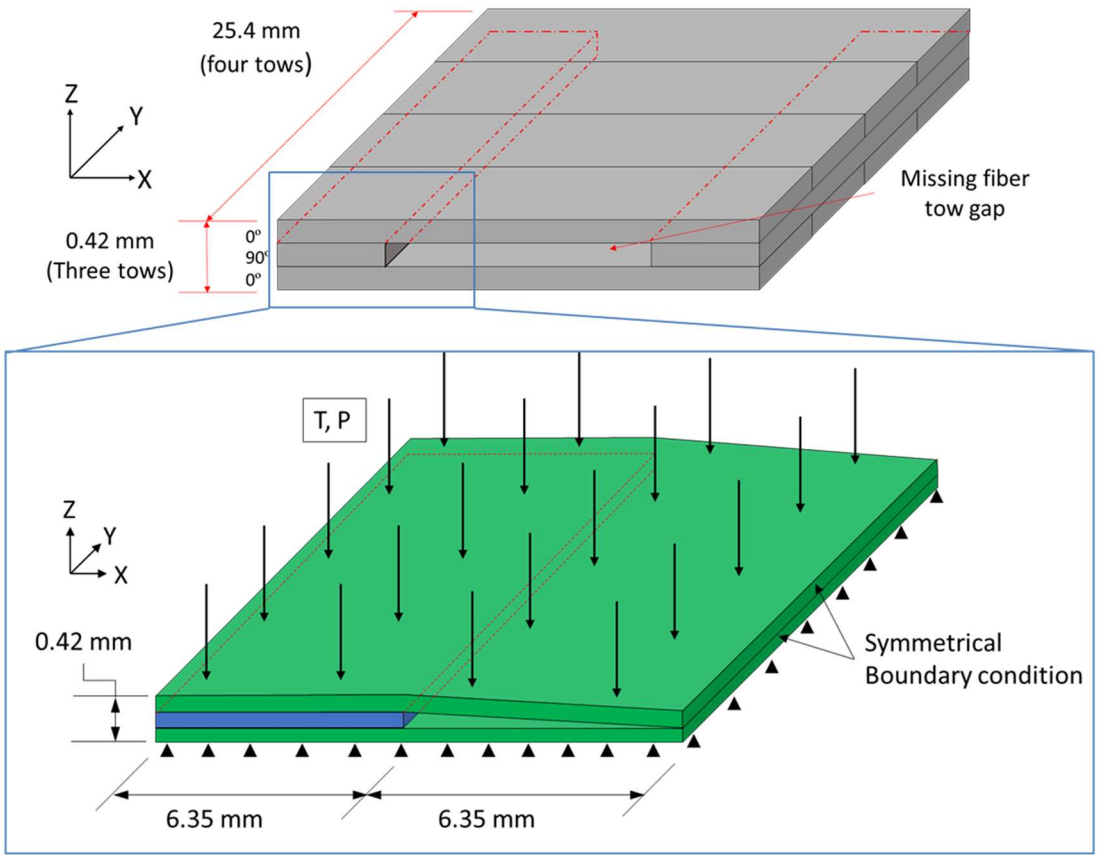

Figure 26. Schematics of the manufactured fiber tow gap dimensions and stacking sequence. The dashed line indicates the 90º ply through in the laminate.

To examine the cross-sectional morphology of the fiber tow gap, two methods were utilized to capture the images of the tow. One method positions the tow using two clamps and placed near a microscope. Composite tow gap specimens were also incased resin which was subsequently polished. An initial rough polishing was used to flatten the surface to ensure contact for the finer grits. After the initial rough polishing, the following grit was used on the composite in order: 320, 400, 600 grit. Finally, each sample was polished using cloth infused with diamond paste of 6 µm, and 1 µm grit. The sample was polished with each grit for 30 minutes each. Analysis of the polished samples was taken in the x-z plane, where x is the fiber direction, was performed using a Leica

DM6 upright microscope to evaluate various ply characteristics as shown in Figure 27. These included measurement of fiber angles within the top 0° tow, dimensions and shape of resin-rich regions, and variations in ply thickness within the bottom 0° tow.

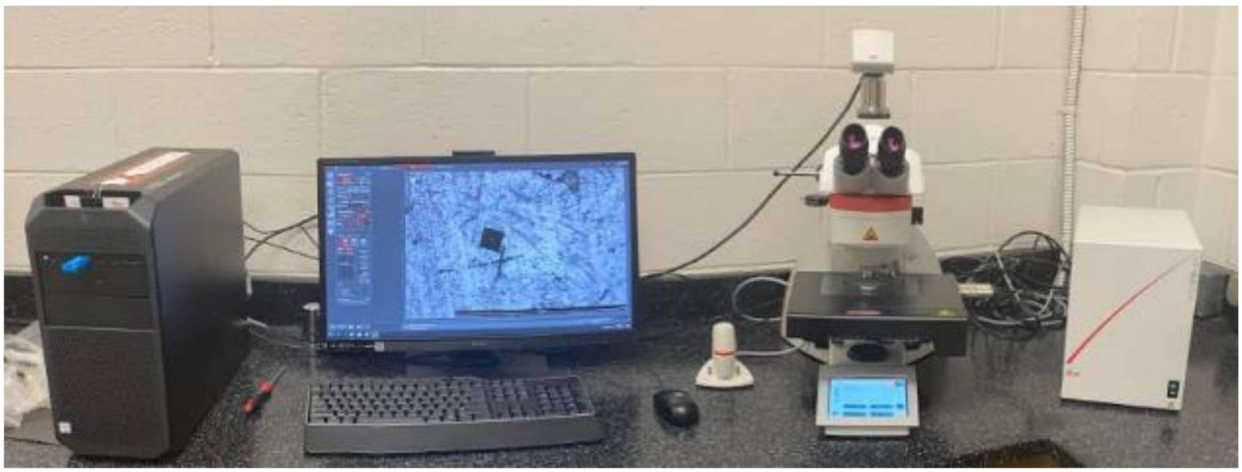

Figure 27. The Leica DM6 microscope used to observe the results of the curing of the composite samples.

3.3.3 Multiphysics approach for resin bleed out simulation.

A comprehensive computational process modeling approach was developed to establish the influence of compaction and resin flow on the morphological irregularities of composite structures. The interconnected nature of the manufacturing cure and compaction processes was examined through a unified modeling strategy utilizing physics-based simulations. Specifically, a compounded multivariable model, comprising a chemo-rheological model and a flow-compaction model, as illustrated in Fig. 28, was employed. The model loops between the chemo-rheological model which updates the material response in the flow-compaction model until the allotted time is reached for the simulation. The results are the defect morphology based on the deposition induced feature. This model analyzed various rheological and physical properties, including the degree of cure, viscosity, fiber volume fraction, and fiber orientation.

The tow gap configuration was used for understanding the effect of resin bleed-out on the cured morphology around the gap region. For the fiber tow gap sample, the FEA model used the same stacking sequence and geometry as the experimentally manufactured composite (Figure 28). To incorporate the initial sinking of the top 0º ply, created by manually applied roller during the layup, the initial slope was incorporated by connecting the bottom and top 0º plies at the middle of the gap. Symmetrical boundary conditions were used on the x-z plane of the 0º plies towards the gap and one side towards of the y-z-Z plane to reduce processing time. To simulate the tool, the bottom of the laminate model was constrained in the z-direction.

The model consisted of 2088 C3D8RT elements to capture the non-linear deformation with hourglass control to maintain excessive deformation on the model. Frictionless contact between the layers of 0° and 90° plies was used. Each ply had a nominal 0.14 mm in thickness. The 0º and 90º plies had two and five elements through the thickness, respectively, to better capture the deformation mechanisms near the tow gap region. Both sets of models, unidirectional and tow gap simulations, used a density for the homogenized composite of 1590 kg/m3 with a mass scaling of 10 to reduce the amount of time to complete the FEA simulations. No significant rise in kinetic energy was found with the addition of the mass scaling. The material properties for both the IM7 carbon fibers and the 8552 resin were derived from literature and are utilized in the subroutines as shown in Appendix A [19], [31], [32]. Since the plies the laminate was notably thin, the heat was applied via a boundary condition for both the unidirectional and the fiber tow gap model. To reduce the computation time, the fiber tow gap featured a symmetrical boundary condition on the Z-X plane, towards the gap in the laminate and the Z-Y plane, towards the negative X direction. Geometric non-linearity was activated for both models to accommodate the large deformations during the compaction.

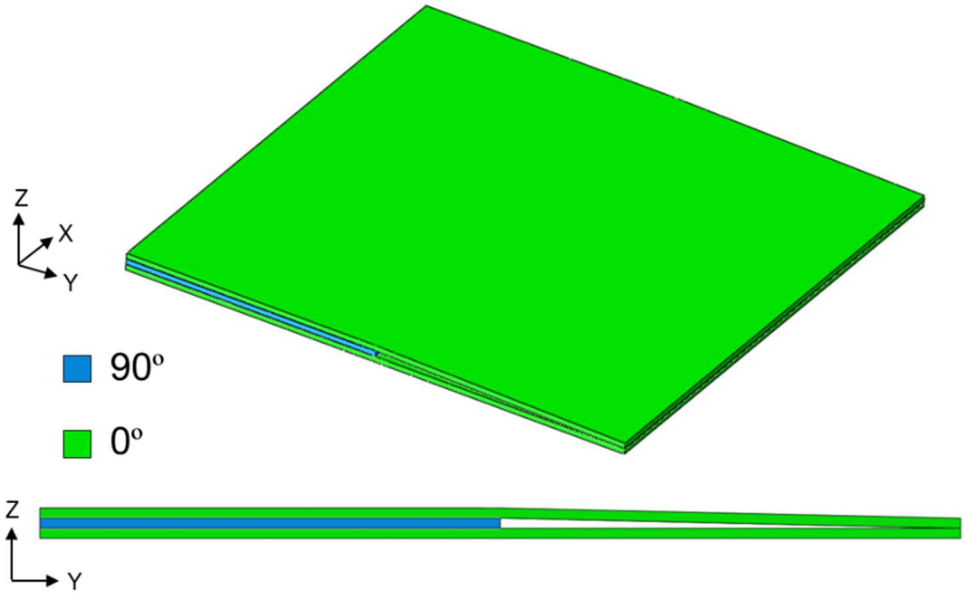

Figure 28. The FEA model of the composite with a single fiber tow gap

3.3.4 Initial Degree of cure measurements

The initial degree of cure of the composite samples was measured using digital scanning calorimetry (DSC). These tests manage to capture the chemical properties of the material such as in the curing of resin. The machine used was a DSC-60A (Figure 29a) with 5.8 mm aluminum pans. The testing apparatus was first calibrated using a standard dynamic indium and zinc tests where the material was heated to until an exothermic reaction occurs. The energy was measured and compared to the expected output based as a function of its mass. The machine was automatically calibrated from the results of the melting temperature and the enthalpy of the results. After the calibration, a dynamic test DSC was conducted on the uncured prepreg. The material was prepped where a strip of 5mm x 5mm strip of the prepreg was cut and weighed before it was sealed in an aluminum pan. The specimen was heated to 110 ºC and was held for the initial manufacturer recommended cure cycle. The exothermic reaction was quantified by taking the integral of the area

and compared the result to the total heat of reaction of 474.9 kJ/kg (Figure 29b). Finally, the initial degree of cure of the material used was determined to be at 14.5%.

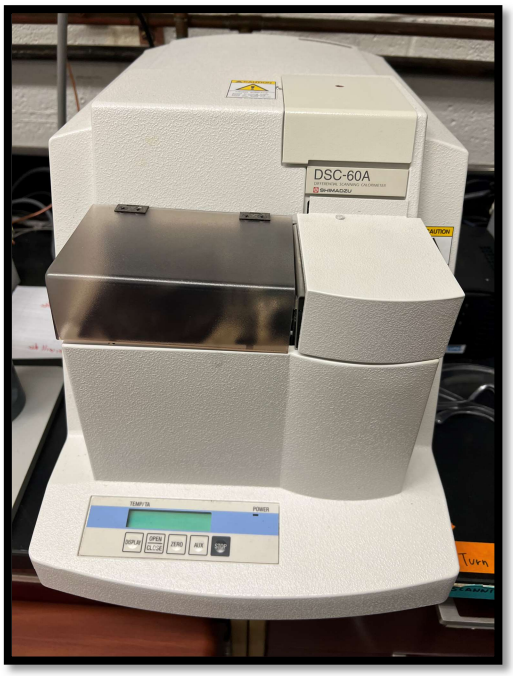

(a)

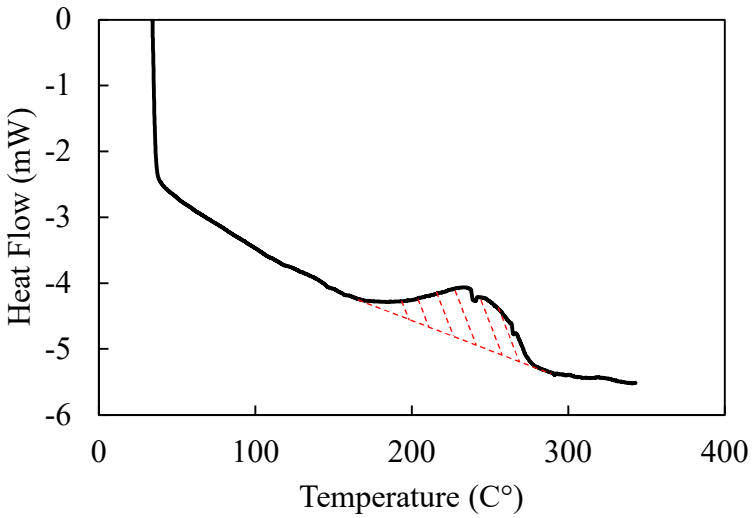

(b)

Figure 29. a) The Shimadzu DSC-60A used for the DSC test to characterize the chemo-rheology of the resin. b) The results of the dynamic test performed

As the resin cures, the phase changes accordingly and affects the viscosity of the resin. The function for the viscosity uses the degree of cure and temperature as shown in Eq 55.

$$\mu = \mu_{\infty} e^{k_i \alpha} e^{\frac{U}{RT}} \tag{55}$$

where $\mu_{\infty} = 83 * 10^{-8}\ MPa \cdot s$ is a viscosity constant, and $U = 49100$ kJ is the activation energy of the viscosity, $k_1 = 25.49 \frac{kJ}{mol}$ and $k_2 = -1.32 \frac{kJ}{mol}$ are temperature independent constants determined through experimental data [41]. The applied temperature, and the evolution of the degree of cure, and the viscosity is shown in Figure 30. The degree of cure can be seen to go past 50% cure at the start of the hold stage, which is when the 8552 resin begins to gel. Furthermore, the viscosity increases quickly due to the gelation of the resin. This shows that it can be assumed that the rheological phenomenon happens during the first 60 minutes of the cure cycle for the composites used in the experiments.

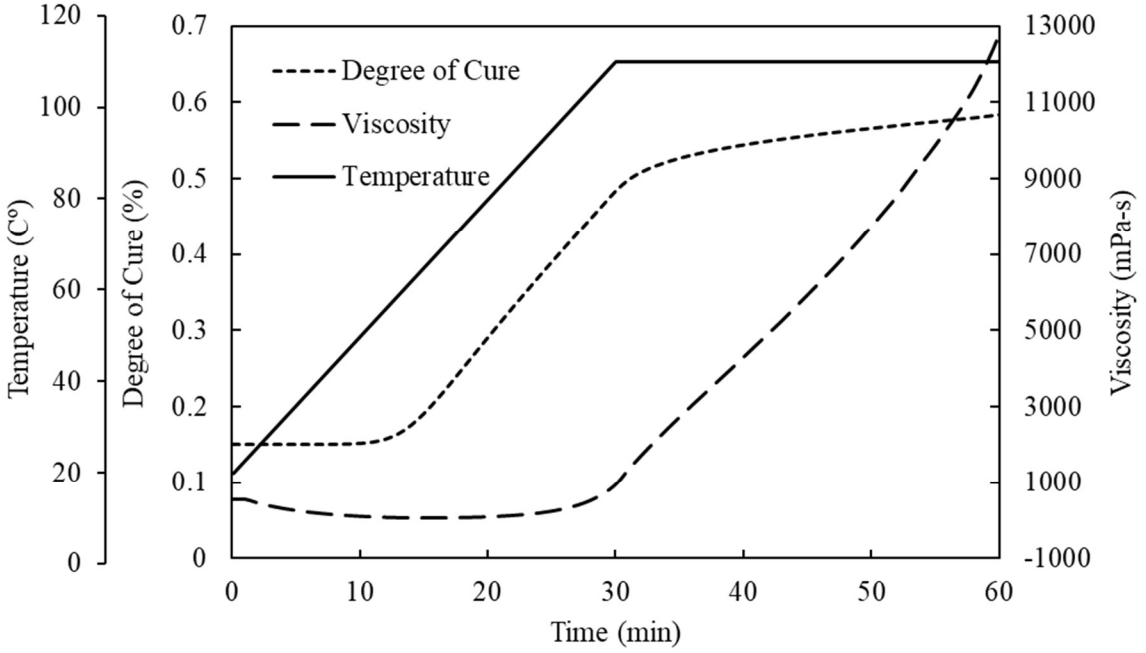

Figure 30. The applied temperature and the evolution of the degree of cure and viscosity using the thermo-rheological model

3.4 Resin Bleed out in laminates with multiple gaps

The work continues from the single tow gap model, with a significantly more complex laminate. With the addition of more gaps, the deformation becomes more irregular during the curing process. The ability for AFP devices to precisely place, cut and restart tows, means that the tow placement and the angle becomes a part of the design space. Furthermore, gaps and overlaps, although seen to be defects, can be tailored in order to reduce the influence of defects on laminate. For example, staggering of gaps through the thickness of a laminate avoids the concentration of resin rich regions and effectively increasing the load transfer between the plies [104]. However, observing the resultant morphology due to these multiple defects is necessary for a more accurate prediction of the strength of the composite. This work explores the non-linear deformation of a

laminate with staggered gaps and utilizes the methodology established with that single gap model. With the addition of more gaps, the deformation becomes more irregular during the curing process. This work was first presented at AIAA SciTech Forum 2023, which mainly shows the similarity between the defects in the experimental micrograph and the model.

3.4.1 Sample Fabrication

A sample was manufactured under the same conditions for the models as the laminate with a single gap. Unlike the single gap experiment, there were five tows for each layer which was 31.75 mm for each in-plane side. For the study, a structure with multiple staggered defects was manufactured to investigate the effects of multiple gaps through the thickness. The laminate consists of seven layers (0.98 mm thick) in a cross-ply stacking sequence, [0º/90º/0º/90º/0º/90º/0º], with fiber tows gaps distributed in the 90º layers. Each gap was 6.57 mm wide, and was located at the second, fourth, sixth and eighth layers. A single fiber tow gap was centrally located at the fourth layer and sixth layer. Two gaps each were placed in the second, and eighth layer, with one gap located beside on each side of the center ply (Figure 31). All fiber tow gaps were oriented in the Y-direction. The sample cure cycle used on the sample with a single fiber tow gap was used on multiple gap sample. The same material, IM7-8552, was used in the manufacturing of the sample with multiple tow gaps.

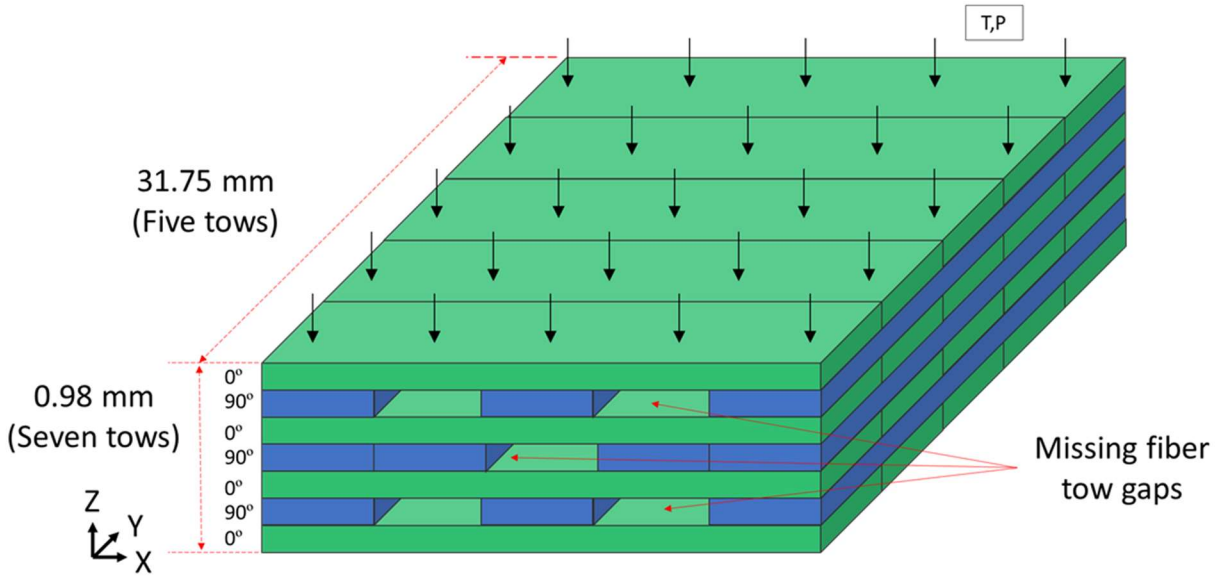

Figure 31. Schematic of the staggered defect model

3.4.2 Multiphysics model with multiple gaps

The model initially developed for analyzing a laminate with a single gap can be extended to accommodate configurations involving multiple embedded gaps. This allows for a more comprehensive understanding of the deformation in more complex laminate systems. Similarly to the model with a single fiber tow gap, a symmetrical FEA model was constructed to predict the deformation of the laminate (Figure 32). The multiple gaps were divided into four sections each where the pressure was activated at 5,10, 15 and 25 minutes into the cure cycle. Since the resin was an incompressible liquid as the composite cured, the resin bleeding into the gaps were simultaneously pushed towards the edge of the 90°. Once activated, the pressure remained constant for 25 minutes before rapidly decaying. This pressure was applied via a distributed load in the internal surface of the fiber tow gaps in the staggered model. Two models were made with the staggered defect configuration, with and without the internal void pressure. This pressure was

assumed to have the same magnitude as the applied pressure of 0.551 MPa (80 psi). The same physics were transferred from the single gap model into the model with multiple gaps. This includes the chemo-rheology model, and the tow compaction model. Furthermore, the resin bleed out found in the previous model was applied to the multiple tow gaps.

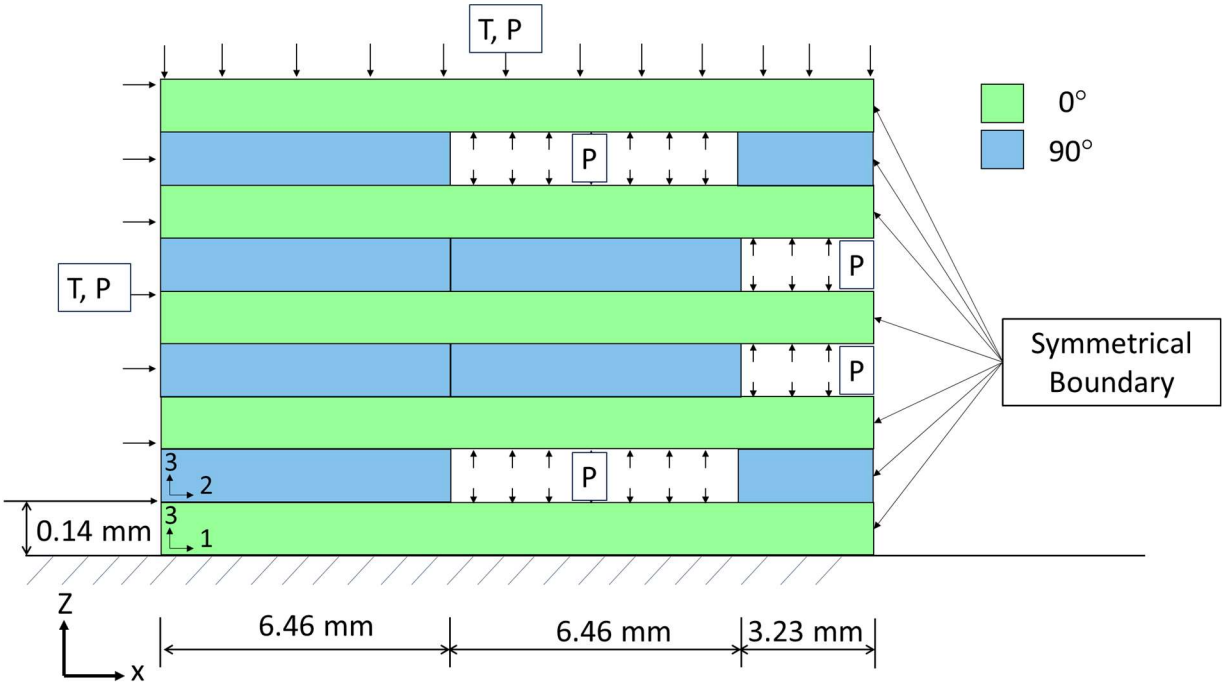

Figure 32. A schematic of a composite with a single fiber tow gap. The gap fills with resin over time creating a pressure in the inside that supports the applied pressure from the autoclave.

4 Results

4.1 Non-Crimp Fabric Compaction

4.1.1 Single element simulation results for a non-crimp fabric

The results of the single element tests exhibited a robust correlation between the numerical simulations and the experimental data in the stress vs. strain plots (Figure 33). The stress shows an exponential increase with respect to strain similarly found in the compaction experiments. While some deviations were observed at a strain rate of 5 mm/min, the correlation remained strong at strain rates of 1 mm/min and 2 mm/min between the experimental and numerical results. This finding suggests that the model is proficient in accurately simulating both large strain and the time-dependent components of compaction. Consequently, the model is suitable for application in more complex simulations involving multiple non-crimp fabric layers.

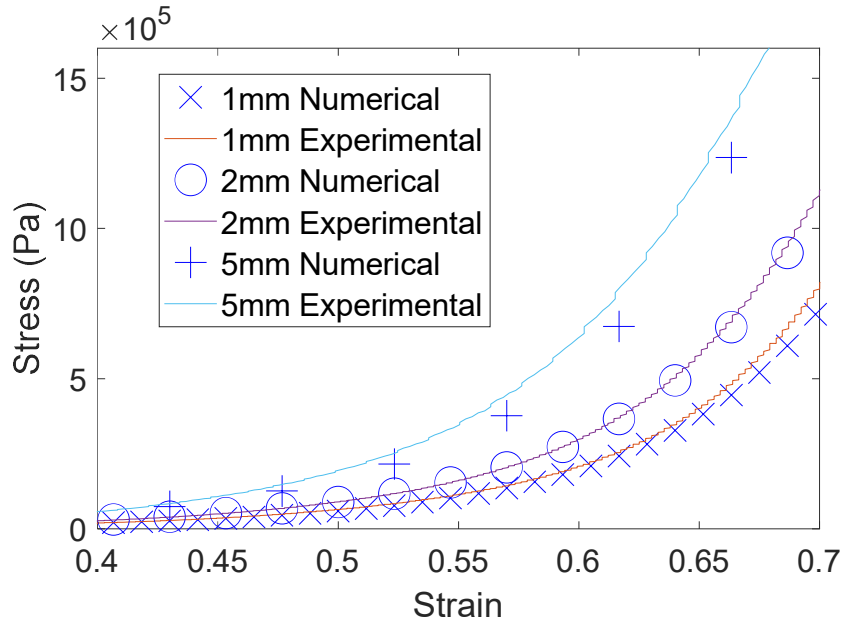

Figure 33. The single element results of the non-crimp fabric FEA models

4.1.2 Multi-layer simulation results for a non-crimp fabric

A critical factor in resin infusion is the permeability through the fibers, which is influenced by the fiber volume fraction distribution. In the reference case, the model was subjected to a displacement of 2 mm at a rate of 2 mm/min, as illustrated in Figure 34. The fiber volume fraction was highest at the top ply and progressively decreased towards the bottom and the fabric edges. Voids were observed forming and shearing between the non-crimp fabric layers, with wrinkling increasing from the fabric center towards the edges. Many voids formed at the bottom of the fabric. This variation indicates that the non-linear morphology and distribution of the fiber volume fraction varied throughout the fabric, despite the load being concentrated at the center. These variations result in resin-rich regions, which effectively diminish the mechanical properties of the composite. Therefore, the implementation of a digital twin was necessary to accurately predict these outcomes.

To compare the models at different strain rates, the fiber volume fraction distribution was examined at a displacement of 1 mm (Figure 35). At this displacement, the fiber volume fraction profile varied across the different strain rates. A higher fiber volume fraction pocket was observed at the bottom of the top ply for the 5 mm/min strain rate. The maximum fiber volume fraction recorded was 49.16% for the 5 mm/min rate, located at the roller edges. In contrast, the 1 mm/min experimental data showed a fiber volume fraction of 47.31%. For the 2 mm/min rate, the models indicated a maximum fiber volume fraction of 48.81%, concentrated at the top of the ply. The maximum fiber volume fraction consistently occurred at the roller edges, where shearing between the layers was prominent. The distinct profiles for each compaction speed demonstrate a clear relationship between fiber volume fraction distribution and crosshead velocity.

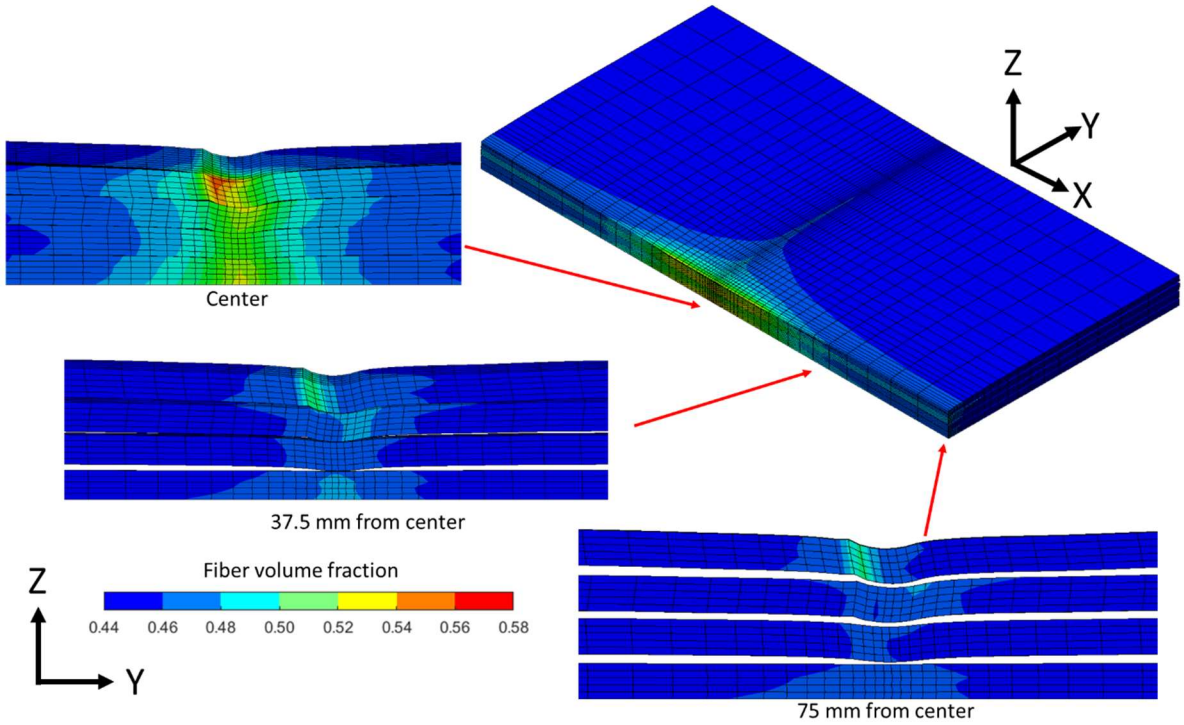

Figure 34. The fiber volume fraction prediction for the 2 mm/min compaction speed model with at 2 mm displacement where it shows various locations in the model in the Z-Y plane.

Upon examination of the cross-sectional profiles in the X-Z plane, noticeable undulations were observed between adjacent layers, indicating a displacement of 1 mm (Figure 36). Concurrently, the highest fiber volume fraction coincided with the most rapid strain rate. Despite variations in thickness distribution, the average strains at the roller's base were consistently recorded as 43.76%, 44.08%, and 43.52% for compaction speeds of 1 mm/min, 2 mm/min, and 5 mm/min, respectively. Notably, out-of-plane undulations were insignificant within this range. However, the cross-sections of the 1 mm/min model exhibited narrower gaps near the roller, whereas those of the 5 mm/min model showed wider gaps extending towards the x-direction. The 2 mm/min model displayed the least separation between layers, manifesting a gradual curvature in the laminate layer. Both cross-sectional analyses underscored the significant influence of

compaction speed on the fiber volume fraction of non-crimp fabric, emphasizing its criticality in the manufacturing process.

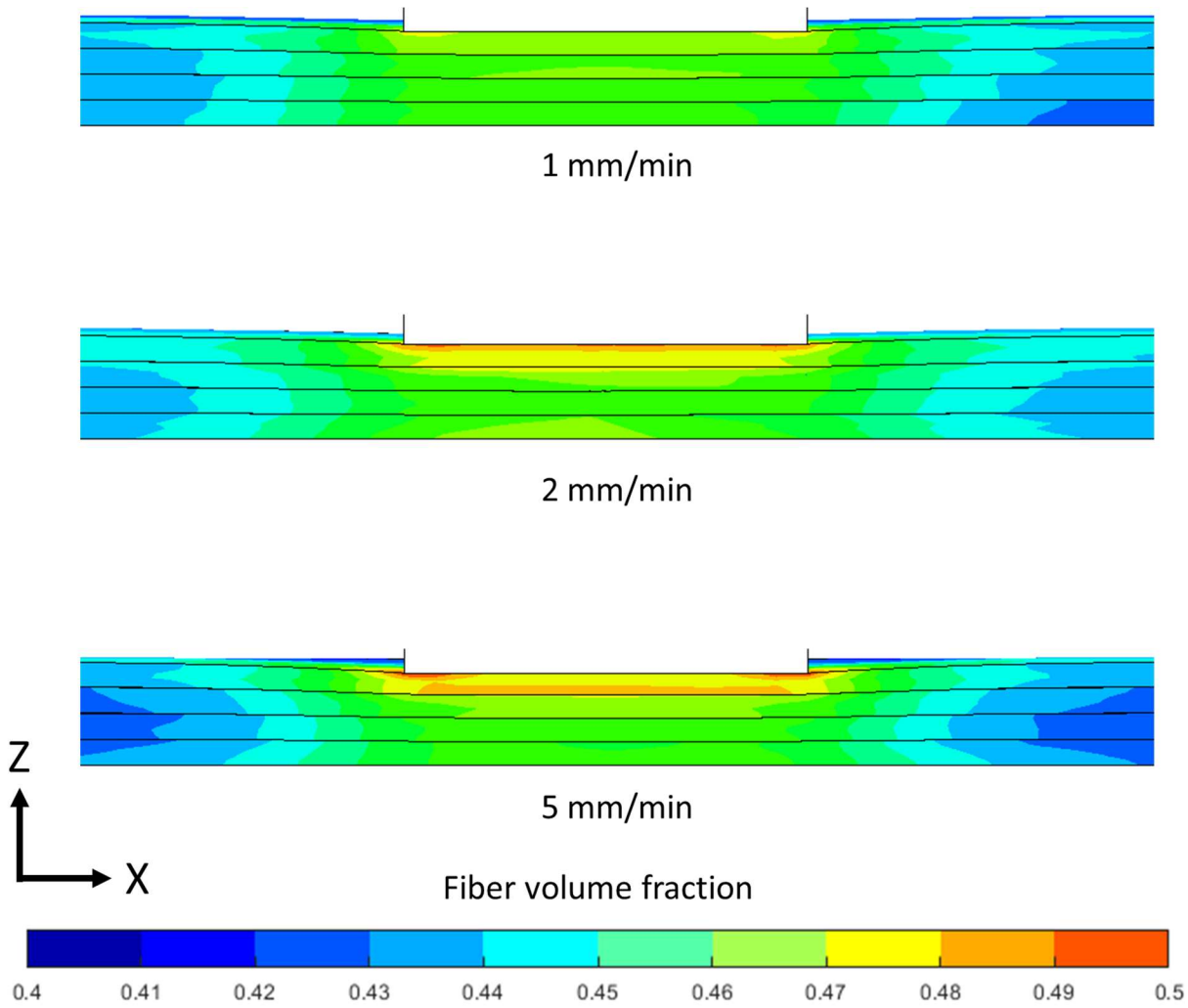

Figure 35. The fiber volume fraction distribution of the non-crimp fabric simulation with a velocity of 1 mm/min, 2 mm/min, and 5 mm/min at 1 mm displacement.

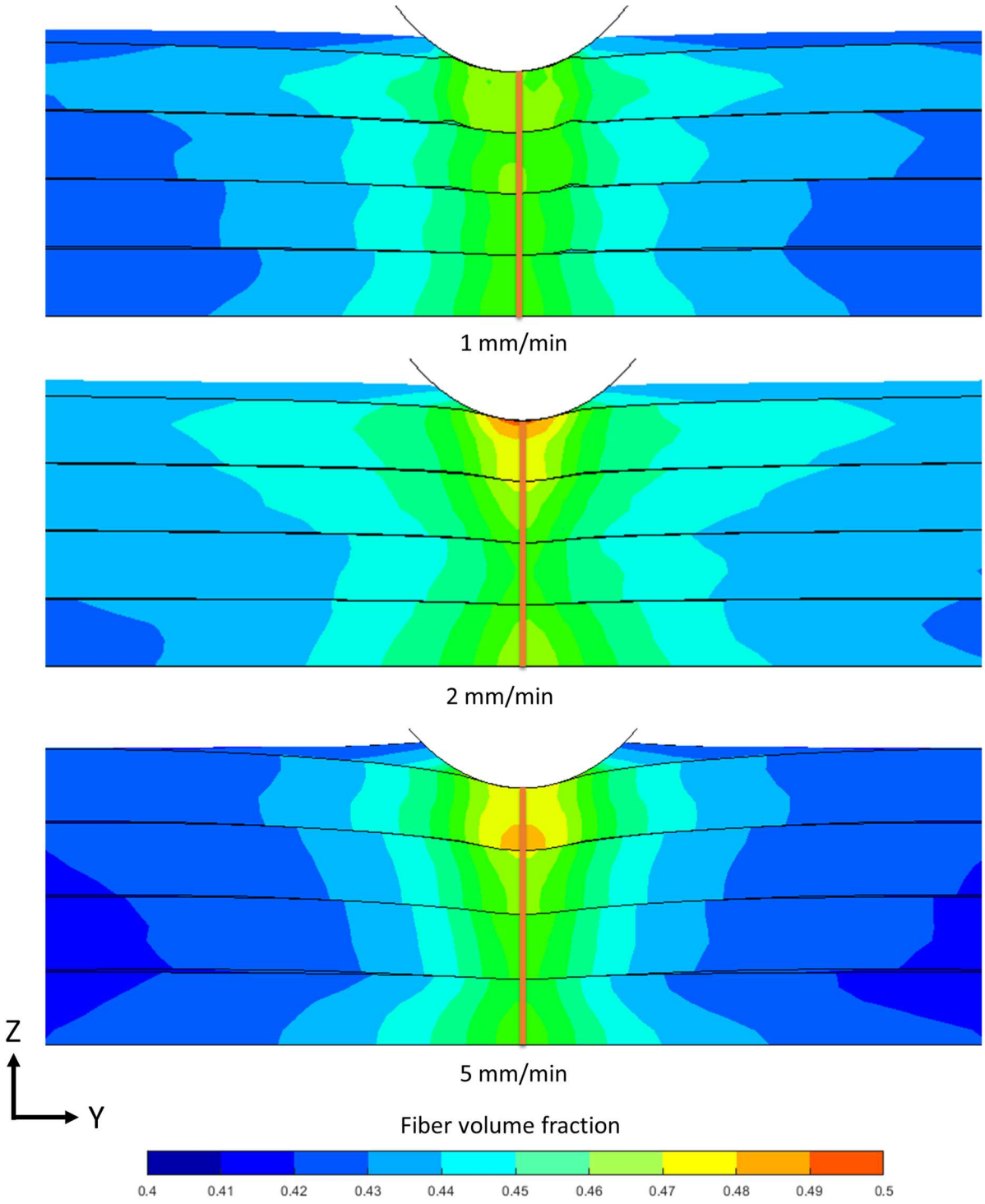

Figure 36. The Z-X plane view of the model at 1 mm for all models, which depicts the fiber volume fraction in the non-crimp fabric and the nodes used to measure the average strain.

4.2 Tow spreading analysis of roller compaction

4.2.1 Robotic arm feedback data

The robotic arm provided a small-scale AFP testing environment, with the ROS capturing the force and roller speed. Initially, the force exhibit fluctuations but stabilizes towards the later part of the tow (Figure 37a). Roller speed remains consistent across various thicknesses and throughout the tow (Figure 37b) and a negligible error of 0.40% error in the input velocity (50 mm/s) indicates the speed is unaffected by the substrate thickness. However, the recorded force shows a more significant variation. The average error for the 10 N, 30 N and 50 N were 24.10%, 7.52% and 4.89% with respect to the composite substrate thickness, respectively. The force may contribute to the tow thickness, which leads to the measurement of tow spreading being averaged along the tow length. Addressing the variation in tow thickness due to force and speed is crucial for enhancing the robotic AFP system in future developments.

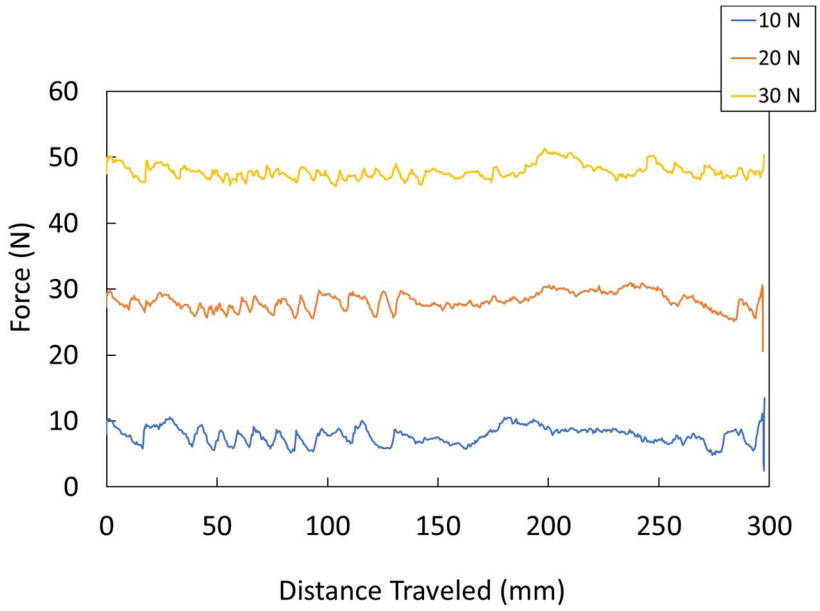

(a)

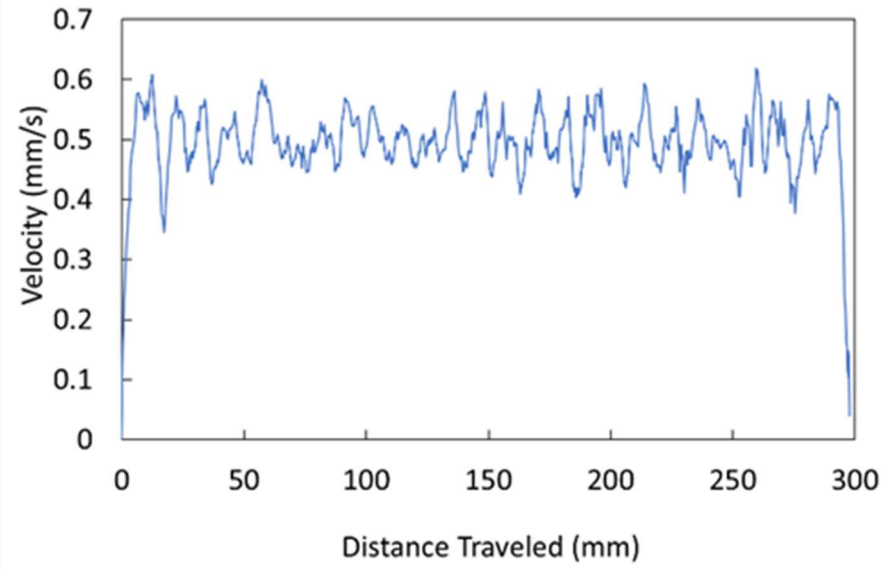

(b)

Figure 37. The recorded a) force and b) speed for the experiment with one layer substrate of composite substrate

4.2.2 Transient heat transfer during roller compaction

The thermocouples were placed adjacent to the composite tow to measure the substrate temperature without interfering with the roller or affecting tow deformation. Figure 38 presents temperature measurements across the length of the tow and the distance from the initial roller position for thermocouples TC-1 through TC-7. The first thermocouple (TC-1) registered a temperature of 26.4ºC compared to the 60ºC measured on the surface of the roller. Subsequent smaller temperature spikes of approximately 25.4ºC were observed as the roller passed near the thermocouples, followed by a gradual decrease to the ambient temperature of 22ºC. The model's peaks show a more consistent 26ºC before dropping to the sink temperature of 20ºC. The comparison between experimental and FEA temperature peaks suggests that the thermal profile is

accurately captured, thereby enabling the analysis of the hyper-viscoelastic deformation of the prepreg tow during roller compaction.

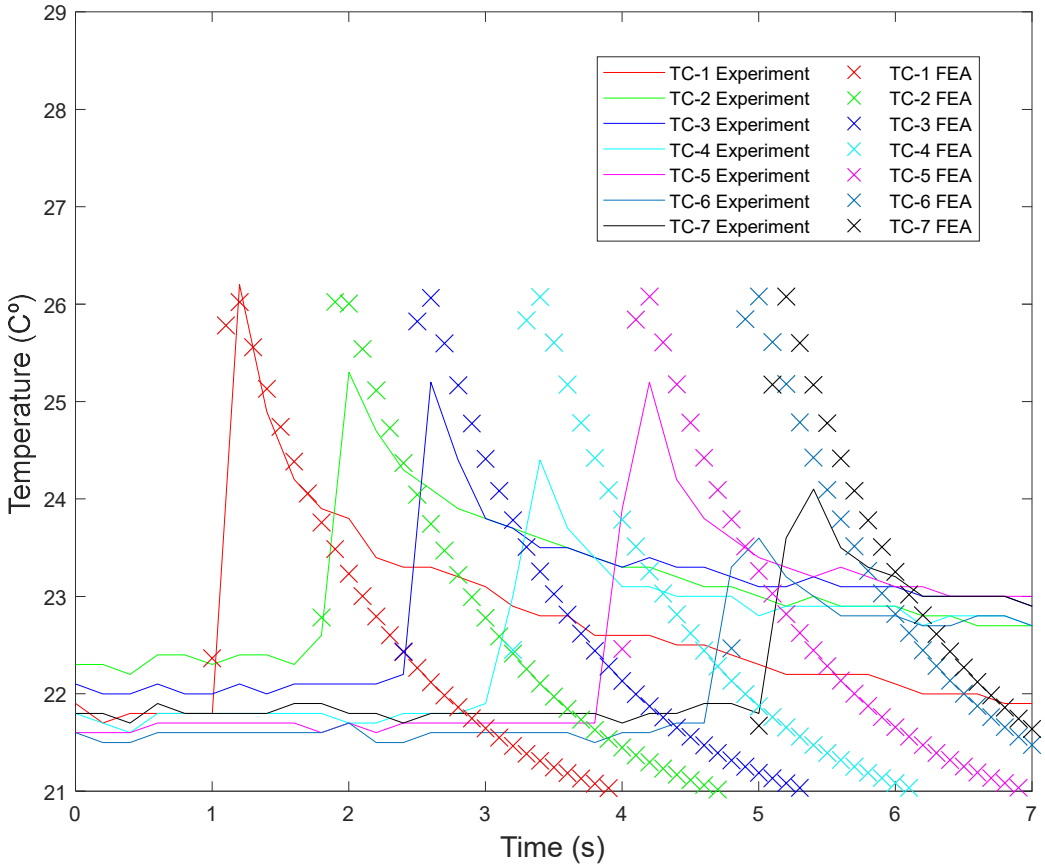

Figure 38. The temperature recorded by the thermocouples on the substrate as the roller passes. The spike shows the location of the roller. The distance is measured from where the initial point the roller contacts the ply.

4.2.3 The effect of prepreg laminate thickness on tow spreading behavior

To understand the effect of the prepreg laminate thickness on the heat dissipation, Fig. 36a illustrates the surface temperature of the prepreg tow as the roller traverses. In the initial compaction of one ply with a 10N load (1s), the composite tow's surface temperature reaches a maximum of 52ºC, while the surrounding composite substrate peaks at 27ºC, measured 6 mm

away from the tow. As the roller moves across the tow's surface, the temperature rapidly decreases to 20ºC, as observed in the composite laminate model with a single layer (Figure 39a). In the case of a ten-ply thick prepreg laminate, roller simulation with a 10 N load produced an elevated temperature distribution throughout the duration of the simulation, demonstrated by a larger area exhibiting a temperature of 39 ºC on the surface of the substrate (Figure 39b). This heat retention can be attributed to the low thermal conductivity of the thermoset and the increased distance between the heat source and the thermally conductive aluminum tool. The gradient of temperature of the tow can be seen in Fig. 39c, where the gradient of temperature is shown at 1 second after the roller passes. The surface temperature was seen to have a difference of 6 ºC due to the lower conductivity of the composite substrate. This shows that the thicker substrates result in a more prolonged state of decreased viscosity.

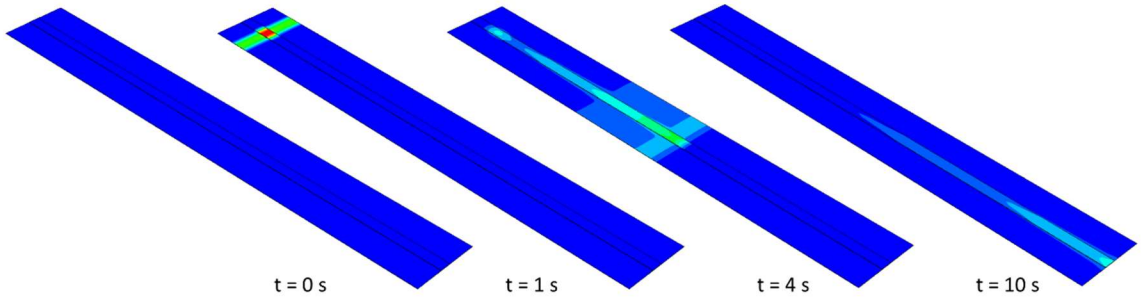

1 ply prepreg laminate

(a)

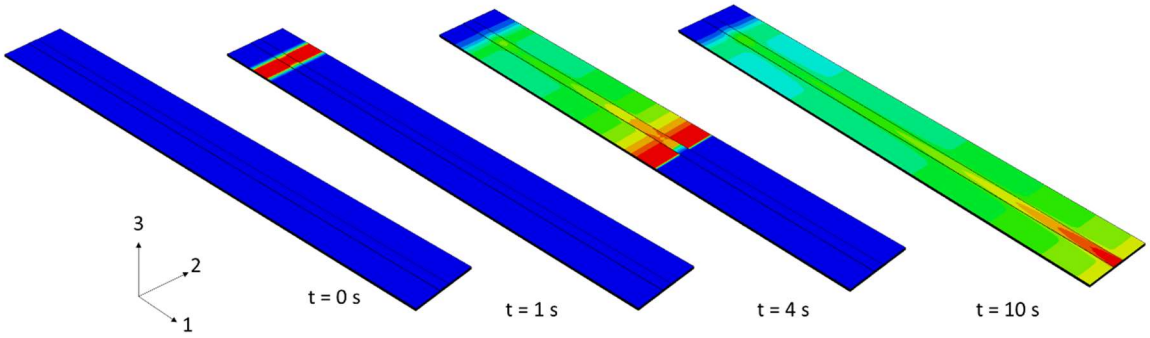

10 ply prepreg laminate

(b)

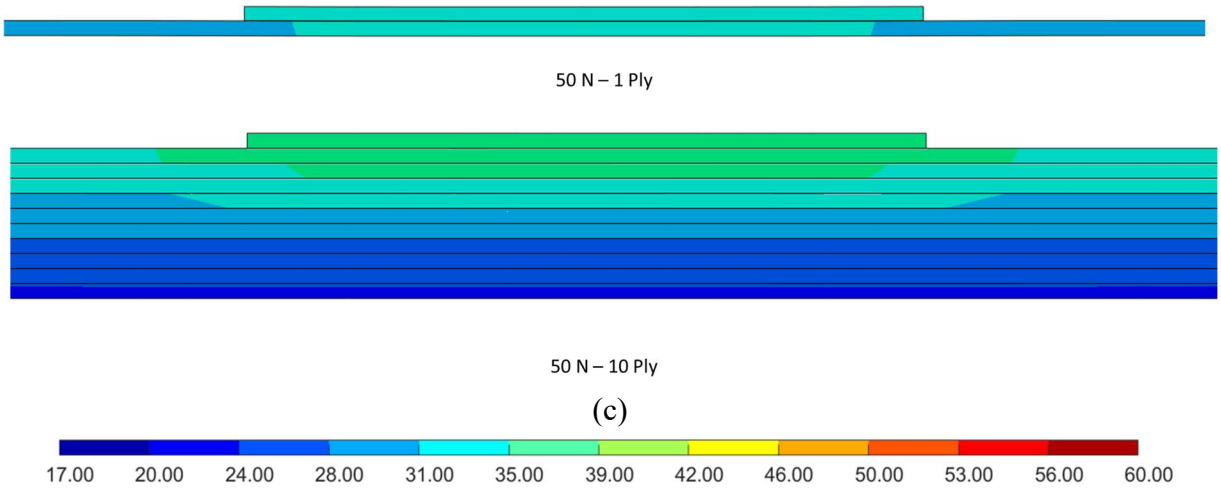

Figure 39. The effect of prepreg laminate thickness on the heat dissipation during roller deposition for 1 ply a) and 10 ply b) thickness at 10 *N* simulation (roller was removed for better visibility) c). The cross section of the temperature in the 50 N – 1 Ply and 50 N – 10 Ply models

Figure 40 illustrates tow spreading in relation to substrate thickness and compaction force. Both experimental and modeling data reveal a rapid decrease in tow spreading as the composite prepreg thickness increases. The maximum spreading, with a transverse strain of 0.06, is observed with a single prepreg laminate layer under an applied force of 50 N. Additionally, the experimental trend indicates that increasing the number of prepreg layers from 1 to 10 results in a decrease in tow spreading from a strain of 0.015 to tow contraction at a strain of -0.005 under a 10 N force. This experiment demonstrates a correlation between substrate thickness and tow spreading behavior. The results suggest that tow spreading can compound as the composite substrate increases, potentially leading to deposition features that significantly impact the structural integrity after curing.

To observe tow spreading and compaction behavior, an FEA model was used to simulate the mechanisms of deformation during and after deposition. The modeling results showed a similar rapid decay in the transverse spreading of the tow as the substrate thickness increased. Thinner prepreg substrates resulted in tow spreading, while thicker substrates showed contraction in the composite tow (Fig. Figure **40**). For 1 ply model with a 10 N force applied, the width expands along the substrate. The model, the model with a 10 N force applied to 10 substrate layers first expands as the roller pushes into the composite tow. However, when the pressure is released from the system the tow contracts towards the center of the substrate as shown in image shown in Figure 41a. Expanding the view of the image, demonstrates the cause of this contraction. After, the pressure is released, the composite substrate also contracts as shown in Figure 41b. The strain for the tow contraction was -0.005 for the 10 ply with a 10 N force model. Although the strain is miniscule, the thicker the composite substrate, the larger this contraction effect. This behavior is attributed to elastic recovery and contact forces between the tow and the substrate [43].

The gradient in temperature as the substrate layers increase leads to changes in the hyper-viscoelasticity of the composite, which affects the elastic recovery of the substrate. This indicates that the FEA simulations were able to capture the sources of non-linear deformation occurring in the composite tow, composite substrate, and roller interaction. However, the contraction of the tow is not fully captured by the models, suggesting that further research is needed to fully simulate the elastic recovery or other mechanisms causing fiber tow contraction.

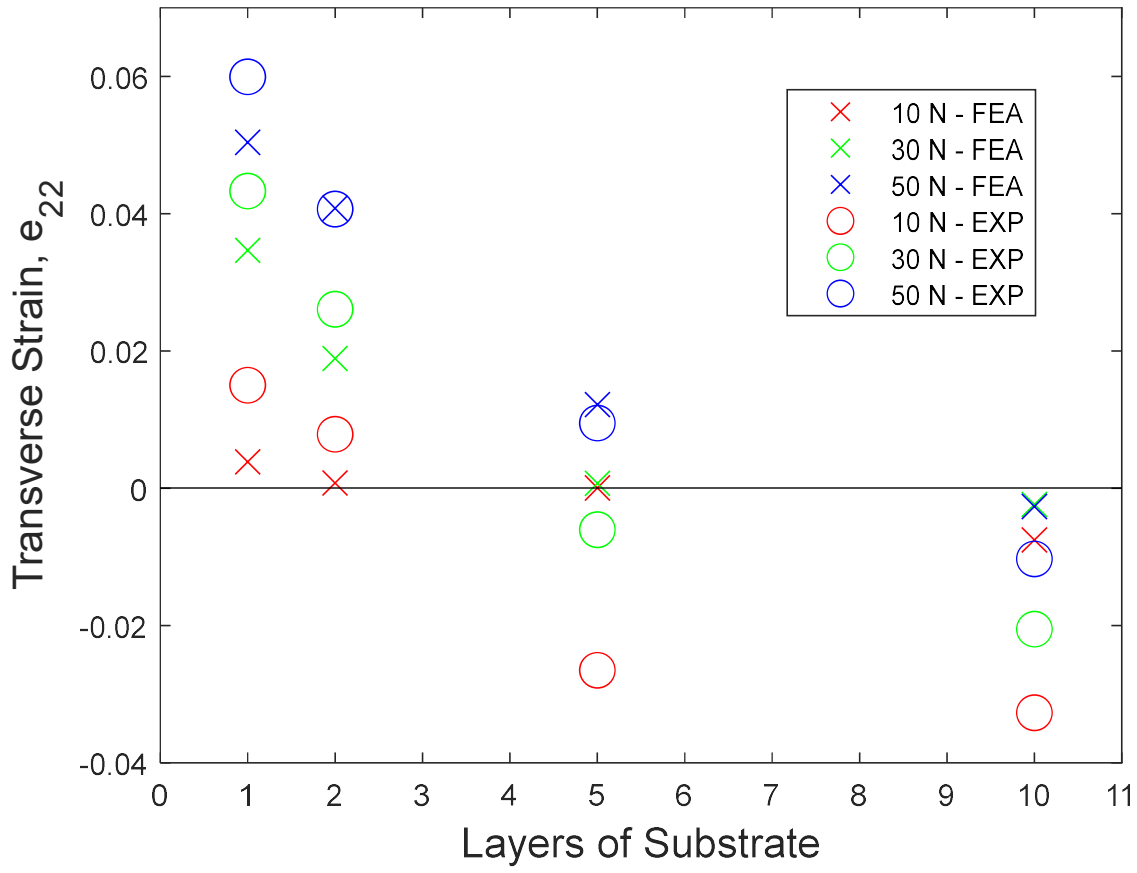

Figure 40. Plotted average values of tow spreading (strain) at different surface thicknesses for each compaction force

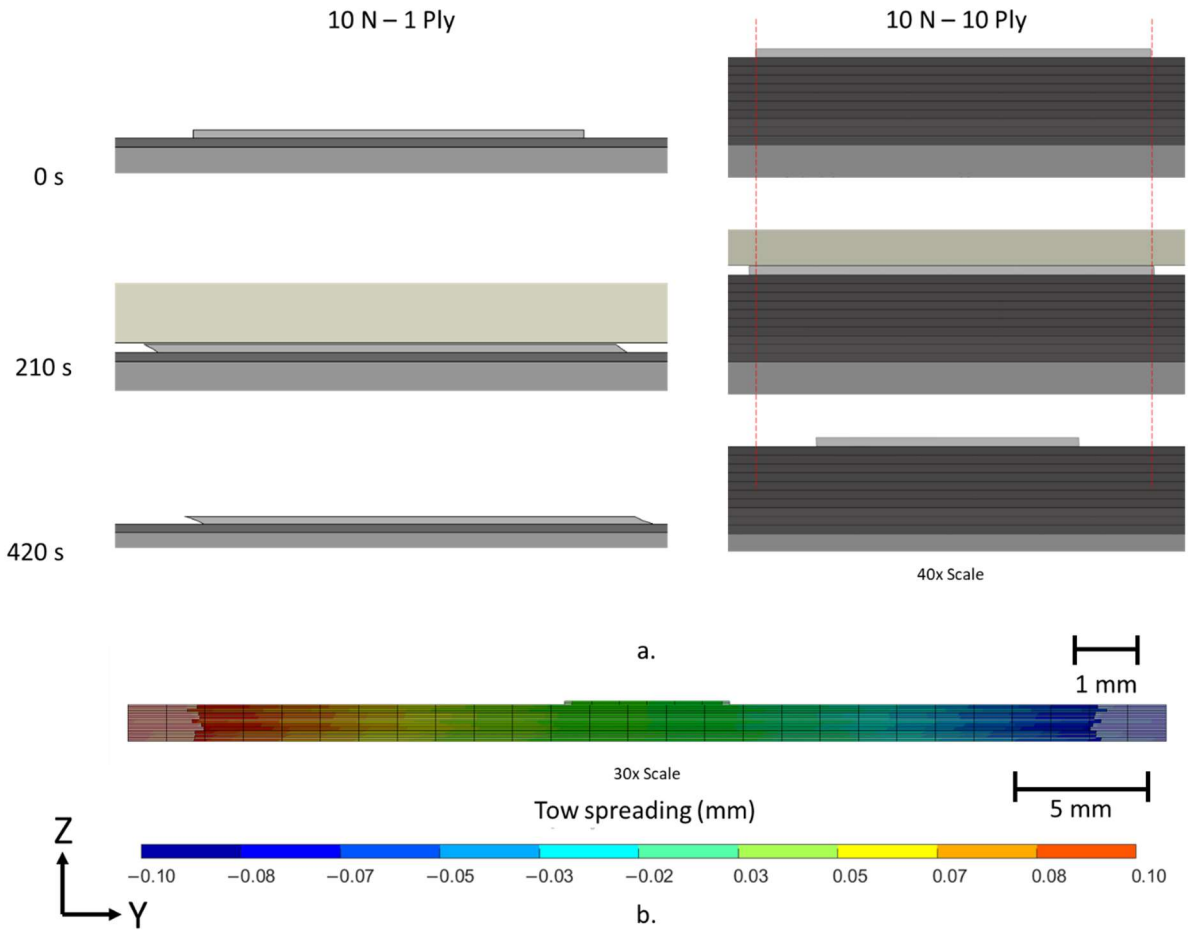

Figure 41. a.) Differences in tow spreading based on the substrate thickness. b.) A scaled image of the tow spreading of the composite ply and the substrate

4.3 Resin bleed out and deformation in a single fiber tow gap

4.3.1 Experimental quantification of resin bleed out in unidirectional prepreg tows

Six configurations, each comprising six samples of unidirectional composites, were compacted, and cured during the initial 90 minutes of the cure cycle. Six samples of each configuration were cured and consolidated in the autoclave under these parameters as shown in Figure 42. For each of the interruption times, the top film was removed, and the tow spreading was

measured. The introduction of a tow aspect ratio in the unidirectional tow was based on the number of tows across the width and through the thickness.

$$\frac{N_w}{N_T} = \xi \tag{56}$$

where Nw is the number of plies in the tow width (transverse of the fiber direction), NT is the number of tows through the thickness of the composite, and ξ is the geometric aspect ratio. For example, a sample with a thickness of four tows and a width of one tow had ξ=0.25. The experimental samples and corresponding simulations used the proposed fiber tow aspect notation.

Figure 42. A batch of unidirectional samples after curing in the autoclave.

When heat and pressure is applied to the composite, the resin liquefies and bleeds through the fiber bed. With the resin flowing out from the composite tow, the ratio of fibers to the resin also increases. The change in fiber volume fraction influences the permeability of the composite and consequently proportionally increases the apparent viscosity of the resin. Furthermore, this percolation flow or bleeding flow influences the squeezing behavior so it was quantified to

properly simulate the compaction [89]. To characterize this phenomenon, the experimental work has determined that multiple flow modes is present at the initial stages of the manufacturing process. Early in the manufacturing process, the composites are shown to have transversely spread, while resin was seen out the fiber bed. Furthermore, the resin was divided between the longitudinal and the transverse to the fiber direction (Figure 43). The portions of resin were cut from the composite and weighed. The ratio of the mass lost, and the initial weight of the composite as shown in the following equation.

$$M_r = \frac{M_L}{M_T} \tag{57}$$

where M_r is the mass loss ratio, M_L is the mass loss (transversely or longitudinally) and M_T is the total mass of the composite. When comparing the tow aspect ratio to the mass, the transverse mass flow tends to stay constant with a slight increase for higher aspect ratios. However, the longitudinal mass flow increases with increasing tow thickness or lower aspect ratios (Figure 44). While the mass lost for the transverse resin weighs more, when the length is considered, the resin flowing longitudinally across the fiber direction is responsible for a larger fraction of mass loss per unit length. This can be explained with a higher permeability through the fiber direction in comparison to the transverse resin flow [105]. Furthermore, the results show that a higher aspect ratio have a lower percentage of resin bleed out for both transversely and longitudinally. This shows that the strain and resin bleed follow a similar trend where a significant factor for both is thickness. As for lower aspect ratios, it demonstrates that a larger difference between the longitudinal and transverse.

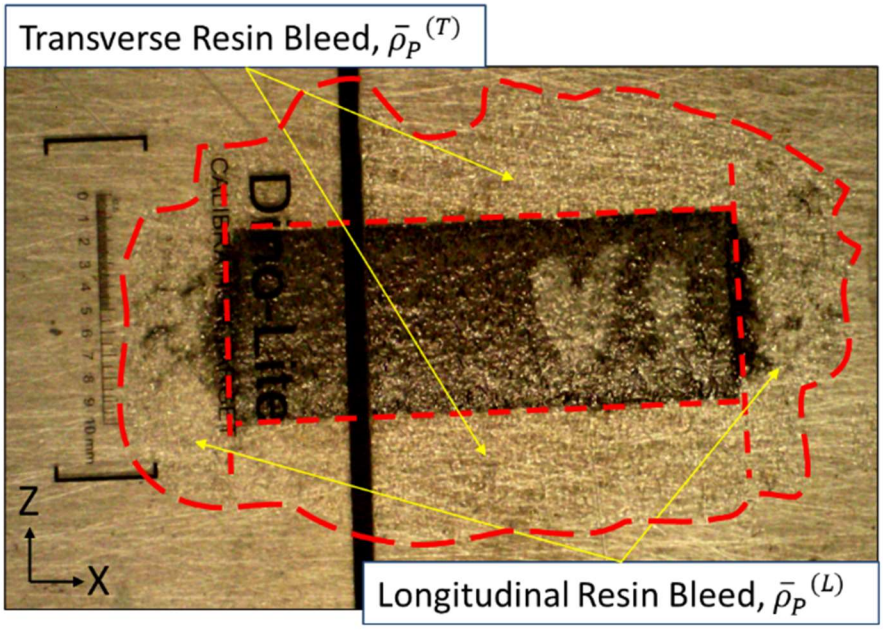

Figure 43. The area depicting the transverse and longitudinal resin bleed that was measured for one composite sample

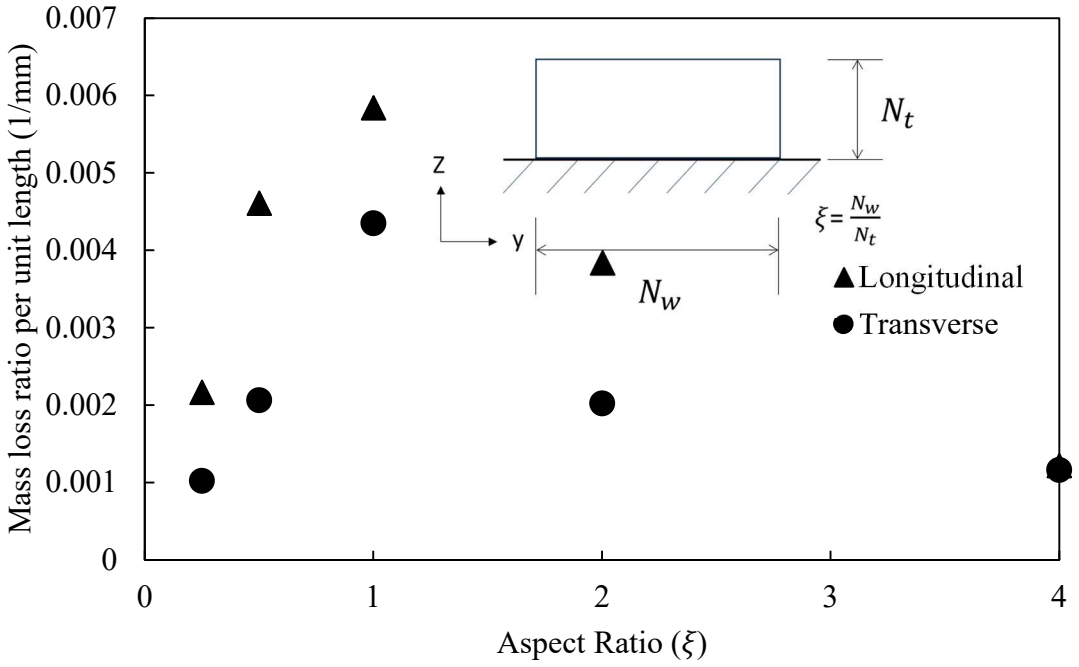

Figure 44. The mass loss fraction per unit length with respect to the aspect ratio

The average resin bleed-out mass per unit surface area, based on the initial dimensions, was measured. While the mass loss for the transverse resin was greater, considering the corresponding area revealed that resin flow longitudinally along the fiber direction accounted for a larger fraction of mass loss per surface area. Longitudinal bleed-out occurred through the surface normal to the fibers, whereas transverse flow occurred at the side of the prepreg tape, with no transverse flow observed due to the tool surface on the bottom and the release film on top. The greater resin loss in the longitudinal direction is attributable to the higher permeability along the fiber direction compared to the permeability in the transverse direction. [105]. The single tow configuration (ξ = 1.0) demonstrates that the longitudinal direction experiences a greater resin mass bleed-out per unit area, with a coefficient, $\bar{\rho}_P{}^{(L)}$= 0.400 mg/mm^2, compared to the transverse direction, which has a mass loss coefficient $\bar{\rho}_P{}^{(T)}$ =0.0198 mg/mm^2 at 90 minutes into the cure cycle. The resin area surrounding a single tow (Fig. 40) was measured transversely and longitudinally over time, serving as a basis to estimate the mass loss per unit area over time (Fig. 8. Functions representing the mass loss coefficient over time in the longitudinal $\bar{\rho}_P{}^{(L)}(t)$ (eq. 53) , and transverse, $\bar{\rho}_P{}^{(T)}(t)$, directions were based on the logistic curve functions in eq. (54). Note, that only the transverse resin bleed out was present around the surface area of the gap (Fig. 4).

$$\bar{\rho}_P{}^{(T)}(t) = \frac{A^{(T)}{}_1}{\left(1 + e^{\frac{A^{(T)}{}_2 - t}{A^{(T)}{}_3}}\right)} \tag{58}$$

$$\bar{\rho}_P{}^{(L)}(t) = \frac{A^{(L)}{}_1}{\left(1 + e^{\frac{A^{(L)}{}_2 - t}{A^{(L)}{}_3}}\right)} \tag{59}$$

where $A^{(T)}{}_1$ =0.0195 mg, $A^{(T)}{}_2$ = 33.542 min, and $A^{(T)}{}_3$ = 3.10 min are transverse fitting parameters and $A^{(L)}{}_1$ =0.0293 mg, $A^{(L)}{}_2$ = 43.881 min, and $A^{(L)}{}_3$ = 11.78 are the longitudinal parameters. The

mass loss per unit of length is shown in Figure 45. The result of this experiment shows that the two flow regimes are present at the same instance and the bleeding along the direction of the fibers is more significant compared to the transverse flow, where the spreading as a medium occurs.

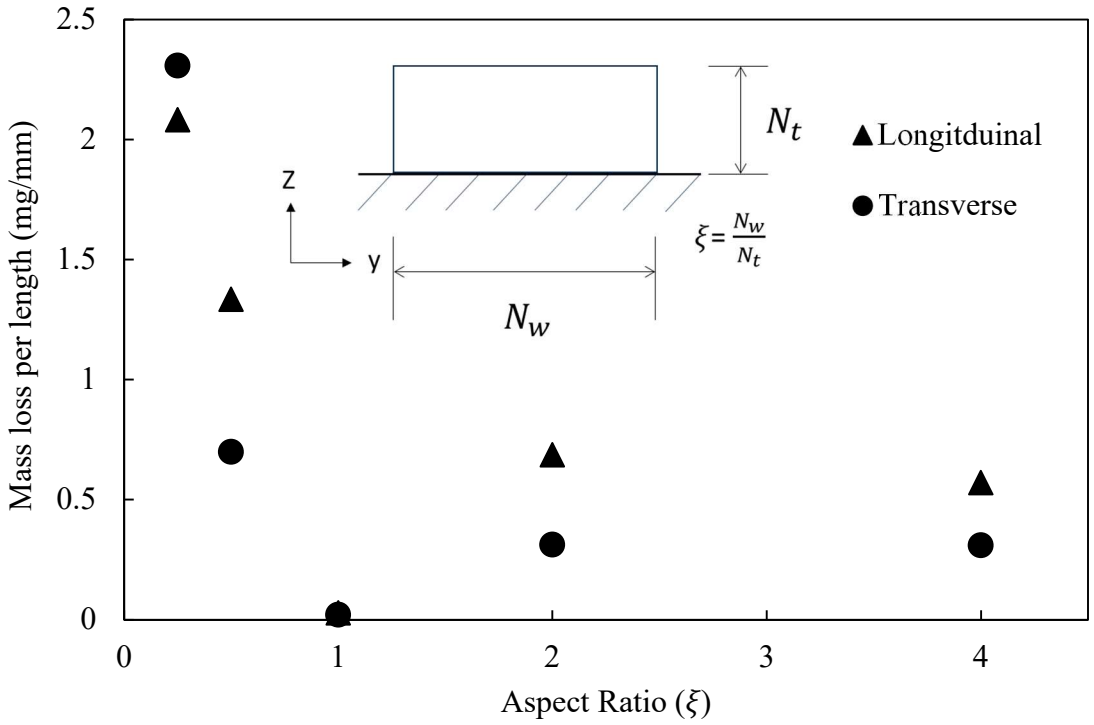

Figure 45. The mass per unit length with respect to the aspect ratio

Unlike the roller deposition, the compaction of the prepreg in the autoclave results in a loss of the resin. This changes the fiber volume fraction of the prepreg. This indicates that a model for the change in the fiber volume fraction is needed to properly simulate the prepreg during cure. However, since the material system is different between the non-crimp fabric and the prepreg, the evolution of the fiber volume fraction is different.

The experimental data indicates that the resin begins to flow between 20 and 30 minutes into the cure cycle, eventually reaching a plateau. This plateau is attributed to decreased permeability and increased viscosity. Additionally, resin mass loss data was utilized to quantify the

fiber volume fraction as a function of through-thickness strain. Thermogravimetric analysis (TGA) revealed an average initial fiber volume fraction of 0.55 [106]. The machine used for the analysis was a Shimadzu TGA-50 (Figure 46a) using a platinum pan with a stirrup. The temperature was ramped from 20 ºC to 600 ºC.

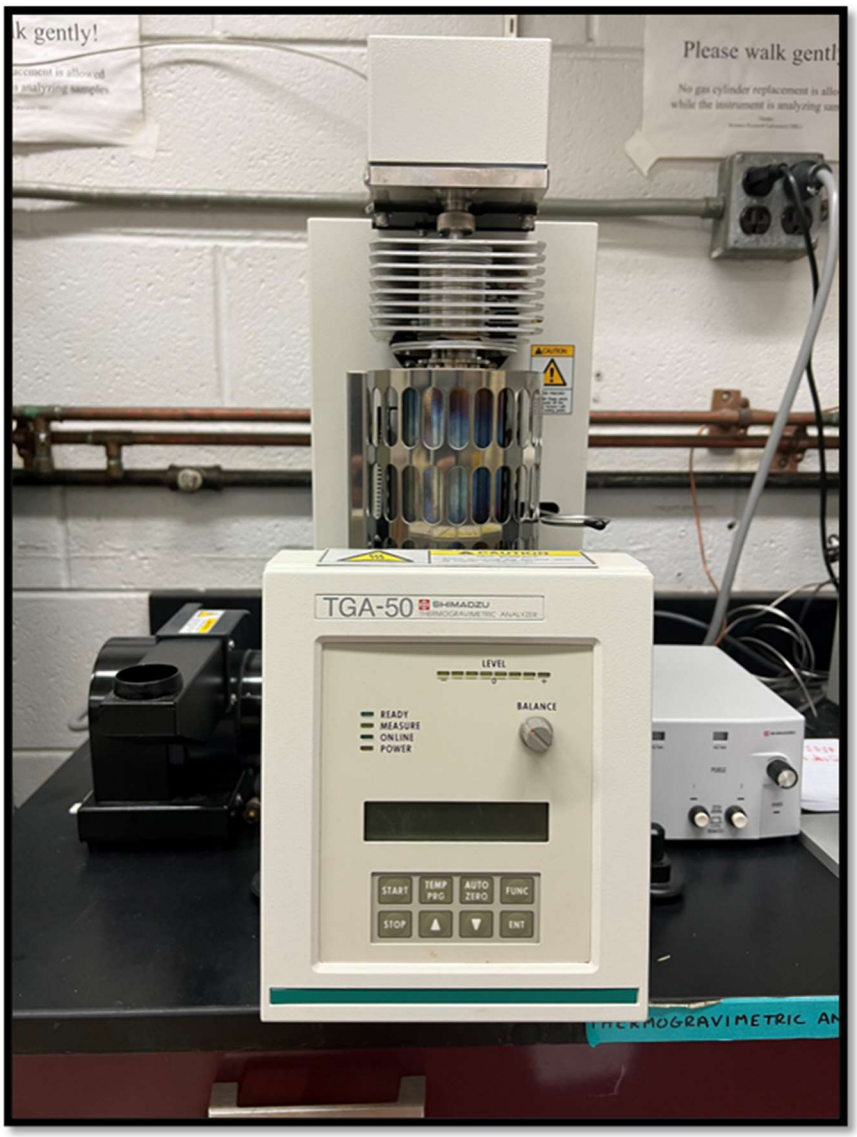

(a)

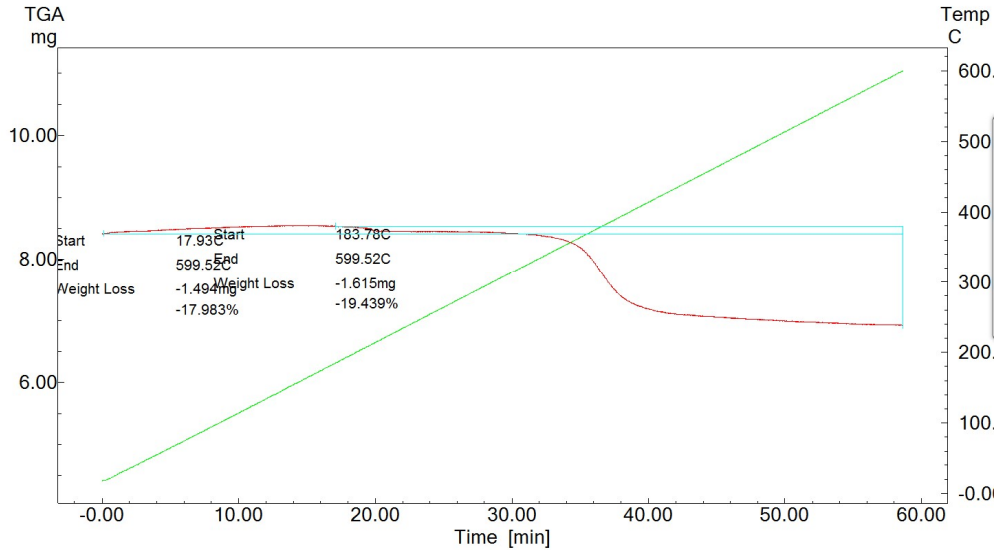

(b)

Figure 46. a) Shimadzu TGA-50, used for the TGA experiments to determine the initial fiber volume fraction. b) The dynamic tests which measured the mass loss due to the resin burning

The result of the dynamic test is shown in Figure 46b. The initial resin weight was determined using the matrix volume fraction from TGA analysis as depicted by the initial plateau of mass. Using the known densities of the matrix and fiber, the fiber volume fraction ascertained via the rule of mixtures. The change in width and length, along with the known initial volume of a single unidirectional tow ($\xi = 1.0$), was employed to calculate the through-thickness strain, ε_{33}, over time. This methodology facilitated the fitting of fiber volume with respect to the compaction strain, as illustrated in Figure 47. showing an exponential plateau.

$$V_f(\varepsilon_{33}) = V_{f_0} + B_1 * e^{\left(\frac{-B_2}{\varepsilon_{33}}\right)} \tag{60}$$

where $B_1 = 0.0673$ *and* $B_2 = 0.0084$ are fitting parameters, ε_{33} is the strain in the compaction direction and V_{f_0} is the initial fiber volume fraction. The fiber volume fraction exhibited a rapid increase during the initial stages of compaction, followed by a plateau as permeability decreased and resin viscosity increased. Additionally, the resin bleed-out observed at the beginning of the

cure cycle impacted the squeeze flow through the evolution of the fiber volume fraction, subsequently affecting the anisotropic apparent viscosity as described in Equations (17-20). The formulation of the fiber volume fraction was empirically determined for the specified cure cycle and material system. The methodologies employed can be adapted for different temperature profiles and composite materials. With the resin bleed-out and fiber volume fraction development characterized for the current cure cycle, a single-phase model was constructed where the resin was not explicitly modeled. Explicitly modeling the resin flow can be accomplished with higher resolution models; however, this approach necessitates computationally intensive representative volume elements to capture microscopic behavior. The present analytical equation provides a sufficient estimation of the evolution of the fiber volume fraction.

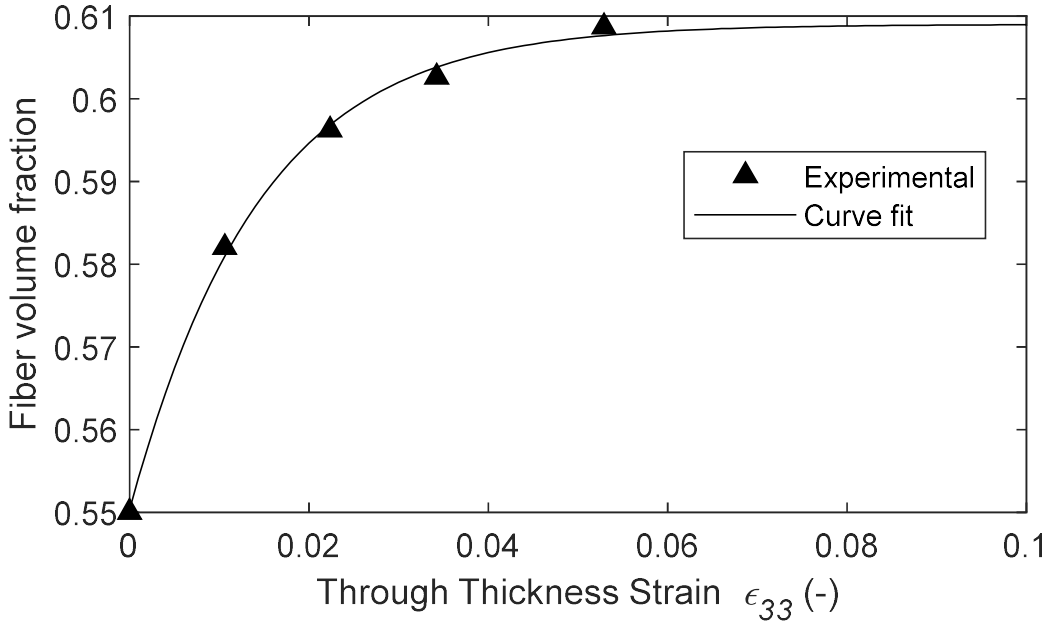

Figure 47. The fiber volume fraction plotted with respect to the strain

4.3.2 Modeling and validation of compaction behavior in unidirectional tows

The compaction results of the unidirectional tows revealed that thicker samples exhibited more tow spreading compared to those with a greater width. For a configuration involving a single tow (ξ =1), the maximum compaction strain was observed to be 0.053 at 90 minutes into the cure cycle. The highest compaction strain, ε_{33}=0.137, was recorded for four tows arranged in the thickness direction (ξ =0.25), whereas the smallest strain, ε_{33}=0.012, was found for the four tows arranged in the width direction (ξ =4.0). This range in observed compaction strain highlights the considerable influence of tow geometry, particularly the thickness of the ply, on the squeeze flow behavior.

The undeformed and deformed configurations of the unidirectional models are presented in Fig. 46a. The baseline configuration for the unidirectional models with one ply (ξ =1.0) shows a reduction in thickness and tow spread in the Y-direction (transverse to the fibers). The modeling results, in terms of through-thickness compaction strains, were compared with experimental measurements to validate the proposed flow-compaction model. Figure 48b - 48d shows the spreading originating from the center of the tow and spreading transversely. The thicker samples show a more consistent spreading while the thinner samples show an uneven distribution of the spreading on the surface of the composite. The consistent trend between the experimental and numerical results indicated that transverse spreading increased with more plies through the thickness and decreased with more tows across the width.

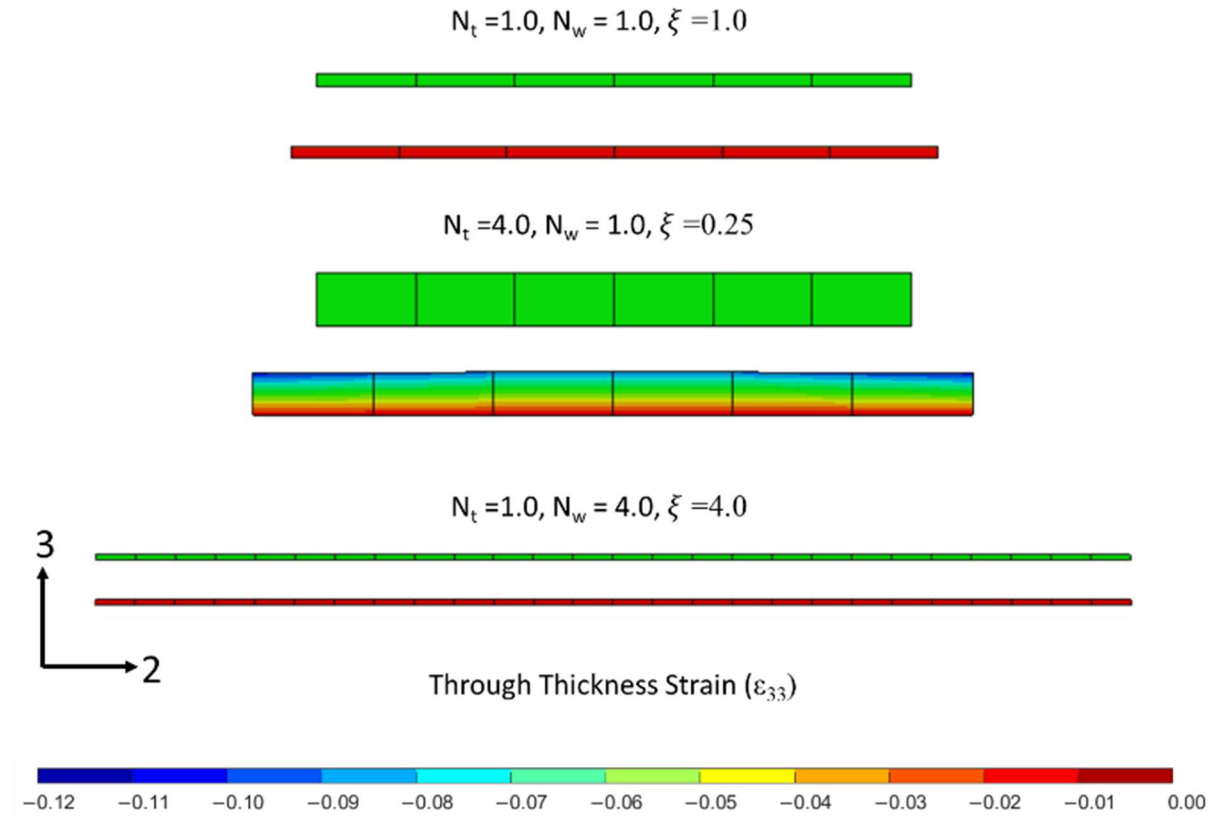
N_t =1.0, N_w = 1.0, ξ =1.0
N_t =4.0, N_w = 1.0, ξ =0.25
N_t =1.0, N_w = 4.0, ξ =4.0
3
2
Through Thickness Strain (ε33)
−0.12 −0.11 −0.10 −0.09 −0.08 −0.07 −0.06 −0.05 −0.04 −0.03 −0.02 −0.01 0.00

(a)

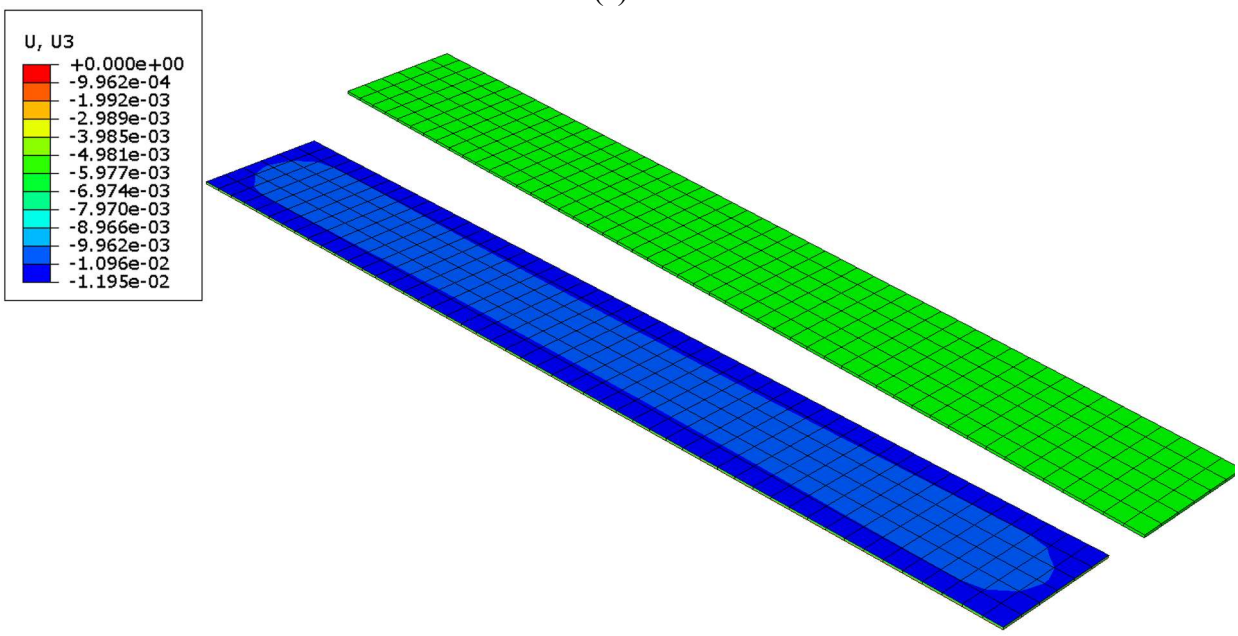
U, U3
+0.000e+00
-9.962e-04
-1.992e-03
-2.989e-03
-3.985e-03
-4.981e-03
-5.977e-03
-6.974e-03
-7.970e-03
-8.966e-03
-9.962e-03
-1.096e-02
-1.195e-02

(b)

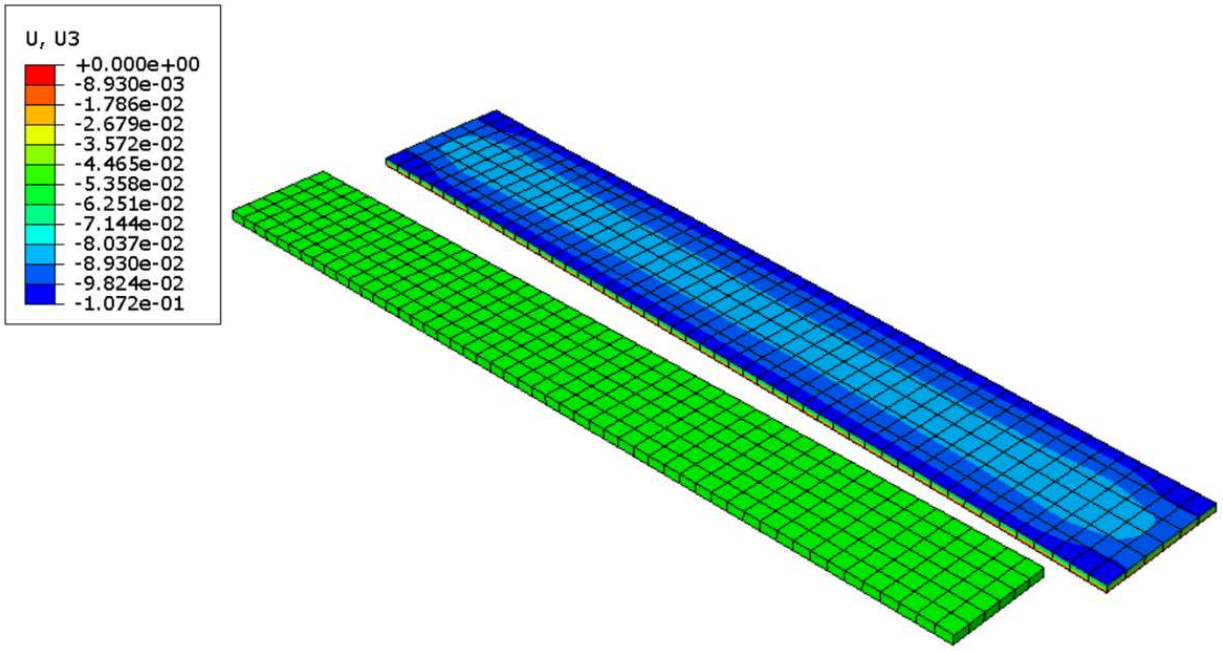

(c)

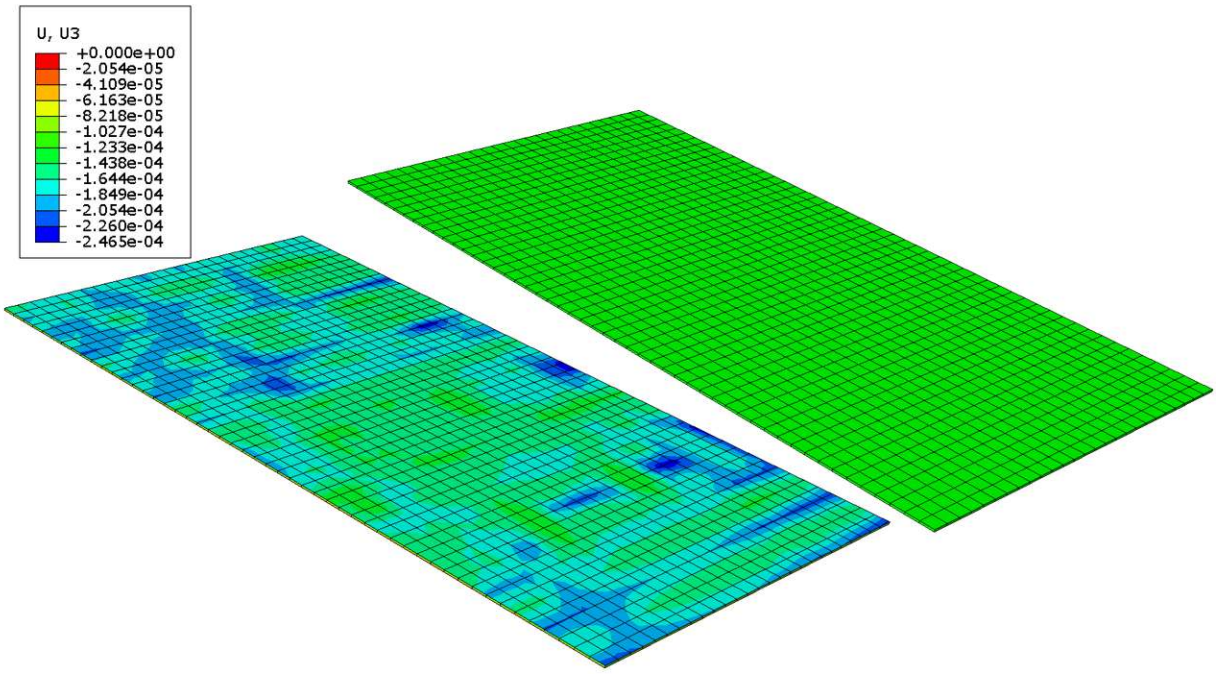

(d)

Figure 48. Unidiretional numerical models for the baseline of a one tow wide and thick composite (ξ =1.0), a four ply thick composite (ξ =0.25), and a four ply wide composite (ξ =4.0)

The through-thickness strains, ε_{33}, in the FEA models of unidirectional tows were quantified using the average displacement on the top y-x surface and the known initial thicknesses. Figure 49a illustrates the rapid decay of through-thickness strain, ε_{33}, at 30 minutes into the hold stage with respect to the aspect ratio. The tow thickness during the compaction simulations and experimental measurements followed a non-linear visco-hyperelastic curve, decreasing with the aspect ratio (Figure 49b). Both the experimental and modeling predictions of compaction showed close agreement up to 90 minutes of the hold stage, with a noticeable deviation at the end of the hold stage.

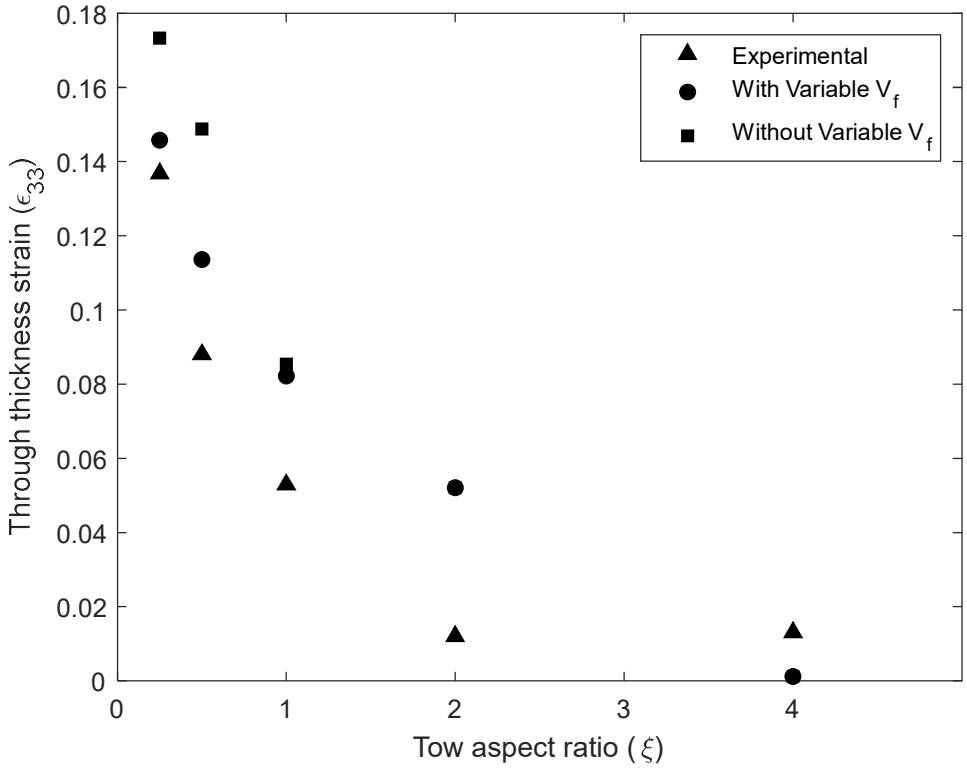

(a)

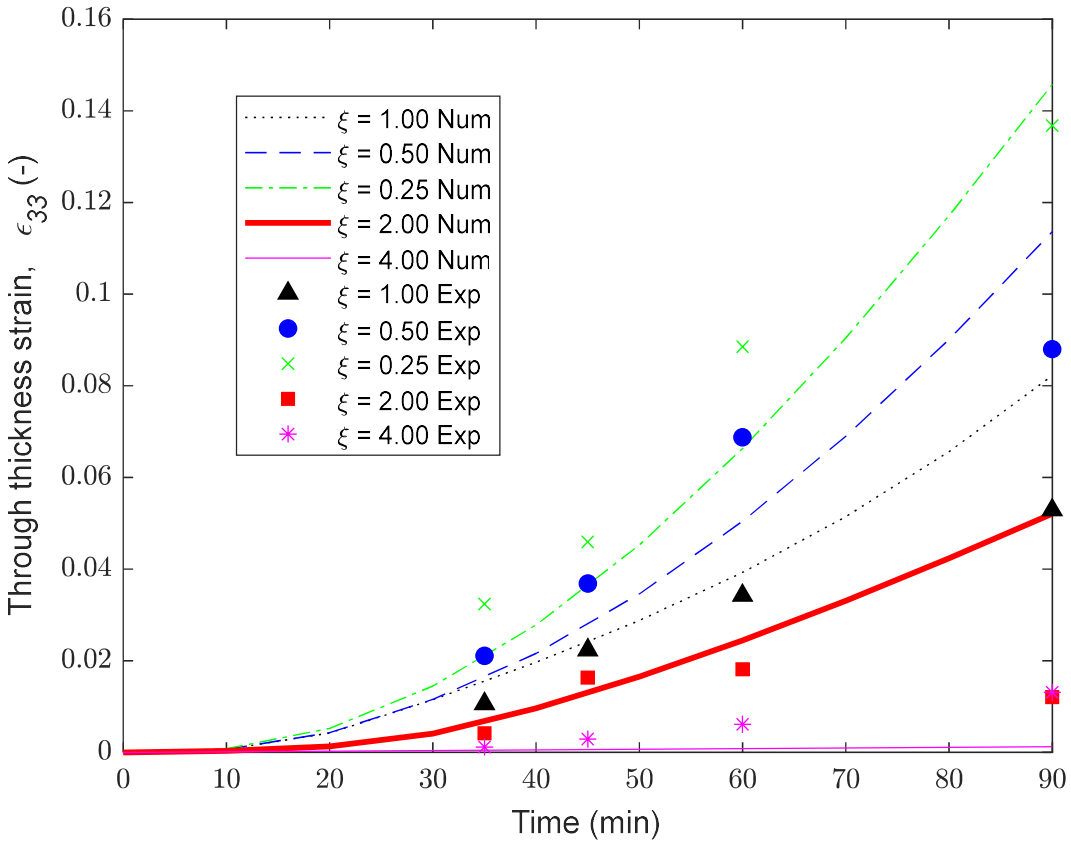

(b)

Figure 49. (a) The strain of the unidirectional elements with respect to the aspect ratio. (b) The through thickness strain of the experimental and numerical unidirectional sample with varying aspect ratios

4.3.3 Squeeze flow simulation of layup with embedded tow gap

The initial micrograph of the X-Z plane of the sample, featuring a single tow gap, is presented in Figure 50a. This micrograph was obtained by supporting the laminate with two binder clips and capturing images of the edge displaying the visible gap using a microscope. When the sample was encased in resin, and polished the progression of the sample is shown in Figure 50b and the final polish is shown in Figure 50c. The polishing allowed for a more accurate measurement of the ply drop into the missing fiber tow gap. The sample shows that the top ply

appears to have subsided into the gap, while the middle ply exhibits expansion towards its center. An average angle of 5.59º, measured using the fiber angles at the point where the two 0º plies met.

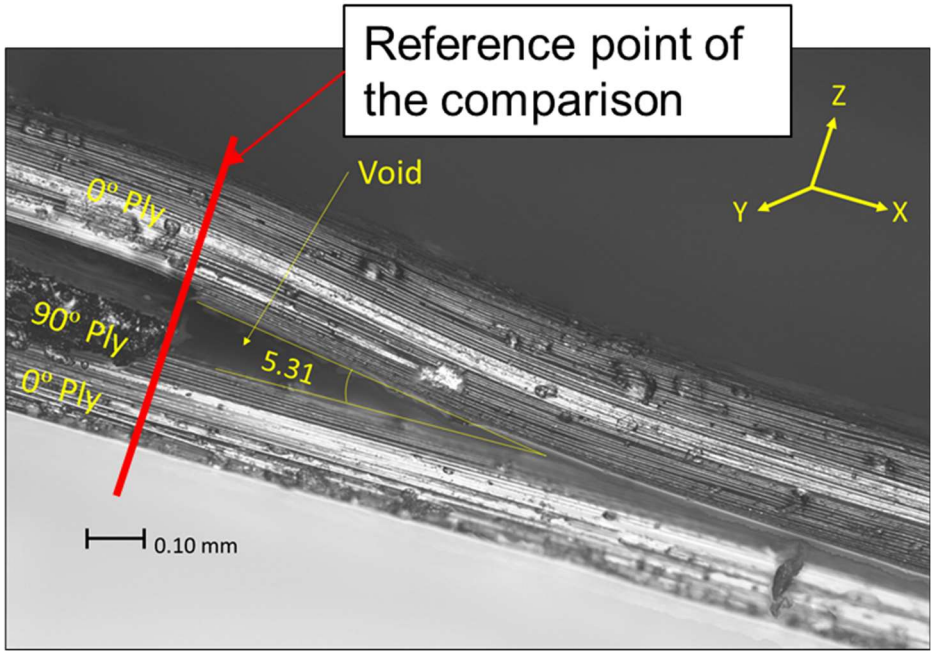

(a)

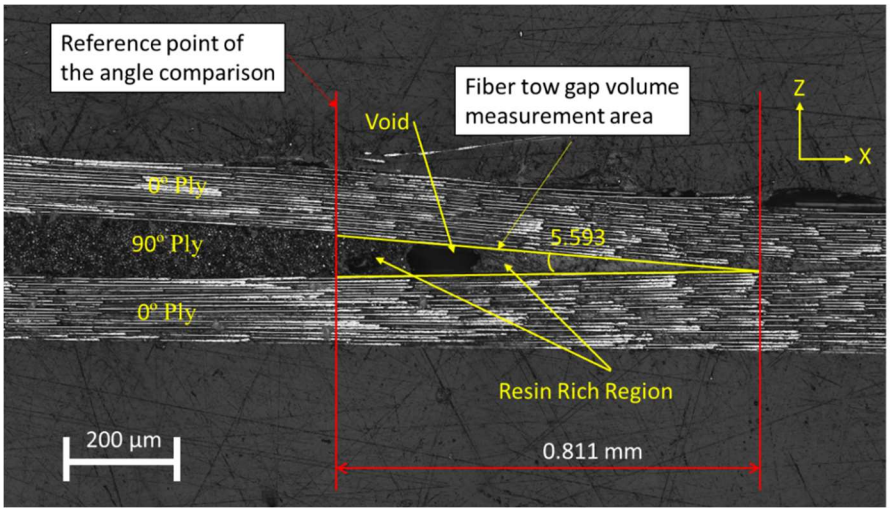

(b)

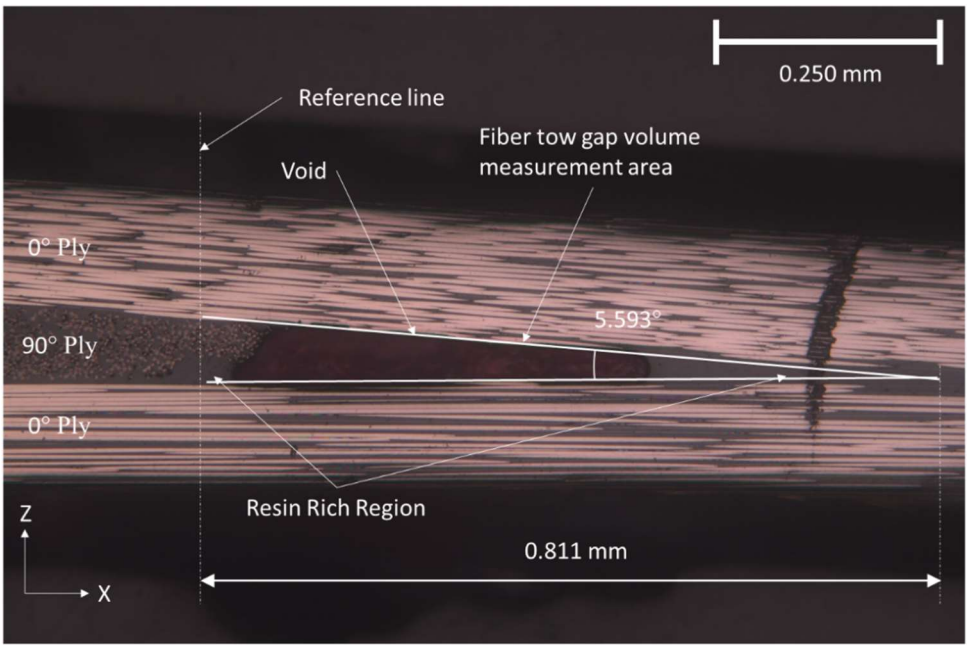

(C)

Figure 50. a) The pristine fiber tow gap without any polishing, b) Rough polish of sandpaper of the micrograph of the fiber tow gap. c) The final polish with diamond paste of the micrograph of the fiber tow gap

To further validate the proposed compaction constitutive model, an analysis was conducted on the region surrounding the fiber tow gap. The initial undeformed configuration of the fiber tow gap model is depicted in Figure 51, which illustrating the layup compaction during the simulation. The fiber direction of the upper 0º ply was measured as shown in Figure 52. The initial finite element analysis (FEA) did not account for the coupling between squeeze flow and resin bleed-out, which will be addressed in a subsequent section. The top ply sank into the fiber tow gap, creating a curvilinear triangular void near the edge of the 90º ply. Early in the cure cycle (before 13 minutes), the gap closed rapidly until the autoclave pressure reached a maximum of 0.541 MPa (80 psi). Following this initial closure, the gap volume decreased gradually until the end of the isothermal hold stage. Tow spreading was observed at the edge of the 90º ply.

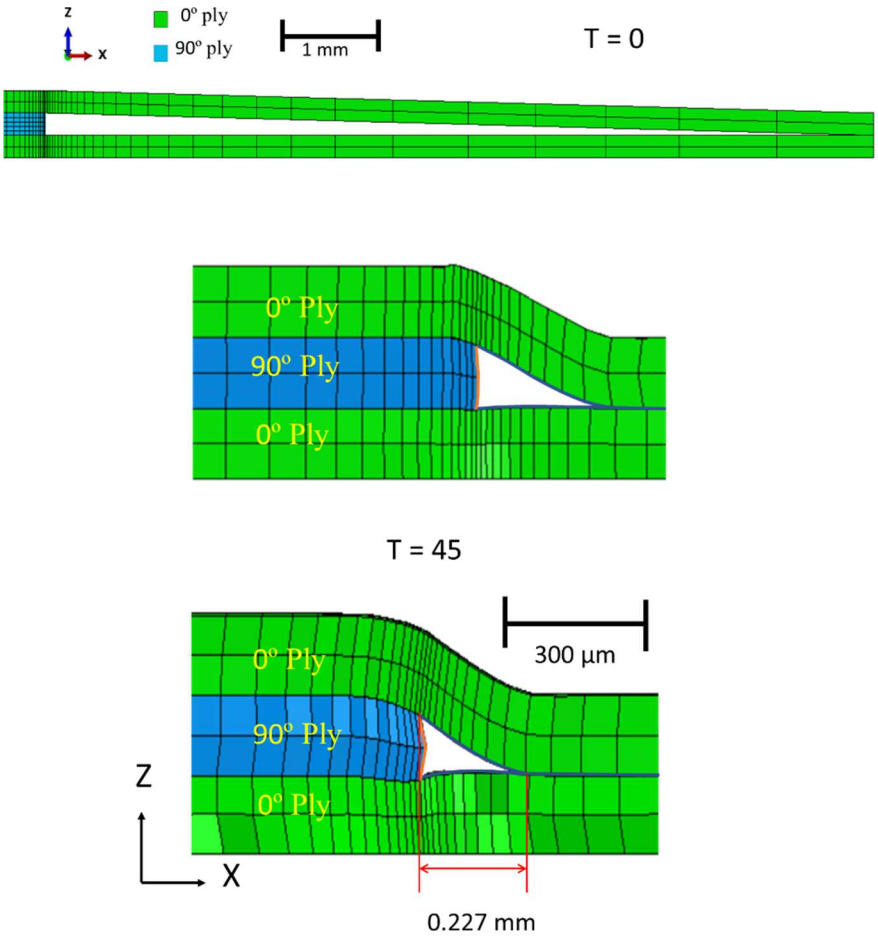

Figure 51. The fiber tow gap model with the gap divided into four section and the fiber tow gap modelling results without internal gap pressure.

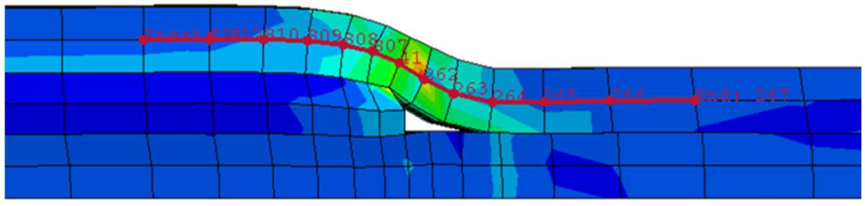

Figure 52. An example of the path of points measured for the angle of the fiber direction

The simulation results, which considered only squeeze flow, were compared to an experimentally manufactured sample featuring the fiber tow gap. The micrograph of the area of

interest, shown in Figure 50c, reveals the morphology induced by the fiber tow gap, wherein the top 0° ply sank into the gap. A resin-rich region formed due to resin bleed-out from adjacent plies. The experimentally observed resin-rich region was significantly larger (0.811 mm in length) compared to the one predicted by squeeze flow analysis (0.227 mm in the closed gap (Figure 53). The simulation depicted a much steeper slope in the top 0° ply than that observed in the physical sample. The discrepancy between the predicted and observed tow morphology can be attributed to resin bleed-out, which provides support against the sinking of the 0° ply. This result underscores the necessity of considering resin bleed-out to accurately capture the cured defect morphology.

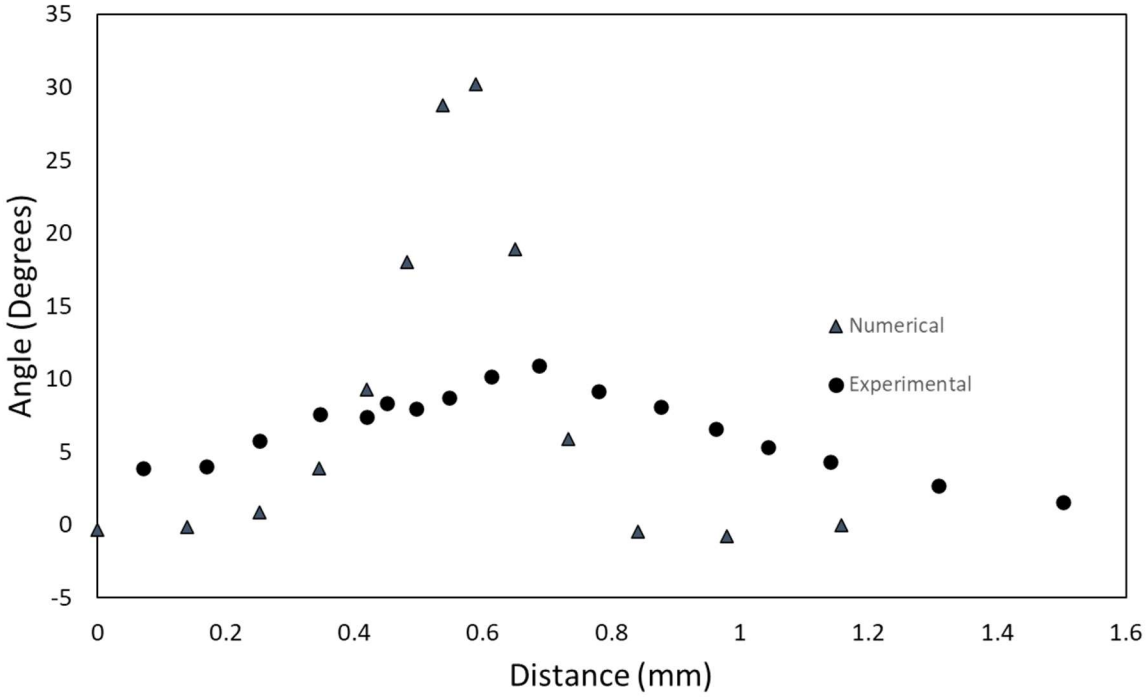

Figure 53. The tow angle comparison measured at the top 0º ply. The angle drops too steeply in comparison to the experiment.

4.3.4 Effect of resin bleed out during compaction of layup with embedded tow gap

When heat and pressure are applied, resin bleeds out of the porous fiber bed which is influenced by factors such as resin viscosity, local fiber volume fraction, applied autoclave pressure, and pressure distribution throughout the laminate [89]. The experimental results for unidirectional tow compaction indicated that resin bleed out occurs primarily at the initial stages of the manufacturing process, with distinct flow behaviors in the longitudinal and transverse directions relative to the fibers. The resin expelled in each direction was removed from the composite and weighed, and the mass loss in each direction was calculated as a ratio of the measured resin mass.

The squeeze flow simulation of the fiber tow gap was used to track the changes in the gap volume. The size of the void in squeeze flow analysis was shown to rapidly decrease because of top ply sinking, where the void volume quickly dropped from 0 to 13 min and then plateaued. However, it is evident that resin bleed out occurs simultaneously with the squeeze flow in the preliminary stages of the cure cycle (Fig. 54) which slows down the volume of the gap from decreasing. In order to capture the coupling between the two phenomena, the squeeze flow and the resin bleed out, the following procedure was used. The volume of the bled-out resin was estimated using the following equation:

$$V_{Res}(t) = \frac{\bar{\rho}_P{}^{(T)}(t) \cdot SA_{Gap}}{\rho_r} \tag{61}$$

where the density of resin, ρ_r, was 1100 g/cm^3, SA_{Gap} is the initial surface of the fiber tow gap volume $V_{Gap}(t)$, which changes during the compaction, and $\bar{\rho}_P{}^{(T)}$ is the experimentally determined resin bleed out areal density for the prescribed cure cycle, as given by Eq. 62. The surface area is

based on the gap geometry as shown in Fig. 50. The partitioned length in the gap is added together and multiplied by the fiber direction length of laminate as shown in Eq. 62.

$$S_{A_t} = l_0 \sum_{n=1}^{4} l_i \tag{62}$$

Where l_i is the length of the section and l_0 the length of the tow in the y-direction. A simulation of the fiber tow gap was used to track the changes in the volume of the void over time. The coordinates of the edges of the fiber tow gap, l1-4, as shown in Fig. 55, was used to calculate the volume of the void.

$$V_{Void} = \frac{1}{2} w\, A_{Gap}(t) \tag{63}$$

where w is the width, and $A_{Gap}(t)$ is the area of the fiber tow gap on the x-z surface during cure cycle time.

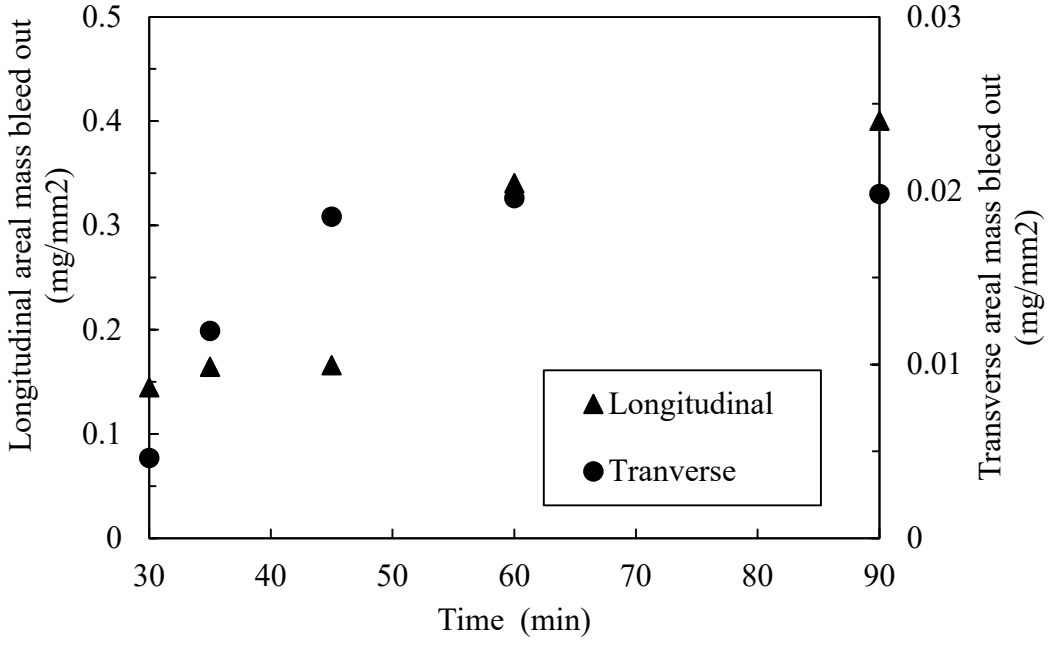

Figure 54. An estimated mass loss fraction over time of the fiber tow gap using experimental data from unidirectional experiments

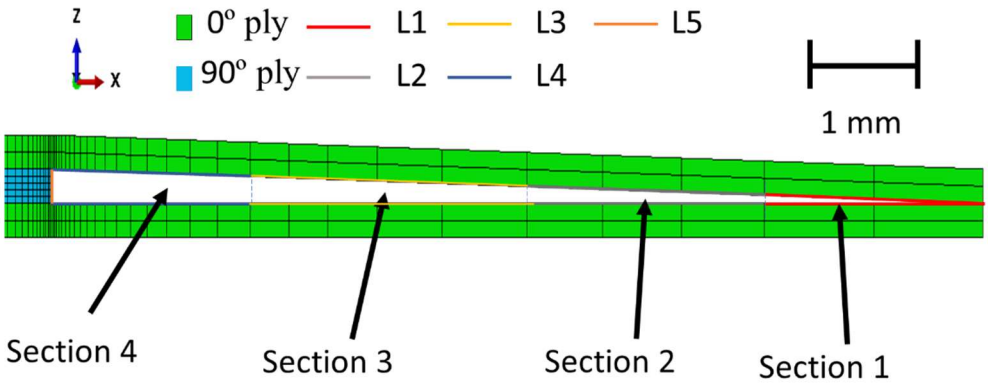

Figure 55. The partitioned length in the fiber tow gap with.

Over time, the volume of the gap region, $V_{Gap}(t)$, is expected to decrease due to ply sinking and squeeze flow, while concurrently, the volume of the bled-out resin, $V_{Res}(t)$, is anticipated to increase. Once the volume of the bled-out resin matches the volume of the tow gap void where the resin-rich region is formed, the gap will be filled with resin. According to the squeeze flow simulation, this gap filling is predicted to occur at t_{fill} =26 minutes (Fig. 56). Experimentally, the volume of the resin pocket, as observed in the micrograph, is shown as a horizontal line in Fig. 49c. This volume, determined from the micrograph in Fig. 49b, corresponds to the volume of resin in the gap at approximately 29 minutes, indicating a progressive filling and coupling between the squeeze flow and resin bleed out.

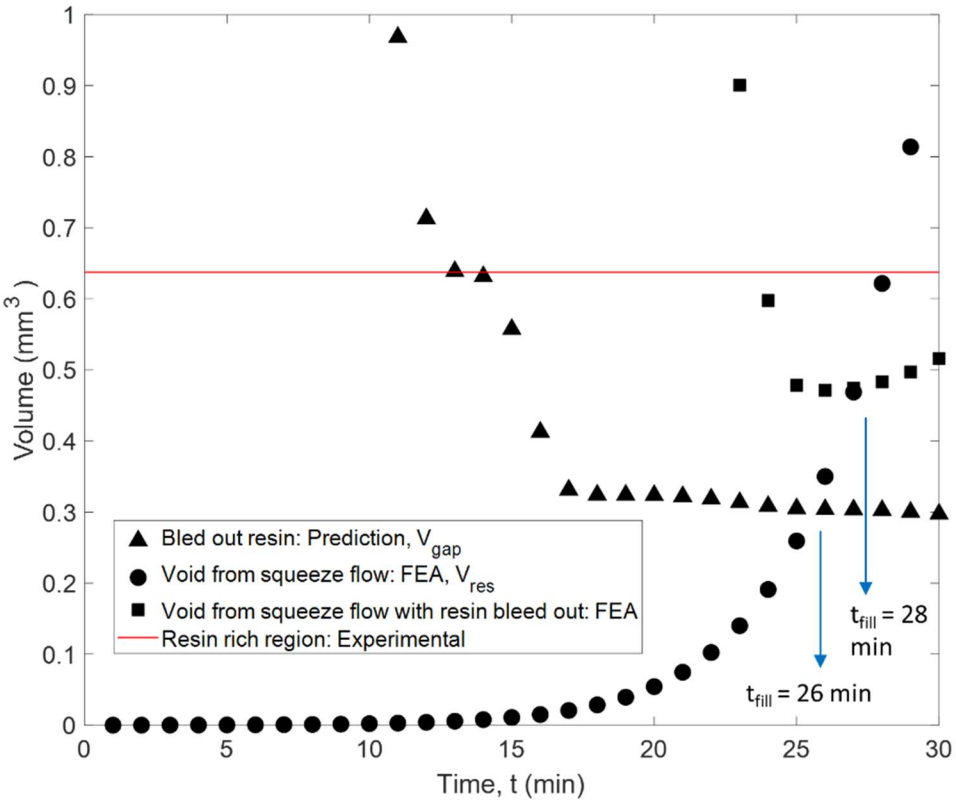

Figure 56. The measured volumes of the model, a theoretical mass flow volume and the experimental gap volume measured from the micrograph.

To describe this flow coupling effect, a pressure matching the autoclave pressure was applied to the internal surfaces of the closing gap to account for the presence of bled-out resin as it fills the void. To simulate the progressive filling of the gap, the internal void pressure was activated gradually in partitioned regions 1-4, as shown in Fig. 55, until the predicted time, t_{fill}, when the gap void is supported by the resin. The internal pressure was applied starting from the symmetrical end of the model, selected based on the proximity of the void surfaces in that region. This pressure was activated at 6, 12, 18, and 24 minutes, respectively. To capture the stress relaxation effects in the viscoelastic liquid resin, the applied pressure followed a linear decrease over 25 minutes (Fig. 57) the time was selected to correspond to the overall time of filling of the tow gap region. The

initial sinking of the fiber tow gap was slowed by the addition of pressure. With the addition of the pressure, the initial sinking of the fiber tow gap was slowed. With incorporation of the coupling between squeeze flow and resin bleed-out, the void filling was predicted to occur at a later time than in squeeze flow analysis (28 min compared to 26 min), which was closer to the moment corresponding to predicted time of filling (at 29 min) based on the experimental size of the resin rich pocket.

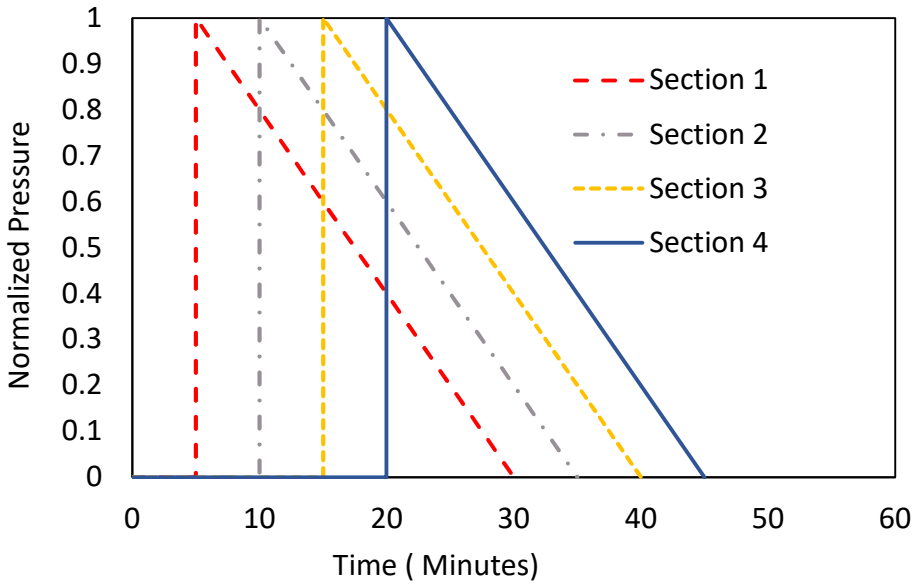

(b)

Figure 57. The timing of the internal resin pressure.

4.3.5 Fiber volume measurement in cured layup with fiber tow gap

Predictions of the variable volume fraction of the 90º ply is shown in Fig. 58a. A micrograph of the center 90º ply from the cured sample was discretized into rectangular sections where the fiber volume fraction, V_f, were quantified using pixel measurements. Each partitioned section

counted the darker areas and calculated the ratio between the lighter colors to the darker resin. The micrograph (Fig. 58b) showed V_f range of 0.40-0.57 with a resin rich region in the top corner that had V_f of about 0.10. FEA simulations predicted V_f to range from 0.57 to 0.60. This study did not consider the initial distribution of the local fiber volume fraction that can account for some of this variation.

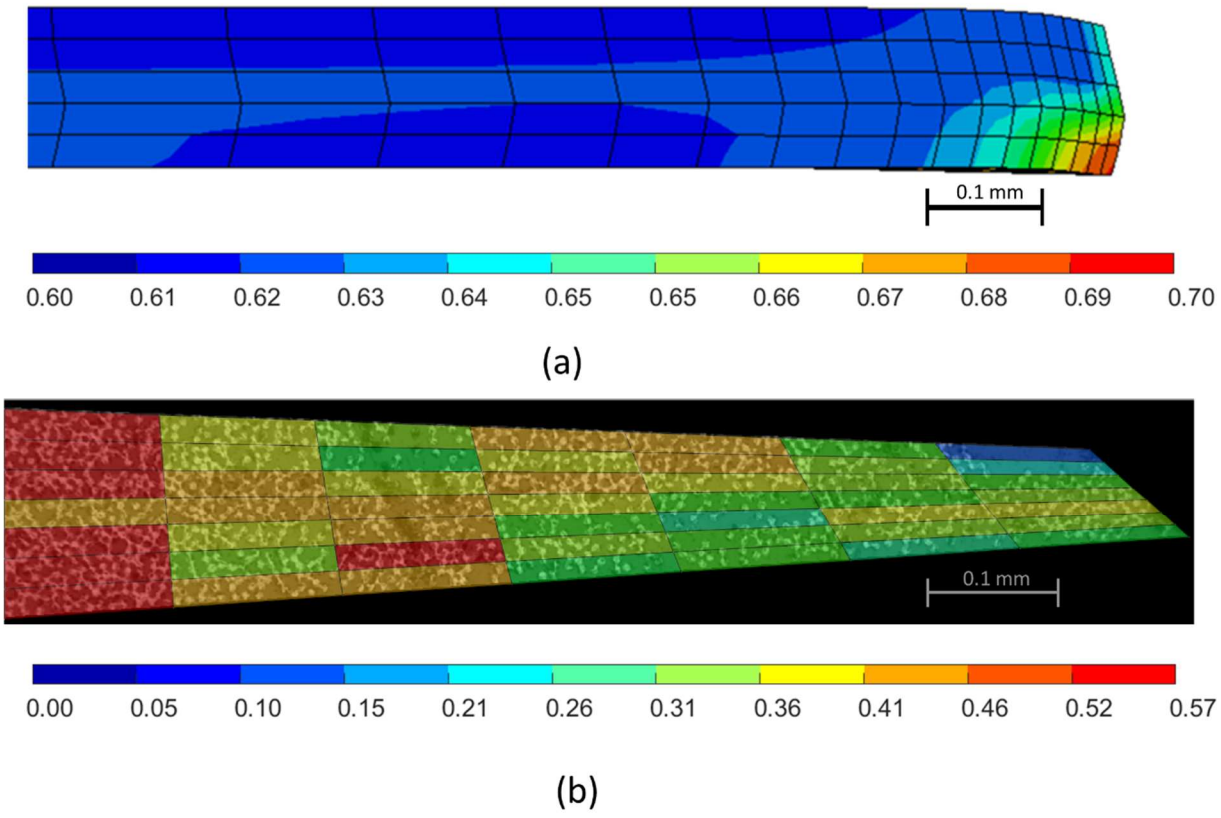

Figure 58. a) The distribution of the fiber volume fraction in the fiber tow gap simulation of the 90º ply. b) The measurement of the fiber volume fraction of the 90º ply micrograph divided into sections.

4.3.6 Evaluation of morphology in cured layup with fiber tow gap

With the bled-out resin providing structural support against the sinking ply above the tow gap, the final morphology of the fiber tow gap model with the internal void pressure is shown in Fig. 59. Compared to the other model (Fig. 52) the two FEA models (squeeze flow with and without the effect of resin bleed out) at 13 minutes, the void pressure applied prevented the ply from sinking too rapidly. The out-of-plane waviness for the top 0º ply, during the hold stage (45 min), was more gradual and developed over a larger distance, which matched the experimental observation.

The proposed multi-physics modeling approach effectively uses a sequential simulation of the flow-compaction, where the results of the squeeze flow simulation are used to inform the void evolution in the coupled flow simulation. The local compaction strain was connected to the volume fraction using eq. (19) and it allowed to consider the interaction between percolation and squeeze flow. The amount of resin flowing into the fiber gap filles the empty space inside of the void before resin gelation, which was captured in FEA simulation by adding an internal void pressure. This resin provided structural support against the sinking ply. The final morphology of model with the internal void pressure in the fiber tow gap is shown in Fig. 59. When comparing the two FEA models at 13 minutes, the internal pressure applied in the fiber tow gap prevented the ply from sinking too rapidly.

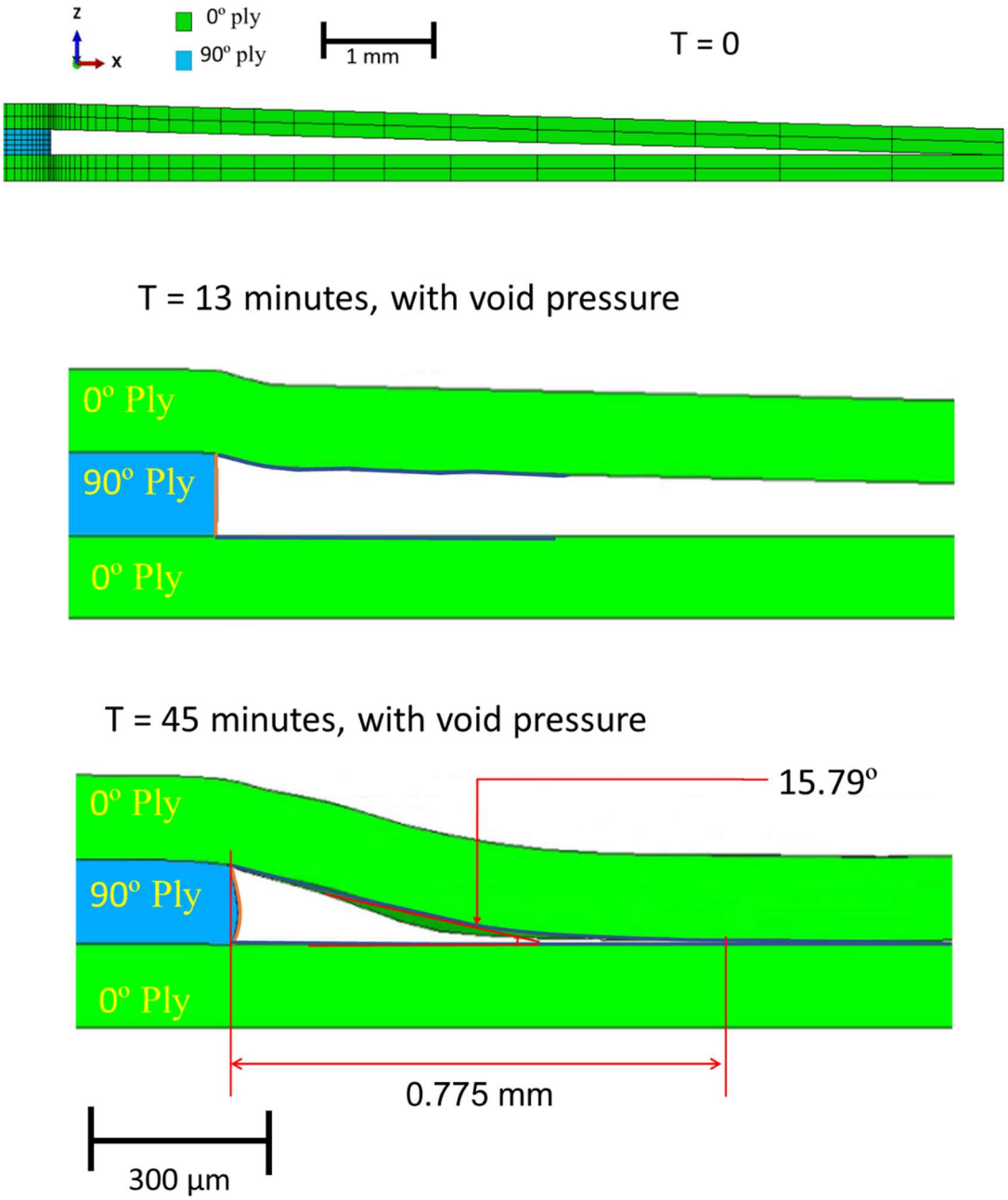

Figure 59. The fiber tow gap model with the gap divided into four section and the fiber tow gap modelling results without internal gap pressure.

The fiber angle of both models was measured using the path feature in Abaqus like the example shown in Fig. 60. The angle vectors between the nodes were measured using their

coordinates and captured the evolution of waviness along the length of the gap; however, the experimental results were not as steep as the modeling prediction. The size of the predicted resin-rich region from the coupled simulation had a length of 0.946 mm (compared to the 0.227 mm without the internal void pressure), which agreed with the experimental size of 0.811 mm. The thickness variation of the bottom 0º ply is shown in Fig. 61. The measured thickness in the micrograph was found to increase from the left of the reference line towards the center of the composite. In comparison, the numerical model followed a curve which had the thickest part at the reference line and decreased in both directions. The resulting morphology can be utilized in further analysis of the composite, such as through progressive damage analysis, to compare with fabricated laminates in the future [107].

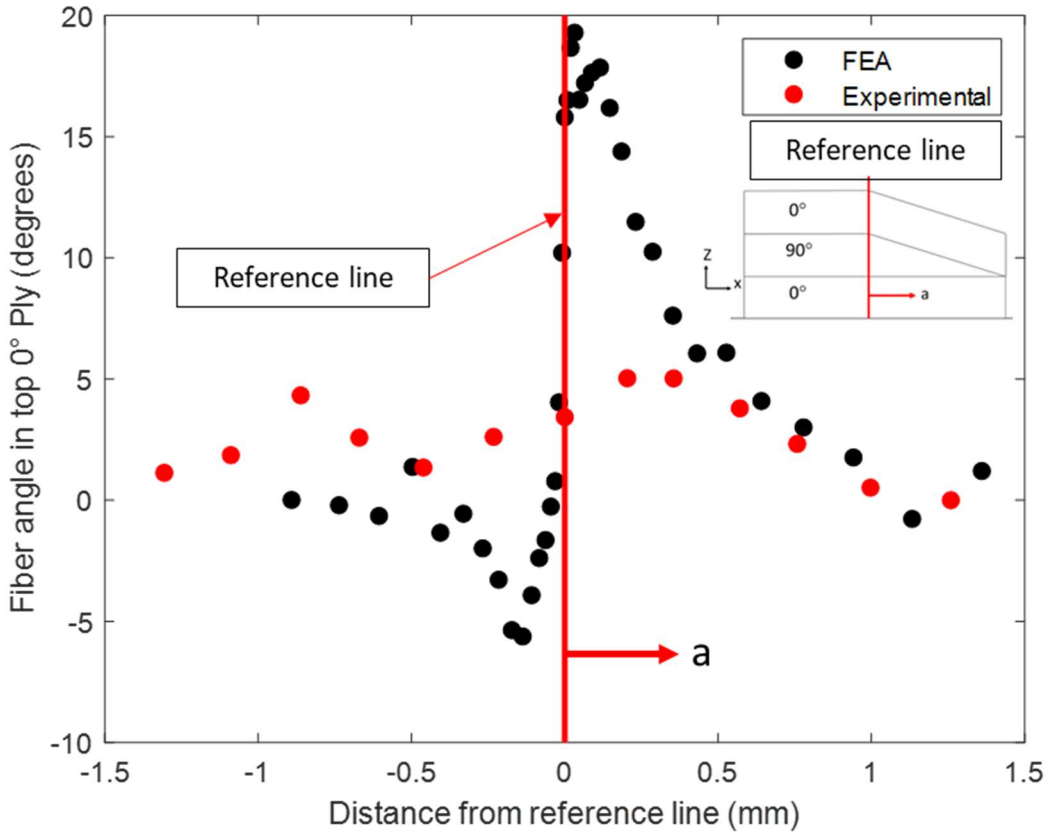

Figure 60. The angle with respect to the distance from the reference point at the edge of the 90-degree ply.

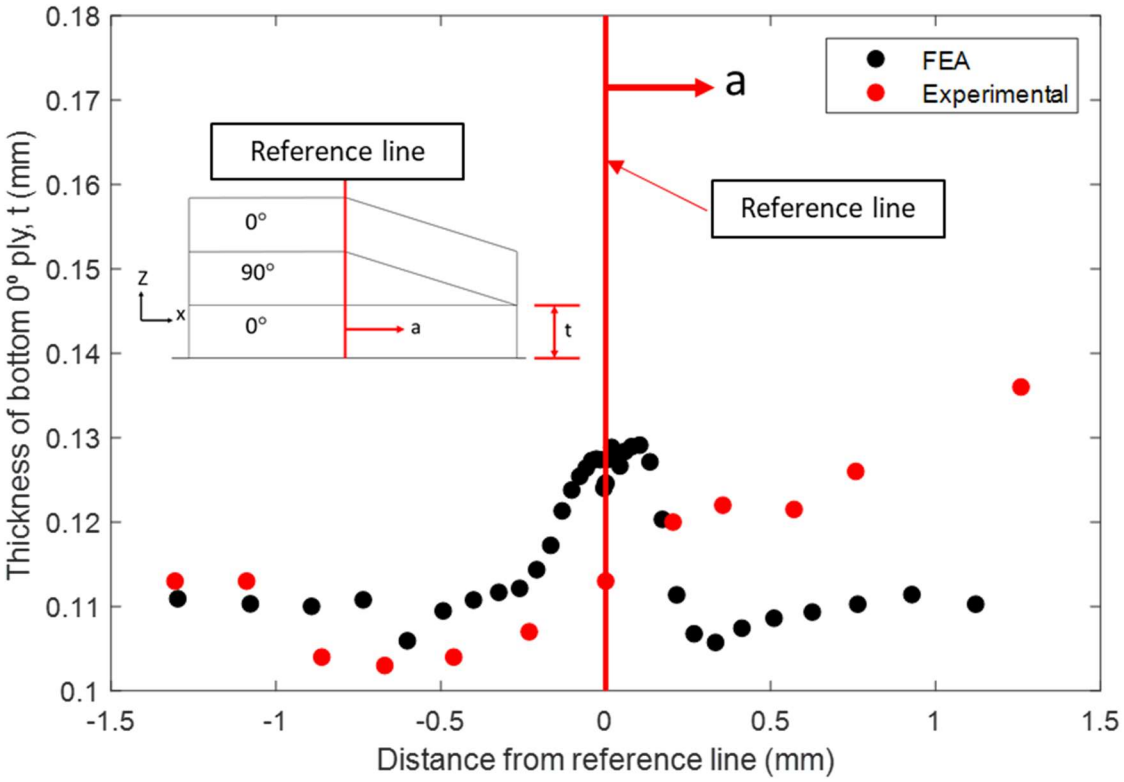

Figure 61. The ply thickness with respect to the distance from the reference point.

4.4 Resin bleed out and deformation in a laminate with a staggered defect

Layup defects result in irregular morphology when the composite is cured and compacted especially when numerous defects are present through the thickness. To analyze the quality of the model, the area near these fiber tow gaps were measured. The presence of these defects typically results in non-linear deformation for both the 0° and 90° plies. Unlike the single tow gap model, the thickness of the composite is affected by a distribution of temperature. This results in a variation in the viscosity of the composite through the thickness.

The initial configuration of the staggered defect model is shown in Fig. 62. The maximum pressure is reached at 13 minutes. In a composite with a single tow gap, it results the top ply rapidly

closing, and forming a void near the defect region [21]. However, in the staggered defect model, the increased stiffness due to the number of layers results only in a slight deformation on the edges of the 90° plies for both the models with and without void pressure as shown in Fig. 62. The addition of the void pressure causes the ply to deform upwards. This indicates that the timing of the pressure and the stiffness of the laminate must be accounted for when applying this technique.

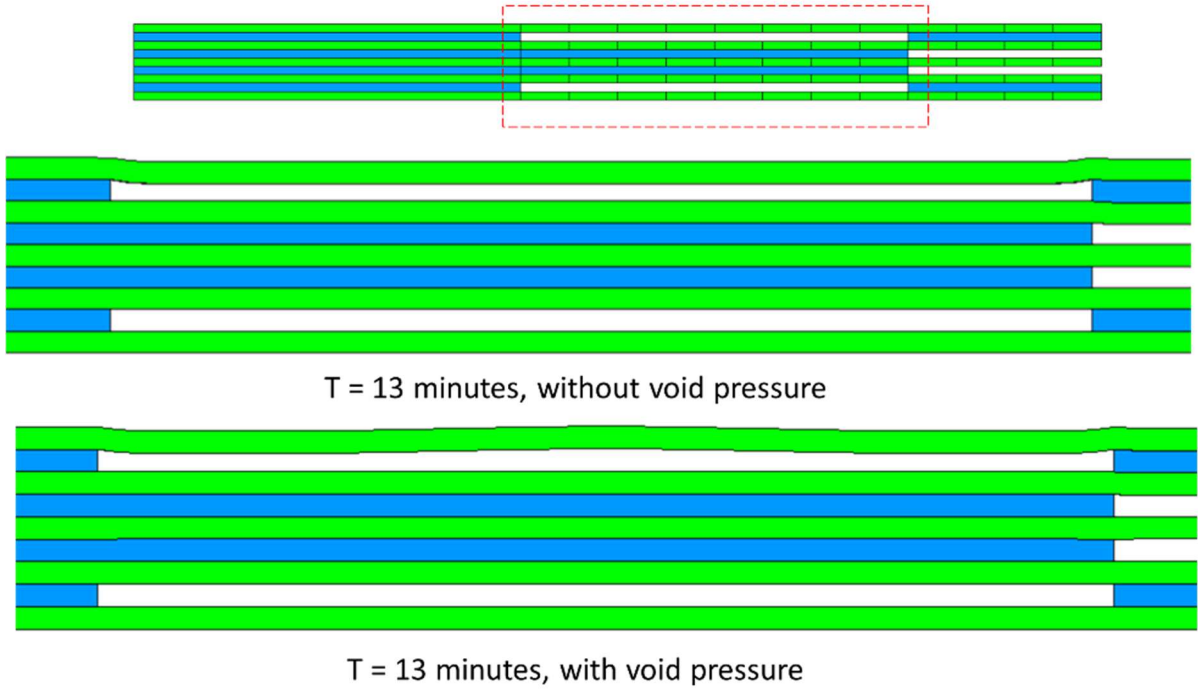

Figure 62. The geometry of the staggered defects at 13 minutes into the cure cycle where maximum pressure is achieved for

The micrograph in Fig. 63 shows resultant morphology after the final cure of the composite with a staggered defect. It shows that all the 0° plies sank into the gap and formed voids around the edges of the 90° plies. As for the model, the top 0° is shown to sink first before the other gap defects which forms void in the defect region. The morphology at 40 minutes into the cure cycle in Fig. 64 shows that the top ply sinks but a larger void is predicted by the model at the lower gaps. At the top 0°, without the addition of the internal void pressure, the ply sinks rapidly at steep

angles. This was a similar result to previous single fiber tow gap models without the influence of the outflow of resin [26]. The size of the gap in the micrograph was measured to be 0.864 mm. In comparison, the model without the internal void pressure shows a gap of 0.310 mm. Furthermore, the increased stiffness of the structure impedes the ply from sinking at the bottom layers. This resulted in large voids at the bottom gaps as opposed to all gaps fully closing in the micrograph.

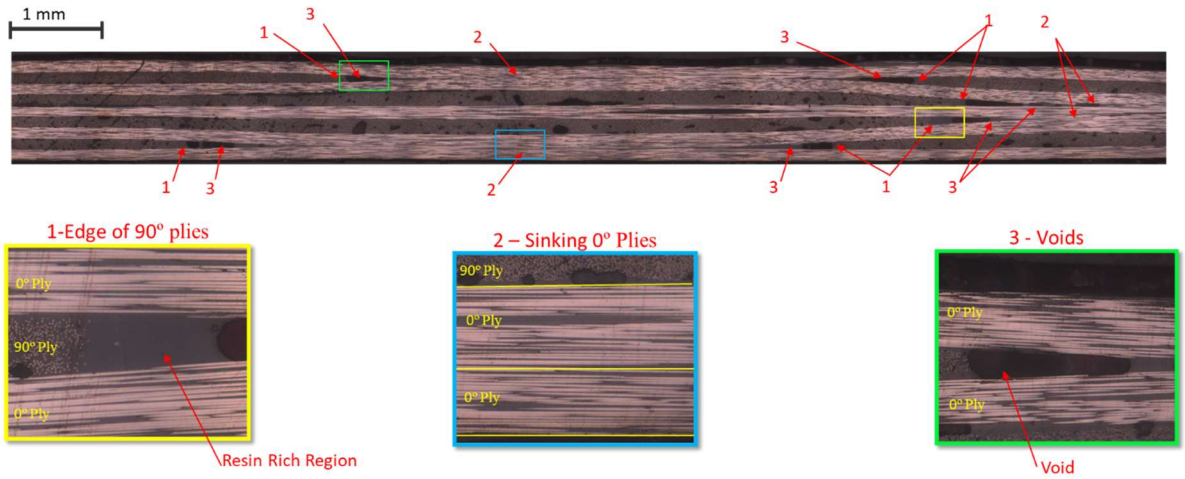

Figure 63. The several types of defects where they occur in the laminate with multiple fiber tow gaps and overlaps

The addition of the void pressure shows the effects of the percolation flow in a complex structure was not fully captured. The internal void pressure hindered the sinking of the ply which resulted in the larger voids in the fiber tow gap. Furthermore, a void was formed in the middle of the 0° ply which is not present in the micrograph. This shows that the addition of the internal void pressure was overestimated for more complex composites and needs be evaluated further for more complex composites. This includes the heat transfer through the system, since it was assumed, the composite had a constant temperature throughout the structure. The percolation flow as a function of the resin viscosity so it can be assumed it was not equal through the structure. This means that the time-based activation of the internal void pressure needs to be reevaluated for thicker

composites. Instead, a chemo-rheological approach such as applying permeability and a mass transfer analysis for future models would produce more accurate results.

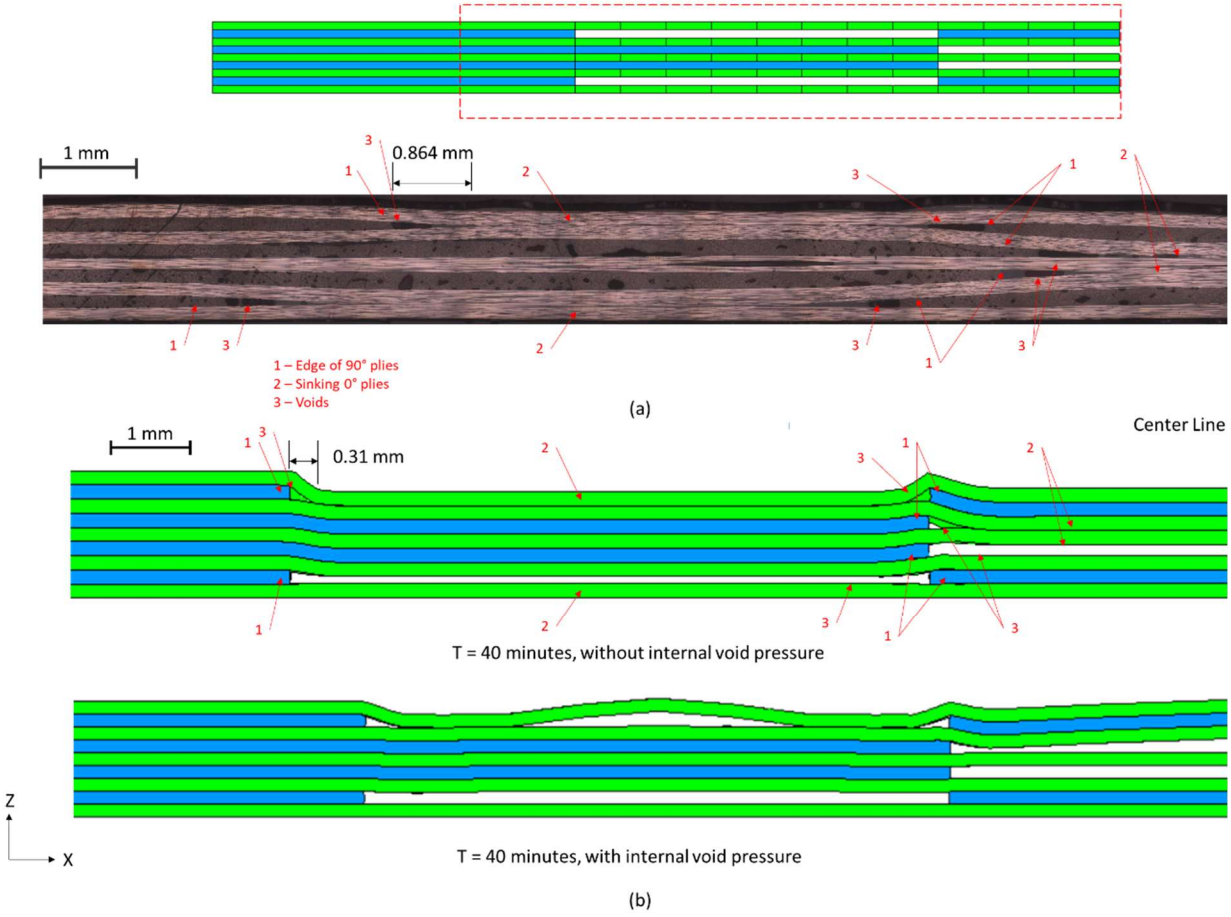

Figure 64. (a) A micrograph of the staggered defect sample which highlights the morphological areas of interest such as the edges of the 90° and the sinking 0° plies. (b) Two finite element models, with and without the internal void pressure, of the staggered defect at 40 minutes into the cure cycle.

5 Conclusion

Composites are versatile materials which have a variety of manufacturing processes. However, the manufacturing of composites, inevitably results in deposition defects. These defects propagate into non-linear deformation which results in morphology that compromise the strength of composites. The manufacturing process of composites is a complex process which involves multiple physical phenomena. However, understanding these multistage processes are necessary to produce quality composite structures. To fully understand the manufacturing of composites, a proposed method was to simulate the manufacturing process via FEA. For this research, HP-RTM and AFP was the two manufacturing processes that was studied.

To illustrate the compaction behavior of a composite weave, a model of a Non-Crimp Fabric (NCF) via a roller compaction process was developed. This model was constructed using a constitutive compaction model for NCF within High-Pressure Resin Transfer Molding (HP-RTM), incorporating both linear elastic and viscous components. The viscous component included terms dependent on strain and strain rate, utilizing fiber volume fraction and compaction speed, respectively. Parameters for the apparent viscosity were derived from data obtained through multiple compaction experiments at varying velocities, which elucidated the time-dependent behavior of the NCF. To simplify the Finite Element Analysis (FEA) modeling, the quasi-isotropic stacking sequence was homogenized into a single transversely isotropic element. Simulations were conducted for three different compaction speeds on a single NCF element. The results demonstrated that the model accurately simulates the stress-strain response of a non-crimp fabric with a fiber volume fraction basis across all three velocities applied. This validation confirms the

model's capability to properly replicate the stress-strain response of NCF. The multilayer NCF roller compaction model effectively simulated the distribution of fiber volume fraction through the fabric's thickness. The maximum fiber volume fraction was observed at the center of the NCF, decreasing towards the bottom and the edges. Wrinkling predominantly occurred away from the center of compaction. The findings indicated that the maximum fiber volume fraction is proportional to the strain rate, whereas the average fiber volume fraction remains unchanged with varying strain rates. This demonstrates that while strain rate influences the distribution of fiber volume fraction, it does not affect the overall average fiber volume fraction, thereby impacting the flow of resin through the laminate.

For the deposition of tows on a composite substrate, experiments were conducted on unidirectional samples with varying compaction force and laminate prepreg thickness. A robotic system was utilized to deposit composite tows via a heated roller, laying tows on increasing layers of composite substrates. The results indicated that tow spreading was significantly influenced by the compliance of the composite substrate. In fact, the tow contracted in certain cases during the tow deposition experiments conducted in this work. The FEA model's heat transfer component was calibrated using the experimentally measured temperature data. The compaction behavior of the prepreg was characterized by a highly coupled hyper-viscoelastic model and a chemo-rheological model, previously employed in AFP composite process modeling. This model was applied to both the composite substrate and the composite tow in the FEA model, under the same variations of force and substrate thickness as the experiment. Although conducted on a smaller scale, the experiment provided a viable approach to investigating AFP parameters such as force and substrate thickness in the deposition process. The results of the experiment and the finite element modelling demonstrates that an increase in thickness of the composite substrate significantly affects the

deformation of the tow. This variation in deformed tow width is due to a combination of the substrate compliance and the heat conduction through the substrate. As the substrate becomes more compliant both the tow and the substrate experiences deformation as the tow is deposited. Furthermore, the hyperelastic properties of the composites is influenced by the temperature. The low conductivity, relative to the rigid tool, causes the heat to dissipate slower in the top layers of the composite substrate which causes both the substrate and the tow to be more viscous.

Furthermore, the tow spreading behavior was also attributed to the variations in substrate compliance and the elastic recovery of the substrate. Specifically, on the release of pressure from the roller, the substrate exhibited an elastic recovery effect, pushing the tow inwards and resulting in tow contraction, particularly evident in thicker substrates. The interaction between these phenomena results in the elastic recovery of both the composite substrate and the tow which further influences the variations in tow width. Knowing these interactions during the deposition of the composite tow allows a degree of prediction for when fiber tow gaps/overlaps occur during the AFP deposition process.

After the deposition, the same interconnected multiphysics framework was used to simulate the compaction of thermosetting prepreg in order to predict complex morphology. With the addition of resin, an anisotropic tensorial prepreg viscosity was used to capture tow spreading during the cure cycle. The deformation in unidirectional and fiber tow gap samples was observed to be a result of the coupling between the squeeze flow and resin bleed out. Resin bleed out was quantified by measuring the volume of the resin outflow from unidirectional prepreg tape. The bled-out resin was found to fill the void in the samples with a single fiber tow gap. To capture this phenomenon the sequential compaction analysis was proposed and validated. As the first step, squeeze flow simulation allowed for the estimation of the time of filling of the void with resin. At

the second step, the calculated time of void filling was used to activate the internal pressure inside of the void. This resulted in the cured morphology that captured the non-uniform morphology more accurately around the initial tow gap region.

To further enhance the multi-physics modeling approach, a sequential simulation of the flow-compaction was considered, where the results of the squeeze flow simulation are implemented to capture the evolution of void filling. Instead of modeling the resin explicitly, a one phase model was made which incorporates the resin bleed out via the development of the microscopic parameters, and the filling of the gap. The compaction strain was connected to the local fiber volume fraction, and it allowed the model to consider the interaction between resin bleed out and squeeze flow. The modeling framework demonstrated that morphological features develop due to the coupled manufacturing phenomena and cannot be considered in isolation from each other. The phenomena include the chemo-rheology of the resin, and visco-hyperelasticity of the laminate in the early stages of curing. The initial deposition gap regions develop into the non-uniform morphological features in the composite, which includes the non-uniform ply thickness, fiber waviness, resin rich regions, and the fiber volume fraction variation. Moreover, the proposed multi-physics modeling framework can be adopted to accommodate various material systems with different chemo-rheological properties. The proposed sequential modeling approach has been used to predict cured morphology in more complex layups with spatially distributed, staggered fiber tow gaps [52]. The models presented in the present work can be decoupled and can modified for a more accurate solution in future work. This includes taking the uncertainty into consideration with the initial parameters, in order to obtain a more accurate prediction of the mass transfer.

Finally, a finite element model of the staggered defect composite was made and simulated until the first hold stage of the manufacturer's cure cycle. Results shows that the ply sinking was

rapid without the internal void pressure developed in the simulation with a single tow gap but also was hindered at the bottom plies due to the increased stiffness of the multiple layers. The addition of the internal void pressure shows the effects of the time-based activation was overestimated resulting in larger voids compared to the micrograph. Since the flow of resin is dependent on the viscosity, the internal void pressure activation must be reevaluated and consider the distribution of heat and mass transfer. The results of the model with multiple fiber tow gaps shows that the internal void pressure timing was insufficient to properly model the resultant gap. Therefore, improvements can be made for a more accurate prediction.

The overall work shows that an experimentally informed FEA model has the capability to simulate the various material systems and the different stages of manufacturing. The work presented today was only the start of a potential field to explore for the digital thread of composite manufacturing. With a predictive approach to composite manufacturing, the deposition induced features can be predicted and their effect on the strength of the finished composite. From when the composite is first laid on the tool onto the final stages of the curing process and beyond, a modelling approach a computational model can enhance the quality of fiber reinforced composites.

6 Future Work

6.1 Relaxation of Composite fabric

After the NCF is compacted, the resin is infused into the mold and cures. During this time, the textile undergoes viscoelastic stress relaxation. This is due to the time-dependent readjustment in fibrous materials, including composites [108], [109]. Over time, the load required to maintain the reduced thickness decreases which must be modeled accordingly for the creation of a digital twin [94]. This phenomenon can be quantified using the hydraulic compaction experiment. Previous experiments have shown that the maximum stress is affected by the strain rate [9]. Therefore, the time-dependent properties can be incorporated into the model. A typical stress-strain responses are shown in Fig. 65.

Previous studies have modeled the stress relaxation for glass fiber composites so the same method can be applied for NCFs [110]. The model uses a Maxwell–Wiechert model which uses linear springs and dashpots in a series to model the stress relaxation behavior of a viscoelastic material as shown in Eq. 64 [18].

$$\sigma(t) = \sigma_0\big(V, v_f\big) + \sigma_1 e^{\left(-\frac{t}{\tau_1}\right)} + \sigma_2 e^{\left(-\frac{t}{\tau_2}\right)} \tag{64}$$

Where σ_0 is the long-term stress as a function of the fiber volume fraction. The σ_1 are σ_2 are stress coefficients and τ_1 andτ_2 are time coefficients. The variable σ_1 is greater than σ_2 and the former is responsible for the initial large drop in stress, while the latter gradually decreases over time towards the equilibrium stress. Consequently, τ_1 is greater than τ_2 since the drop happens quickly after the NCF is unloaded.

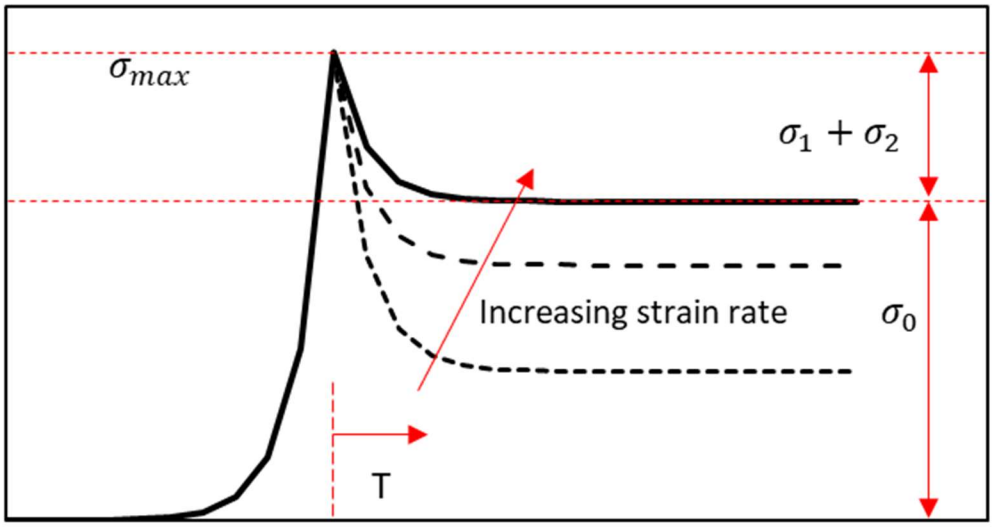

Figure 65. A typical normalized stress over time plot of a compaction and relaxation of a material which shows the maxwell variables.

The Maxwell coefficients must be determined to fully simulate the relaxation phase of the NCF manufacturing. In the case of σ_0, previous work has shown the equilibrium stress is dependent on the maximum stress [111], [112]. In the current model, the maximum stress found in the NCF is proportional to the strain rate for the same through thickness strain. Therefore, the long-term stress can be scaled according to both the compaction velocity and the fiber volume fraction. For the other parameters ($\sigma_1, \sigma_2, \tau_1$ and τ_2) must be determined though curve fitting for each of the experiments through a non-linear least squares algorithm [110]. For the creation of a relaxation model, it would be insufficient to so the parameters for every configuration. Therefore, any trend for the maxwell parameters will be investigated for any dependence on the fiber volume fraction and the compaction speed [110], [113], [114]. Experiments have been conducted for the relaxation of NCFs such the plot shown in Fig. 66. However, more experiments need to be conducted in order

to fully determine if the trend can be fitted to the maxwell coefficients. Furthermore, the plot derived from the data shows larger strain rates which is typically present in HP-RTM applications.

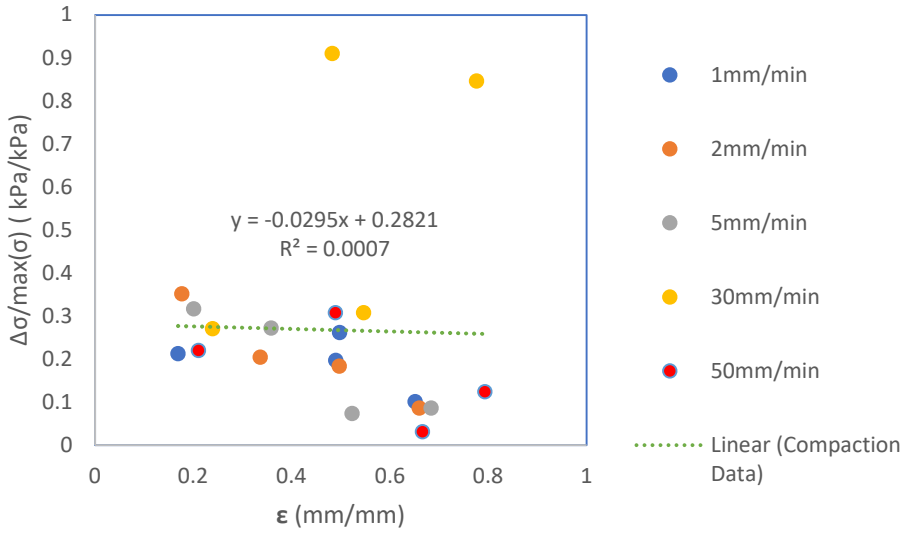

Figure 66. An experimental curve depicting the ratio between the relaxation stress and the maximum stress based on the maximum strain.

6.2 Wrinkling model for composite fabric and steered composite tows

When compacting tows in a mold with complex geometry or depositing tows on a substrate, out-of-plane deformation may result due to the curvilinear geometry (Fig. 67) [115], [116]. For the wrinkling in NCFs, the interaction between the plies or the interply shearing is fundamental in predicting this out-of-plane behavior [116]. When placed on a curved mold, the friction between the mold and the ply and between plies may result in large voids which can result in resin rich regions. In the fast-paced manufacturing process, such as HP-RTM, this wrinkling could significantly influence the resulting strength. Therefore, to predict the effects of the tool and subsequent layers of NCFs, may be necessary for a more accurate measurement of strength after the curing process.

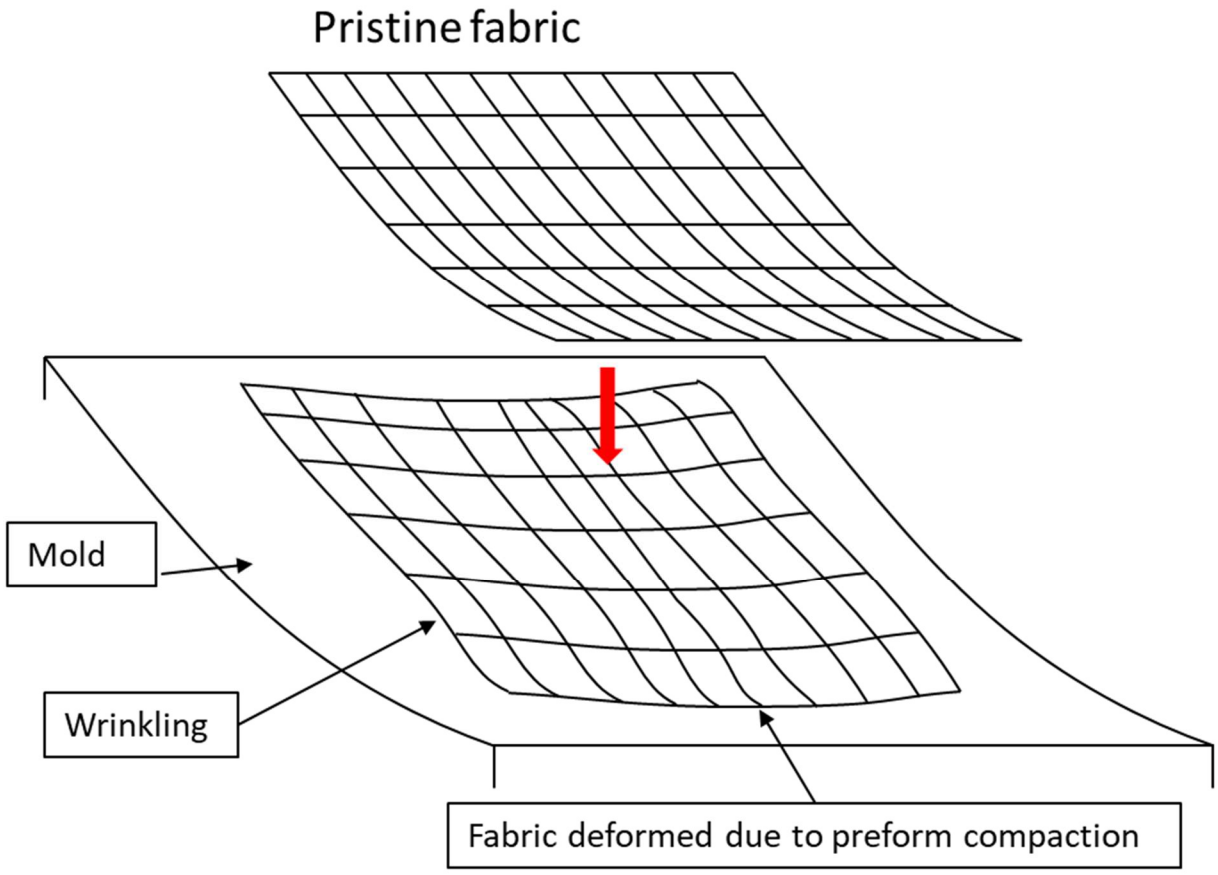

Figure 67. Schematic of the wrinkling of composite fabric on a curved tool

The wrinkling from the deposition (Fig. 68) may also be a result of the friction between the tow and the ply and the between plies. Although, tows can be cut and restarted [17], it increases the occurrence of gaps and overlaps within the laminate. A straight uncut composite typically has better mechanical properties than discontinuous fibers. However, out-of-plane deformation can be due to the angle of the steering [117], [118]. When placing tows in curved surfaces, the tow may separate from the tool or the composite substrate. In this case, shearing of the tow and the contact forces becomes significantly important [119]. However, if the angle of the roller or the force exerted on the roller was controlled, frictional forces may also be influenced. Studies show that

the processing parameters, such as temperature, pressure and federate, significantly affects the occurrence of wrinkling in composite tows. [120]. The effect of these parameters may be predicted through a finite element model. Therefore, to further study the topic of wrinkling, requires experiments regarding the friction of the NCFS and the composite prepreg. These involve inter-ply and intra-ply friction studies. This addition to the fabric model will allow for a stitching analysis which will give insight on any anomalies when combining the layers in the NCF.

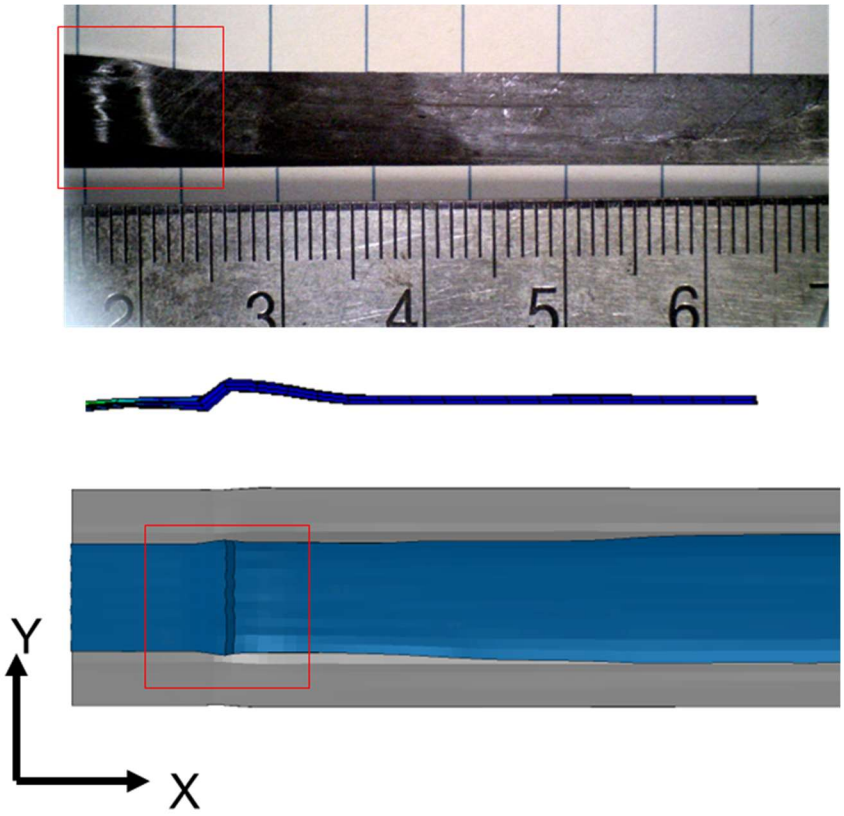

Figure 68. Wrinkling in a single composite tow and the with the same phenomenon showcased in the FEA model.

6.3 Flow regime switching and thermo-chemical expansion

The resin bleed out was a significant presence in the manufacturing of the thermoset laminates made deposited by AFP. This phenomenon was described by Wang and Gutowski [32] and later described further by Belnoue [72]. This mechanism suggests that during the compaction of a composite tow, tangled fibers cause the transverse flow of the resin to be hindered. Thus, causing a switch between a coupled squeeze flow and resin bleed out to just pure axial resin bleed out (Fig. 69). In other words, the ply becomes completely compressible since only the bleeding flow is present in state.

This switching mechanism would be dependent on the sample's cross section and would be derived phenomenologically like the other terms in the visco-hyperelastic model. Belnoue et al. [72] proposes that the strain dependent viscous terms can be used to switch these two flow regimes. After a critical cell-configuration is reached within the composite tow, the squeezing of the tow to resin bleed-out in a smooth transition. Furthermore, the effects of the ply interfaces due to the tooling may result in an uneven distribution of the shearing which decays towards the center of the tow. This results in two different mechanisms for locking to occur, the maximum through thickness strain rate and the maximum shear rate at the ply edges. These locking values were approximated as:

$$\varepsilon^{l} = \max\left\{ -ln\left(\sqrt{\frac{2}{3}\frac{h_0}{w_0} tan\left(\gamma_{lock} + 1\right)} \right), \frac{2}{3}\varepsilon_{lock} \right\} \tag{65}$$

Where γ_{lock} is the maximum shear at the ply edge which can be approximated using geometric considerations. It also interesting to consider the measurement of the fiber volume fraction in Fig.

57, the micrograph of the laminate depicts a shearing which results in higher fiber volume fraction closer to the edges of the gap. This shows the locking mechanism is present in the curing of the composite. Therefore, for later in the manufacturing cycle, past the first hold stage presented in the current study, this phenomenon is necessary to accurately predict the spreading of the composite tow and its effects on the filling of fiber tows gap, in terms of the uneven shearing of the ply.

The FEA model presented today may be extended to further encompass the full range of the composite manufacturing process. One of the simplest mechanisms to implement for the model revolves around the thermodynamic shrinkage of the composite [67]. After the development of the elastic modulus as the resin cures, the material will experience chemical and thermal shrinkages. This occurs later in the composite manufacturing process after the initial hold stage presented in the work. Both the composite tow with multiple gaps and the NCF fabric may experience a significant deformation due to the residual deformation due to large shift in fiber directions [53], [121].

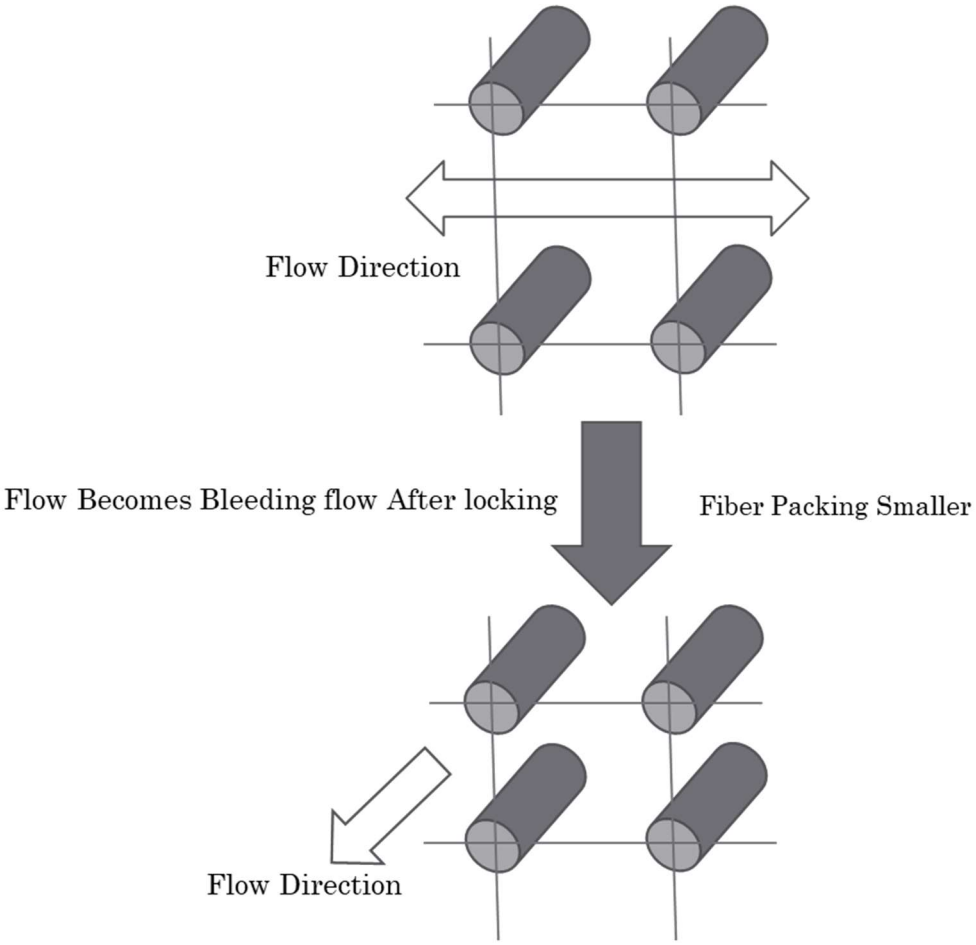

Figure 69. Schematics of the flow regime changed based on the packing of the fiber which demonstrates the purpose of the locking phenomenon in the fiber tow gap model.

6.4 Utilization of resultant morphology of the finite element models

The culmination of the FEA models is intended to be the morphology of the non-crimp fabric and the composite tow. These models can be further utilized to perform further analysis in terms of composites. With the resulting variation in fiber volume fraction and wrinkling, the results of the NCF simulation may be used to simulate the resin infusion through the layup. For example, in a rectangular sample shown in Fig. Figure 70, a flow front simulation can be performed with the stochastic features formed during the compaction and the relaxation of the composite. A simulation of the curing process with the resulting fiber volume fraction variation, voids content and initial

geometry of the sample can be performed using the models utilized in the work presented in this report.

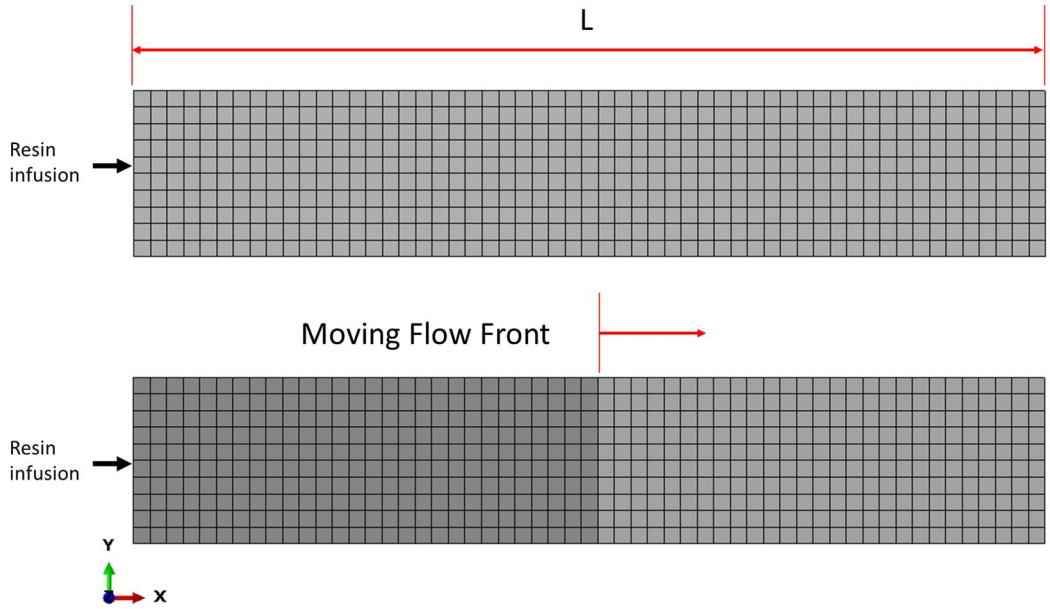

Figure 70. A reproduction of a 2D resin flow experiment using the calculated permeability.

A single-phase model was presented in this research. However, modelling the resin explicitly after the curing process presents a good model for the irregular morphology of a composite tow with embedded defects (Figure 71). Work has been done to accurately simulate the fiber tow gap with multiple defects [122]. Defects such as the resin rich region due to the composite gaps affects the quality of the composite [26], [28], [123], [124]. The strength of these laminates can be tested based on the resultant geometry due to the manufacturing process. This includes strength test, fatigue tests, and progressive failure analyses.

Furthermore, newer configuration of composite may be simulated using the modeling framework shown in this work. For example, the configuration which induces waviness and ply drop very similar to the model with multiple fiber tow gaps [51]. Increasing and decreasing the fiber to gap will also yield different results and different consideration when it comes to the resin

bleed out. Instead of a single-phase model, as presented in the fiber tow gap models, the resin bleed out may be simulated using formulas considering the Darcy flow through the fibers. This approach may be more computationally more expensive, but it would create a more generic approach when it comes to modeling the resin rich regions in composite structures. Furthermore, initial stochastic microscopic descriptors could be added to add variability to the model, such as initial fiber volume fraction and misalignment.

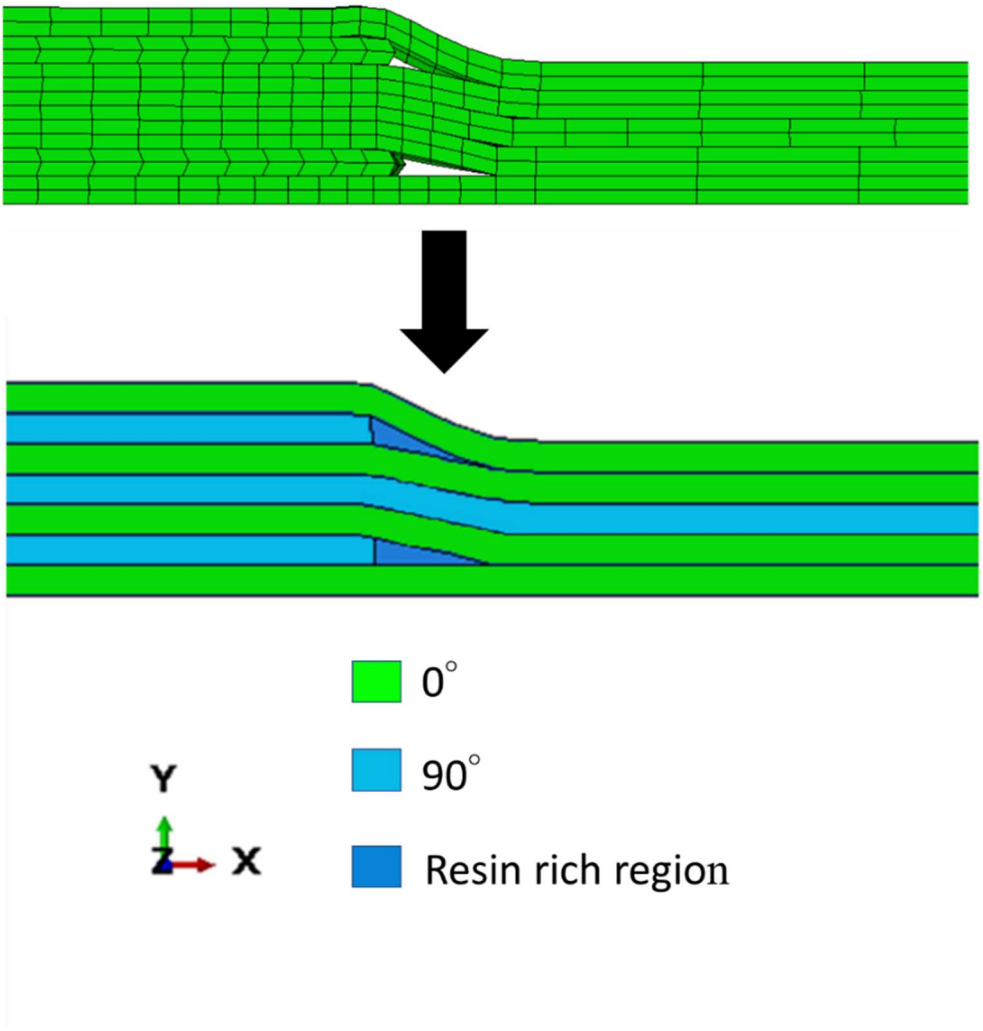

Figure 71. The aftermath of the composite curing model, which shows the resulting resin rich regions.

7 Appendix

Appendix A: Material Constants of the IM7/8663

Material constants used for the visco-hyperelastic properties of the transverse direction of the and the linear elastic fiber direction of the IM7/8852.

Hyperelastic Properties (Homogenized Composite)	
E_L	25 MPa
E_t	1e-6 MPa
G_{12}	0.495 E-7 MPa
ν_{12}	0.01
ν_{23}	0.01
G_{23}	1.0 MPa
λ	1.e-08 MPa
μ	2.5e-07 MPa
γ	3.1250 MPa
α	2.2277e-07 MPa
β	5.0005e-11 MPa
Fiber Properties (IM7 fibers)	
$E_L^{(f)}$	168 GPa
$\nu^{(f)}$	0.027
$\mu^{(f)}$	163 GPa
$\lambda^{(f)}$	7.65 Pa

8 References

[1] S. Vigneshwaran *et al.*, “Recent advancement in the natural fiber polymer composites: A comprehensive review,” *J. Clean. Prod.*, vol. 277, p. 124109, Dec. 2020, doi: 10.1016/j.jclepro.2020.124109.

[2] J. Frketic, T. Dickens, and S. Ramakrishnan, “Automated manufacturing and processing of fiber-reinforced polymer (FRP) composites: An additive review of contemporary and modern techniques for advanced materials manufacturing,” *Addit. Manuf.*, vol. 14, pp. 69–86, Mar. 2017, doi: 10.1016/j.addma.2017.01.003.

[3] P. Parandoush and D. Lin, “A review on additive manufacturing of polymer-fiber composites,” *Compos. Struct.*, vol. 182, pp. 36–53, Dec. 2017, doi: 10.1016/j.compstruct.2017.08.088.

[4] R. A. Tatara, “17 - Compression Molding,” in *Applied Plastics Engineering Handbook (Third Edition)*, M. Kutz, Ed., in Plastics Design Library. , William Andrew Publishing, 2024, pp. 389–424. doi: 10.1016/B978-0-323-88667-3.00011-4.

[5] K. M. Pillai, C. L. Tucker, and F. R. Phelan, “Numerical simulation of injection/compression liquid composite molding. Part 2: preform compression,” *Compos. Part Appl. Sci. Manuf.*, vol. 32, no. 2, pp. 207–220, Feb. 2001, doi: 10.1016/S1359-835X(00)00137-8.

[6] M. H. Nguyen, A. A. Vijayachandran, P. Davidson, D. Call, D. Lee, and A. M. Waas, “Effect of automated fiber placement (AFP) manufacturing signature on mechanical performance of composite structures,” *Compos. Struct.*, vol. 228, p. 111335, Nov. 2019, doi: 10.1016/j.compstruct.2019.111335.

[7] M. H. Nguyen, P. Davidson, and A. M. Waas, “Influence of Automated Fiber Placement (AFP) Manufacturing Signature on the Mechanical Performance of a Composite,” in *AIAA Scitech 2020 Forum*. Accessed: Mar. 11, 2020. [Online]. Available: https://arc.aiaa.org/doi/abs/10.2514/6.2020-0473

[8] M. A. Siddiqui, H. Koelman, and P. S. Shembekar, “High Pressure RTM Process Modeling for Automotive Composite Product Development,” SAE International, Warrendale, PA, SAE Technical Paper 2017-26–0175, Jan. 2017. doi: 10.4271/2017-26-0175.

[9] A. Beltran Laredo, “Mechanism of Compaction with Wrinkle Formation During Automatic Stitching of Dry Fabrics and the Size Effect of Compression Molded Discontinuous Fiber-Reinforced Composites,” *Mech. Aerosp. Eng. Theses Diss.*, Aug. 2020, doi: 10.25777/e2bb-b036.

[10] V. Jamora, B. Laredo, and O. Kravchenko, “Modeling of Wrinkle Formation in Non-Crimp Dry Fabric during Preform Compaction”.

[11] Y. Geng, J. Jiang, and N. Chen, “Local impregnation behavior and simulation of non-crimp fabric on curved plates in vacuum assisted resin transfer molding,” *Compos. Struct.*, vol. 208, pp. 517–524, Jan. 2019, doi: 10.1016/j.compstruct.2018.10.054.

[12] “Handbook of Technical Textiles - 2nd Edition.” Accessed: Oct. 05, 2022. [Online]. Available: https://www.elsevier.com/books/handbook-of-technical-textiles/horrocks/978-1-78242-465-9

[13] P. K. Mallick, *Processing of Polymer Matrix Composites*. New York: CRC Press, 2017. doi: 10.1201/9781315157252.

[14] D. H.-J. A. Lukaszewicz, C. Ward, and K. D. Potter, “The engineering aspects of automated prepreg layup: History, present and future,” *Compos. Part B Eng.*, vol. 43, no. 3, Art. no. 3, Apr. 2012, doi: 10.1016/j.compositesb.2011.12.003.
[15] K. Wu, B. Stewart, and R. Martin, *ISAAC – A Testbed for Advanced Composites Research*. 2014.
[16] D. M. J. Peeters, G. G. Lozano, and M. M. Abdalla, “Effect of steering limit constraints on the performance of variable stiffness laminates,” *Comput. Struct.*, vol. 196, pp. 94–111, Feb. 2018, doi: 10.1016/j.compstruc.2017.11.002.
[17] K. C. Wu, “Design and analysis of tow-steered composite shells using fiber placement,” 2008.
[18] B. Denkena, C. Schmidt, and P. Weber, “Automated Fiber Placement Head for Manufacturing of Innovative Aerospace Stiffening Structures,” *Procedia Manuf.*, vol. 6, pp. 96–104, Jan. 2016, doi: 10.1016/j.promfg.2016.11.013.
[19] E. D. Gregory and P. D. Juarez, “In-situ thermography of automated fiber placement parts,” *AIP Conf. Proc.*, vol. 1949, no. 1, p. 060005, Apr. 2018, doi: 10.1063/1.5031551.
[20] Y.-N. Liu, C. Yuan, C. Liu, J. Pan, and Q. Dong, “Study on the resin infusion process based on automated fiber placement fabricated dry fiber preform,” *Sci. Rep.*, vol. 9, May 2019, doi: 10.1038/s41598-019-43982-1.
[21] V. C. C. Jamora, V. M. Rauch, S. Kravchenko, and O. Kravchenko, “Mechanics of Fiber Tow Compaction for Predicting Defect Morphology in AFP composites,” in *AIAA SCITECH 2022 Forum*, American Institute of Aeronautics and Astronautics. doi: 10.2514/6.2022-0378.
[22] K. Croft, L. Lessard, D. Pasini, M. Hojjati, J. Chen, and A. Yousefpour, “Experimental study of the effect of automated fiber placement induced defects on performance of composite laminates,” *Compos. Part Appl. Sci. Manuf.*, vol. 42, no. 5, Art. no. 5, May 2011, doi: 10.1016/j.compositesa.2011.01.007.
[23] M. H. Nguyen, A. A. Vijayachandran, P. Davidson, D. Call, D. Lee, and A. M. Waas, “Effect of automated fiber placement (AFP) manufacturing signature on mechanical performance of composite structures,” *Compos. Struct.*, vol. 228, p. 111335, Nov. 2019, doi: 10.1016/j.compstruct.2019.111335.
[24] A. Trochez, V. C. Jamora, R. Larson, K. C. Wu, D. Ghosh, and O. G. Kravchenko, “Effects of automated fiber placement defects on high strain rate compressive response in advanced thermosetting composites,” *J. Compos. Mater.*, vol. 55, no. 30, pp. 4549–4562, Dec. 2021, doi: 10.1177/00219983211042073.
[25] K. Croft, L. Lessard, D. Pasini, M. Hojjati, J. Chen, and A. Yousefpour, “Experimental study of the effect of automated fiber placement induced defects on performance of composite laminates,” *Compos. Part Appl. Sci. Manuf.*, vol. 42, no. 5, Art. no. 5, May 2011, doi: 10.1016/j.compositesa.2011.01.007.
[26] M. Ghayour, M. Hojjati, and R. Ganesan, “Effect of tow gaps on impact strength of thin composite laminates made by Automated Fiber Placement: Experimental and semi-analytical approaches,” *Compos. Struct.*, vol. 248, p. 112536, Sep. 2020, doi: 10.1016/j.compstruct.2020.112536.
[27] M. Nartey *et al.*, “Understanding the impact of fibre wrinkle architectures on composite laminates through tailored gaps and overlaps,” *Compos. Part B Eng.*, vol. 196, p. 108097, Sep. 2020, doi: 10.1016/j.compositesb.2020.108097.

[28] A. Trochez, V. C. Jamora, R. Larson, K. C. Wu, D. Ghosh, and O. G. Kravchenko, “Effects of automated fiber placement defects on high strain rate compressive response in advanced thermosetting composites,” *J. Compos. Mater.*, p. 00219983211042073, Sep. 2021, doi: 10.1177/00219983211042073.
[29] Y. M. Elsherbini and S. V. Hoa, “Experimental and numerical investigation of the effect of gaps on fatigue behavior of unidirectional carbon/epoxy automated fiber placement laminates,” *J. Compos. Mater.*, vol. 51, no. 6, pp. 759–772, Mar. 2017, doi: 10.1177/0021998316655393.
[30] W. Zhou, Q. Cheng, Q. Xu, W. Zhu, and Y. Ke, “Deformation and fracture mechanisms of automated fiber placement pre-preg laminates under out-of-plane tensile loading,” *Compos. Struct.*, vol. 255, p. 112948, Jan. 2021, doi: 10.1016/j.compstruct.2020.112948.
[31] Y. Hu *et al.*, “Modeling the effect of automated fiber placement induced gaps based on serial layer scanned point clouds,” *Compos. Struct.*, vol. 313, p. 116929, Jun. 2023, doi: 10.1016/j.compstruct.2023.116929.
[32] E. L. Wang and T. G. Gutowski, “Laps and gaps in thermoplastic composites processing,” *Compos. Manuf.*, vol. 2, no. 2, pp. 69–78, Jan. 1991, doi: 10.1016/0956-7143(91)90182-G.
[33] A. Sawicki and P. Minguett, “The effect of intraply overlaps and gaps upon the compression strength of composite laminates,” in *39th AIAA/ASME/ASCE/AHS/ASC Structures, Structural Dynamics, and Materials Conference and Exhibit*, American Institute of Aeronautics and Astronautics, 2020. doi: 10.2514/6.1998-1786.
[34] W. E. Guin, J. R. Jackson, and C. M. Bosley, “Effects of tow-to-tow gaps in composite laminates fabricated via automated fiber placement,” *Compos. Part Appl. Sci. Manuf.*, vol. 115, pp. 66–75, Dec. 2018, doi: 10.1016/j.compositesa.2018.09.014.
[35] M. Thor *et al.*, “Numerical and experimental investigation of out-of-plane fiber waviness on the mechanical properties of composite materials,” *Int. J. Mater. Form.*, vol. 14, no. 1, pp. 19–37, Jan. 2021, doi: 10.1007/s12289-020-01540-5.
[36] G. Seon, Y. Nikishkov, A. Makeev, and L. Fergusson, “Predicting Formation of Manufacturing Defects in Contoured Composites,” Oct. 2019, Accessed: Mar. 11, 2020. [Online]. Available: https://www.ingentaconnect.com/content/ahs/jahs/2019/00000064/00000004/art00005
[37] E. S. Greenhalgh, Ed., “7 - Defects and damage and their role in the failure of polymer composites,” in *Failure Analysis and Fractography of Polymer Composites*, in Woodhead Publishing Series in Composites Science and Engineering. , Woodhead Publishing, 2009, pp. 356–440. doi: 10.1533/9781845696818.356.
[38] D. S. Cairns, J. F. Mandell, M. E. Scott, and J. Z. Maccagnano, “Design and manufacturing considerations for ply drops in composite structures,” *Compos. Part B Eng.*, vol. 30, no. 5, pp. 523–534, Jul. 1999, doi: 10.1016/S1359-8368(98)00043-2.
[39] J. Wang, K. D. Potter, and J. Etches, “Experimental investigation and characterisation techniques of compressive fatigue failure of composites with fibre waviness at ply drops,” *Compos. Struct.*, vol. 100, pp. 398–403, Jun. 2013, doi: 10.1016/j.compstruct.2013.01.010.
[40] P. Hubert, A. Johnston, A. Poursartip, and K. Nelson, “Cure kinetics and viscosity models for Hexcel 8552 epoxy resin,” *Int SAMPE Symp Exhib.*, vol. 46, pp. 2341–2354, Jan. 2001.
[41] S. J. Ng, R. Boswell, S. J. Claus, F. Arnold, and A. Vizzini, “Degree of Cure, Heat of Reaction, and Viscosity of 8552 and 977-3 HM Epoxy Resin,” NAVAL AIR WARFARE CENTER AIRCRAFT DIV PATUXENT RIVER MD, Mar. 2000. Accessed: Apr. 01, 2021. [Online]. Available: https://apps.dtic.mil/sti/citations/ADA377439

[42] Y. Wang, S. Mahapatra, J. P.-H. Belnoue, D. S. Ivanov, and S. R. Hallett, “Understanding tack behaviour during prepreg-based composites’ processing,” *Compos. Part Appl. Sci. Manuf.*, vol. 164, p. 107284, Jan. 2023, doi: 10.1016/j.compositesa.2022.107284.
[43] X. He, Y. Shi, C. Kang, and T. Yu, “Analysis and control of the compaction force in the composite prepreg tape winding process for rocket motor nozzles,” *Chin. J. Aeronaut.*, vol. 30, no. 2, pp. 836–845, Apr. 2017, doi: 10.1016/j.cja.2016.07.004.
[44] F. Heinecke and C. Willberg, “Manufacturing-Induced Imperfections in Composite Parts Manufactured via Automated Fiber Placement,” *J. Compos. Sci.*, vol. 3, Jun. 2019, doi: 10.3390/jcs3020056.
[45] D. Budelmann, H. Detampel, C. Schmidt, and D. Meiners, “Interaction of process parameters and material properties with regard to prepreg tack in automated lay-up and draping processes,” *Compos. Part Appl. Sci. Manuf.*, vol. 117, pp. 308–316, Feb. 2019, doi: 10.1016/j.compositesa.2018.12.001.
[46] A. W. Smith, A. Endruweit, G. Y. H. Choong, D. S. A. De Focatiis, and P. Hubert, “Adaptation of material deposition parameters to account for out-time effects on prepreg tack,” *Compos. Part Appl. Sci. Manuf.*, vol. 133, p. 105835, Jun. 2020, doi: 10.1016/j.compositesa.2020.105835.
[47] P. Zhu, T. Zheng, T. Hu, J. Hu, and J. Zhang, “Contact Mechanics Response of Composite Cylindrical Roller Bearings Based on FEM,” *J. Fail. Anal. Prev.*, vol. 21, no. 2, pp. 499–506, Apr. 2021, doi: 10.1007/s11668-020-01106-2.
[48] E. Oromiehie, B. G. Prusty, P. Compston, and G. Rajan, “Automated fibre placement based composite structures: Review on the defects, impacts and inspections techniques,” *Compos. Struct.*, vol. 224, p. 110987, Sep. 2019, doi: 10.1016/j.compstruct.2019.110987.
[49] S. H., G. D., D. A., and S. H., “Effect of Process Parameters on The Quality of Laminates Made by Automated Fiber Placement (AFP) Using Out-Of-Autoclave (OOA) Prepregs,” presented at the European Conference on Composite Materials, Jun. 2016.
[50] M. Thor *et al.*, “Numerical and experimental investigation of out-of-plane fiber waviness on the mechanical properties of composite materials,” *Int. J. Mater. Form.*, Jan. 2020, doi: 10.1007/s12289-020-01540-5.
[51] P. Díaz-Montiel, G. G. Ayala, A. Rivera, R. Mauk, C. Reiman, and S. Venkataraman, “Quantification of Material and Geometric Defects Variability in Fiber-Reinforced Composites with Ply Waviness Defects,” in *ASME 2023*, Jun. 2023.
[52] V. Jamora, “Compaction and Residual Stress Modeling in Composite Manufactured with Automated Fiber Placement,” *Mech. Aerosp. Eng. Theses Diss.*, Apr. 2020, doi: 10.25777/j2pk-ke03.
[53] V. C. Jamora, K. C. Wu, and O. G. Kravchenko, “Residual deformation analysis in composite shell structures manufactured using automated fiber placement,” *Compos. Struct.*, vol. 248, p. 112482, Sep. 2020, doi: 10.1016/j.compstruct.2020.112482.
[54] V. A. F. Costa and A. C. M. Sousa, “Modeling of flow and thermo-kinetics during the cure of thick laminated composites,” *Int. J. Therm. Sci.*, vol. 42, no. 1, Art. no. 1, Jan. 2003, doi: 10.1016/S1290-0729(02)00003-0.
[55] J. P.-H. Belnoue *et al.*, “Understanding and predicting defect formation in automated fibre placement pre-preg laminates,” *Compos. Part Appl. Sci. Manuf.*, vol. 102, pp. 196–206, Nov. 2017, doi: 10.1016/j.compositesa.2017.08.008.

[56] R. B. Pipes, “Anisotropic Viscosities of an Oriented Fiber Composite with a Power-Law Matrix,” *J. Compos. Mater.*, vol. 26, no. 10, pp. 1536–1552, Oct. 1992, doi: 10.1177/002199839202601009.
[57] S. David Müzel, E. P. Bonhin, N. M. Guimarães, and E. S. Guidi, “Application of the Finite Element Method in the Analysis of Composite Materials: A Review,” *Polymers*, vol. 12, no. 4, Art. no. 4, Apr. 2020, doi: 10.3390/polym12040818.
[58] B. Daum, N. Feld, O. Allix, and R. Rolfes, “A review of computational modelling approaches to compressive failure in laminates,” *Compos. Sci. Technol.*, vol. 181, p. 107663, Sep. 2019, doi: 10.1016/j.compscitech.2019.05.020.
[59] S. Yan, X. Zou, M. Ilkhani, and A. Jones, “An efficient multiscale surrogate modelling framework for composite materials considering progressive damage based on artificial neural networks,” *Compos. Part B Eng.*, vol. 194, p. 108014, Aug. 2020, doi: 10.1016/j.compositesb.2020.108014.
[60] D. O. Adams and S. J. Bell, “Compression strength reductions in composite laminates due to multiple-layer waviness,” *Mesostructures Mesomech. Fibre Compos.*, vol. 53, no. 2, Art. no. 2, Jan. 1995, doi: 10.1016/0266-3538(95)00020-8.
[61] S. C. White, P. M. Weaver, and K. C. Wu, “Post-buckling analyses of variable-stiffness composite cylinders in axial compression,” *Compos. Struct.*, vol. 123, pp. 190–203, May 2015, doi: 10.1016/j.compstruct.2014.12.013.
[62] A. Beakou, M. Cano, J.-B. Le Cam, and V. Verney, “Modelling slit tape buckling during automated prepreg manufacturing: A local approach,” *Compos. Struct.*, vol. 93, no. 10, Art. no. 10, Sep. 2011, doi: 10.1016/j.compstruct.2011.04.030.
[63] F. A. Leone, C. G. Dávila, and D. Girolamo, “Progressive damage analysis as a design tool for composite bonded joints,” *Compos. Part B Eng.*, vol. 77, pp. 474–483, Aug. 2015, doi: 10.1016/j.compositesb.2015.03.046.
[64] S. Sattar, “Role of Structural Hierarchy in Multiscale Material Systems,” *Mech. Aerosp. Eng. Theses Diss.*, Aug. 2022, doi: 10.25777/xh7r-g449.
[65] S. Sattar, D. Pedrazzoli, M. Zhang, S. G. Kravchenko, and O. G. Kravchenko, “Notched tensile strength of long discontinuous glass fiber reinforced nylon composite,” *Compos. Part Appl. Sci. Manuf.*, vol. 163, p. 107217, Dec. 2022, doi: 10.1016/j.compositesa.2022.107217.
[66] V. Jamora, C. Wu, and A. Kravchenko, “Residual deformation analysis in composite shell structures manufactured using automated fiber placement,” Accessed: Jul. 04, 2024. [Online]. Available: https://ntrs.nasa.gov/citations/20205005869
[67] O. G. Kravchenko, S. G. Kravchenko, and R. B. Pipes, “Chemical and thermal shrinkage in thermosetting prepreg,” *Compos. Part Appl. Sci. Manuf.*, vol. 80, pp. 72–81, Jan. 2016, doi: 10.1016/j.compositesa.2015.10.001.
[68] N. Ersoy, K. Potter, M. R. Wisnom, and M. J. Clegg, “An experimental method to study the frictional processes during composites manufacturing,” *Compos. Part Appl. Sci. Manuf.*, vol. 36, no. 11, pp. 1536–1544, Nov. 2005, doi: 10.1016/j.compositesa.2005.02.010.
[69] J. I. Kim, Y. T. Hwang, K. H. Choi, H. J. Kim, and H. S. Kim, “Prediction of the vacuum assisted resin transfer molding (VARTM) process considering the directional permeability of sheared woven fabric,” *Compos. Struct.*, vol. 211, pp. 236–243, Mar. 2019, doi: 10.1016/j.compstruct.2018.12.043.
[70] T. G. Rogers and J. O’neill, “Theoretical analysis of forming flows of fibre-reinforced composites,” 1991, doi: 10.1016/0956-7143(91)90134-3.

[71] J. Bonet and A. J. Burton, “A simple orthotropic, transversely isotropic hyperelastic constitutive equation for large strain computations,” *Comput. Methods Appl. Mech. Eng.*, vol. 162, no. 1, Art. no. 1, Aug. 1998, doi: 10.1016/S0045-7825(97)00339-3.
[72] J. P.-H. Belnoue, O. J. Nixon-Pearson, D. Ivanov, and S. R. Hallett, “A novel hyper-viscoelastic model for consolidation of toughened prepregs under processing conditions,” *Mech. Mater.*, vol. 97, pp. 118–134, Jun. 2016, doi: 10.1016/j.mechmat.2016.02.019.
[73] G. Seon, Y. Nikishkov, and A. Makeev, “A numerical method based on pore-pressure cohesive zone modeling for simulation of debulking in resin-saturated composite prepregs,” *Int. J. Numer. Methods Eng.*, vol. 123, no. 12, pp. 2791–2813, 2022, doi: 10.1002/nme.6959.
[74] P. Simacek, N. Niknafs Kermani, V. Gargitter, and S. G. Advani, “Role of resin percolation in gap filling mechanisms during the thin ply thermosetting automated tape placement process,” *Compos. Part Appl. Sci. Manuf.*, vol. 152, p. 106677, Jan. 2022, doi: 10.1016/j.compositesa.2021.106677.
[75] N. Niknafs Kermani, V. Gargitter, P. Simacek, and S. G. Advani, “Gap filling mechanisms during the thin ply Automated Tape Placement process,” *Compos. Part Appl. Sci. Manuf.*, vol. 147, p. 106454, Aug. 2021, doi: 10.1016/j.compositesa.2021.106454.
[76] P. A. Kelly, “A viscoelastic model for the compaction of fibrous materials,” *J. Text. Inst.*, vol. 102, no. 8, pp. 689–699, Aug. 2011, doi: 10.1080/00405000.2010.515103.
[77] G. Limbert and J. Middleton, “A transversely isotropic viscohyperelastic material: Application to the modeling of biological soft connective tissues,” *Int. J. Solids Struct.*, vol. 41, no. 15, Art. no. 15, Jul. 2004, doi: 10.1016/j.ijsolstr.2004.02.057.
[78] T. He, H. Zhang, and K. Zhang, “A smoothed finite element approach for computational fluid dynamics: applications to incompressible flows and fluid–structure interaction,” *Comput. Mech.*, vol. 62, no. 5, pp. 1037–1057, Nov. 2018, doi: 10.1007/s00466-018-1549-x.
[79] M. N. Saquib, R. Larson, S. Sattar, J. Li, S. Kravchenko, and O. Kravchenko, “Experimental Validation of Reconstructed Microstructure via Deep Learning in Discontinuous Fiber Platelet Composite,” *J. Appl. Mech.*, pp. 1–61, Nov. 2023, doi: 10.1115/1.4063983.
[80] R. Larson, R. Horque, V. C. Jamora, J. Li, S. G. Kravchenko, and O. G. Kravchenko, “Prediction of Local Fiber Orientation State in Prepreg Platelet Molded Composites via Deep Convolutional Neural Network,” *Submitt. Compos. Part A*.
[81] R. A. Larson, R. Hoque, V. Jamora, J. Li, S. Kravchenko, and O. Kravchenko, “Hyperparameters Effect in Deep Convolutional Neural Network Model on Prediction of Fiber Orientation Distribution in Prepreg Platelet Molded Composites,” in *AIAA SCITECH 2022 Forum*, 0 vols., in AIAA SciTech Forum. , American Institute of Aeronautics and Astronautics, 2021. doi: 10.2514/6.2022-0103.
[82] T. J. Chapman, J. W. Gillespie, R. B. Pipes, J.-A. E. Manson, and J. C. Seferis, “Prediction of Process-Induced Residual Stresses in Thermoplastic Composites,” *J. Compos. Mater.*, vol. 24, no. 6, Art. no. 6, Jun. 1990, doi: 10.1177/002199839002400603.
[83] P. Hubert, A. Johnston, A. Poursartip, and K. Nelson, “Cure kinetics and viscosity models for Hexcel 8552 epoxy resin,” *Int SAMPE Symp Exhib.*, vol. 46, pp. 2341–2354, Jan. 2001.
[84] “Stress and Strain,” in *Formulas for Stress, Strain, and Structural Matrices*, John Wiley & Sons, Ltd, 2004, pp. 89–147. doi: 10.1002/9780470172681.ch3.

[85] M. J. A. Latif, D. Peric, and W. G. Dettmer, “Numerical Modeling of Transversely Isotropic Elastic Material at Small and Finite Strains,” *AIP Conf. Proc.*, vol. 909, no. 1, Art. no. 1, May 2007, doi: 10.1063/1.2739841.
[86] A. J. Favaloro, D. E. Sommer, B. R. Denos, and R. B. Pipes, “Simulation of prepreg platelet compression molding: Method and orientation validation,” *J. Rheol.*, vol. 62, no. 6, pp. 1443–1455, Oct. 2018, doi: 10.1122/1.5044533.
[87] R. Li and D. Zhang, “An experimentally validated anisotropic visco-hyperelastic constitutive model for knitted fabric-reinforced elastomer composites,” *J. Reinf. Plast. Compos.*, p. 07316844231198310, Sep. 2023, doi: 10.1177/07316844231198310.
[88] J. Cao *et al.*, “Characterization of mechanical behavior of woven fabrics: Experimental methods and benchmark results,” *Compos. Part Appl. Sci. Manuf.*, vol. 39, no. 6, pp. 1037–1053, Jun. 2008, doi: 10.1016/j.compositesa.2008.02.016.
[89] P. Hubert and A. Poursartip, “A Review of Flow and Compaction Modelling Relevant to Thermoset Matrix Laminate Processing,” *J. Reinf. Plast. Compos.*, vol. 17, no. 4, pp. 286–318, Mar. 1998, doi: 10.1177/073168449801700402.
[90] J. P.-H. Belnoue, O. Nixon-Pearson, D. Ivanov, and S. R. Hallet, “Numerical and Experimental Investigation of Prepreg Compaction for Defect Formation Mechanisms,” *Des. Manuf. Appl. Compos. 2014*, vol. 0, no. 0, Art. no. 0, 2014, Accessed: Aug. 10, 2023. [Online]. Available: https://dpi-proceedings.com/index.php/dmac2014/article/view/21306
[91] M. E. Messiry, “Theoretical analysis of natural fiber volume fraction of reinforced composites,” *Alex. Eng. J.*, vol. 52, no. 3, pp. 301–306, Sep. 2013, doi: 10.1016/j.aej.2013.01.006.
[92] A. Ghosh, S. M. Ishtiaque, and R. S. Rengasamy, “Stress–strain characteristics of different spun yarns as a function of strain rate and gauge length,” *J. Text. Inst.*, vol. 96, no. 2, pp. 99–104, Mar. 2005, doi: 10.1533/joti.2004.0067.
[93] “ZOLTEK™ PX35 Multi-Directional Fabrics.” [Online]. Available: https://zoltek.com/wp-content/uploads/2017/09/TDS_PX35_MD_Fabrics.pdf
[94] P. Kelly, R. Umer, and S. Bickerton, “Compaction of dry and wet fibrous materials during infusion processes,” presented at the 36th international SAMPE technical conference, 2004, pp. 785–797.
[95] A. A. Somashekar, S. Bickerton, and D. Bhattacharyya, “Non-elastic effects during compression of fiber reinforcements,” in *International Conference on Flow Processes in Composite Materials, FPCM*, 2004, pp. 413–418.
[96] B. Bhattacharjee, C. Sherin, K. Kaipa, O. Kravchenko, S. Dong, and V. Jamora, “FIBER TOW SPREADING DURING AFP MANUFACTURING,” in *SAMPE 2023*, NA SAMPE, 2023. doi: 10.33599/nasampe/s.23.0186.
[97] V. C. Jamora, V. Rauch, S. G. Kravchenko, and O. G. Kravchenko, “Effect of Resin Bleed Out on Compaction Behavior of the Fiber Tow Gap Region during Automated Fiber Placement Manufacturing,” *Polymers*, vol. 16, no. 1, Art. no. 1, Jan. 2024, doi: 10.3390/polym16010031.
[98] V. C. C. Jamora, V. M. Rauch, S. Kravchenko, and O. Kravchenko, “Mechanics of Fiber Tow Compaction for Predicting Defect Morphology in AFP composites,” in *AIAA SCITECH 2022 Forum*, 0 vols., in AIAA SciTech Forum. , American Institute of Aeronautics and Astronautics, 2021. doi: 10.2514/6.2022-0378.

[99] X. Li, S. R. Hallett, and M. R. Wisnom, “Modelling the effect of gaps and overlaps in automated fibre placement (AFP)-manufactured laminates,” *Sci. Eng. Compos. Mater.*, vol. 22, no. 2, pp. 115–129, 2015, doi: 10.1515/secm-2013-0322.
[100] V. C. Jamora, “Modeling and characterization of the effects of percolation flow in composites with an embedded fiber tow gap”.
[101] J. M. Kenny, A. Apicella, and L. Nicolais, “A model for the thermal and chemorheological behavior of thermosets. I: Processing of epoxy-based composites,” *Polym. Eng. Sci.*, vol. 29, no. 15, Art. no. 15, Aug. 1989, doi: 10.1002/pen.760291502.
[102] S. M. Sabzevari, “Cure kinetics and process modeling of a carbon-fiber thermoplastic-toughened epoxy resin prepreg,” p. 119.
[103] V. A. F. Costa and A. C. M. Sousa, “Modeling of flow and thermo-kinetics during the cure of thick laminated composites,” *Int. J. Therm. Sci.*, vol. 42, no. 1, Art. no. 1, Jan. 2003, doi: 10.1016/S1290-0729(02)00003-0.
[104] O. Falcó, J. A. Mayugo, C. S. Lopes, N. Gascons, and J. Costa, “Variable-stiffness composite panels: Defect tolerance under in-plane tensile loading,” *Compos. Part Appl. Sci. Manuf.*, vol. 63, pp. 21–31, Aug. 2014, doi: 10.1016/j.compositesa.2014.03.022.
[105] H. C. Stadtfeld, M. Erninger, S. Bickerton, and S. G. Advani, “An Experimental Method to Continuously Measure Permeability of Fiber Preforms as a Function of Fiber Volume Fraction,” *J. Reinf. Plast. Compos.*, vol. 21, no. 11, pp. 879–899, Jul. 2002, doi: 10.1177/073168440202101102.
[106] K. Marlett, Y. Ng, and J. Tomblin, “Hexcel 8552 IM7 unidirectional prepreg 190 gsm & 35% RC qualification material property data report,” *Natl. Cent. Adv. Mater. Perform. Wichita Kans. Test Rep. CAM-RP-2009-015 Rev A*, pp. 1–238, 2011.
[107] R. Larson, A. Bergan, F. Leone, and O. G. Kravchenko, “Influence of stochastic adhesive porosity and material variability on failure behavior of adhesively bonded composite sandwich joints,” *Compos. Struct.*, vol. 306, p. 116608, Feb. 2023, doi: 10.1016/j.compstruct.2022.116608.
[108] T. Yamada and M. Matsuo, “The Study of Effect of a Polyurethane Filament on Mechanical Properties of Plain Stitch Fabrics,” *Text. Res. J.*, vol. 79, no. 4, pp. 310–317, Mar. 2009, doi: 10.1177/0040517508090501.
[109] S. Bickerton, M. J. Buntain, and A. A. Somashekar, “The viscoelastic compression behavior of liquid composite molding preforms,” *Compos. Part Appl. Sci. Manuf.*, vol. 34, no. 5, pp. 431–444, May 2003, doi: 10.1016/S1359-835X(03)00088-5.
[110] A. A. Somashekar, S. Bickerton, and D. Bhattacharyya, “Modelling the viscoelastic stress relaxation of glass fibre reinforcements under constant compaction strain during composites manufacturing,” *Compos. Part Appl. Sci. Manuf.*, vol. 43, no. 7, pp. 1044–1052, Jul. 2012, doi: 10.1016/j.compositesa.2012.02.004.
[111]H. Xia, M. Song, Z. Zhang, and M. Richardson, “Microphase separation, stress relaxation, and creep behavior of polyurethane nanocomposites,” *J. Appl. Polym. Sci.*, vol. 103, no. 5, pp. 2992–3002, 2007, doi: 10.1002/app.25462.
[112] H. L. Ornaghi, J. H. S. Almeida, F. M. Monticeli, and R. M. Neves, “Stress relaxation, creep, and recovery of carbon fiber non-crimp fabric composites,” *Compos. Part C Open Access*, vol. 3, p. 100051, Nov. 2020, doi: 10.1016/j.jcomc.2020.100051.
[113] Y. R. Kim, S. P. McCarthy, and J. P. Fanucci, “Compressibility and relaxation of fiber reinforcements during composite processing,” *Polym. Compos.*, vol. 12, no. 1, pp. 13–19, 1991, doi: 10.1002/pc.750120104.

[114] K. Van der Voort Maarschalk, K. Zuurman, H. Vromans, G. K. Bolhuis, and C. F. Lerk, "Stress relaxation of compacts produced from viscoelastic materials," *Int. J. Pharm.*, vol. 151, no. 1, pp. 27–34, May 1997, doi: 10.1016/S0378-5173(97)04889-8.
[115] J. V. Viisainen and M. P. F. Sutcliffe, "Characterising the variability in wrinkling during the preforming of non-crimp fabrics," *Compos. Part Appl. Sci. Manuf.*, vol. 149, p. 106536, Oct. 2021, doi: 10.1016/j.compositesa.2021.106536.
[116] S. Bel, P. Boisse, and F. Dumont, "Analyses of the Deformation Mechanisms of Non-Crimp Fabric Composite Reinforcements during Preforming," *Appl. Compos. Mater.*, vol. 19, no. 3, pp. 513–528, Jun. 2012, doi: 10.1007/s10443-011-9207-x.
[117] O. Falcó Salcines, "Analysis of process-induced defects on steered-fiber panels for aeronautical applications," Universitat de Girona, 2014.
[118] P. Boisse, J. Colmars, N. Hamila, N. Naouar, and Q. Steer, "Bending and wrinkling of composite fiber preforms and prepregs. A review and new developments in the draping simulations," *Compos. Part B Eng.*, vol. 141, pp. 234–249, May 2018, doi: 10.1016/j.compositesb.2017.12.061.
[119] N. Bakhshi and M. Hojjati, "An experimental and simulative study on the defects appeared during tow steering in automated fiber placement," *Compos. Part Appl. Sci. Manuf.*, vol. 113, pp. 122–131, Oct. 2018, doi: 10.1016/j.compositesa.2018.07.031.
[120] R. Wehbe, C. Sacco, A. Baz Radwan, M. Albazzan, and R. Harik, "Influence of process parameters in AFP fiber steering on cylinders: Constant curvature paths," *Compos. Part C Open Access*, vol. 2, p. 100036, Oct. 2020, doi: 10.1016/j.jcomc.2020.100036.
[121] V. C. Jamora, K. C. Wu, and O. G. Kravchenko, "Residual deformation analysis in composite shell structures manufactured using automated fiber placement," *Compos. Struct.*, vol. 248, p. 112482, Sep. 2020, doi: 10.1016/j.compstruct.2020.112482.
[122] A. Ravangard, V. C. Jamora, J. D. Bhagatji, and O. Kravchenko, "Origin and Significance of Non-Uniform Morphology in AFP Composites," *Proc. Am. Soc. Compos.-THIRTY-EIGHTH Tech. Conf.*, no. 0, Art. no. 0, 2023, doi: 10.12783/asc38/36629.
[123] I. A. Khattab, "A novel numerical approach and experimental study on the waviness defects in composite structures," *DLR Dtsch. Zent. Luft- Raumfahrt EV - Forschungsberichte*, pp. 1–242, Jan. 2013.
[124] B. C. (Eric) Kim, K. Hazra, P. Weaver, and K. Potter, "Limitations of fibre placement techniques for variable angle tow composites and their process-induced defects," *18th Int. Conf. Compos. Mater.*, Aug. 2011, [Online]. Available: http://www.scopus.com/inward/record.url?scp=84875940309&partnerID=8YFLogxK

JAMORA, VON CLYDE C

1429 Thamesford Dr. | Virginia Beach, VA, 23464 |
EMAIL: vonjamora@gmail.com |

EDUCATION

Old Dominion University

PhD in Mechanical Engineering — **AUG** 2020 - PRESENT
Master's Degree in Mechanical Engineering — **SEP** 2018 - **MAY** 2020
Bachelor's Degree in Mechanical Engineering — **JAN** 2015 - **MAY** 2018
Cumulative GPA: 3.85

Tidewater Community College — **AUG** 2013 - **DEC** 2015

Associates Degree in Mechanical Engineering
GPA: 3.939

Landstown High School Governor's STEM and Technology Academy — **SEP** 2009 - J**UN** 2013
Graduated Technology Academy with Honors

Research and Work Experience

Collier Aerospace — **AUG** 2023 – PRESENT
Aerospace Composites Research Engineer
Newport News, Virginia

Graduate Teaching Assistant — **AUG** 2020 – **MAY** 2023
Graduate Researcher — **SEP** 2018 – **MAY** 2023
Old Dominion University, Norfolk, Virginia

Biomechanical Lab Software Development — **AUG** 2017–**MAY** 2018
Research Assistant

Certification: Engineer-in-Training

PUBLICATIONS

V. C. Jamora, "Compaction and Residual Stress Modeling in Composite Manufactured with Automated Fiber Placement," M.S., Old Dominion University, United States -- Virginia, 2020.

V.C. Jamora, K. C. Wu, and O. G. Kravchenko, "Residual deformation analysis in composite shell structures manufactured using automated fiber placement," Composite Structures, vol. 248, p. 112482, Sep. 2020

V. C. Jamora, V. Rauch, S. G. Kravchenko, and O. G. Kravchenko, "Effect of Resin Bleed Out on Compaction Behavior of the Fiber Tow Gap Region during Automated Fiber Placement Manufacturing," Polymers, vol. 16, no. 1, Art. no. 1, Jan. 2024, doi: 10.3390/polym16010031